Atomic-level structure and deformation in metallic glasses

Thesis by
David Z. Chen

In Partial Fulfillment of the Requirements for the
degree of
Doctor of Philosophy

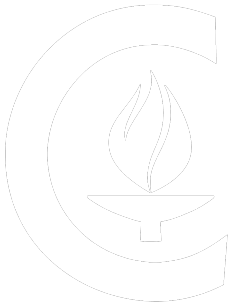

CALIFORNIA INSTITUTE OF TECHNOLOGY
Pasadena, California

2016
Defended May 3, 2016

David Z. Chen
ORCID: 0000-0001-5732-5015

ACKNOWLEDGEMENTS

Time is a fickle thing, but it sure flies when you are having fun. Eight years ago I walked into Prof. Rodney Ruoff's lab at the University of Texas at Austin as a bright-eyed undergraduate researcher. His postdoc, Dr. Weiwei Cai taught me about electrical measurements, ultra-high vacuum systems, evaporative deposition, and I was in awe at how precise and fascinating everything was. It was like walking onto the set of a new Spiderman movie, but better - because it was real. I love science for its people, who always have the time to share their knowledge with you and who are fueled by a passion in their hearts for finding out natural truths. One little-known fact about Caltech is that its motto is "The truth will make you free." This statement resonates with me as a scientist and as a human being, and I resonate with others who also feel drawn towards the truth. There are many, many people who have helped me along the way, and I have done my best to help others as well (the circle of science, so to speak). I would not have gotten this far without my friends, colleagues, and family. Mom and dad, thank you for your unconditional support and love. My close friends (you know who you are), thank you all for the laughs and good times - you are the catalyst for getting me out of rough slumps. My colleagues and lab mates (you know who you are), thank you for being true to yourselves - you are the reason I love science. Finally, my advisor Julia, thank you for all of your support and mentorship. I admire your boundless energy - you are an infinite reservoir of heat for our engines of research.

ABSTRACT

Metallic glasses (MGs) are a relatively new class of materials discovered in 1960 and lauded for its high strengths and superior elastic properties. Three major obstacles prevent their widespread use as engineering materials for nanotechnology and industry: 1) their lack of plasticity mechanisms for deformation beyond the elastic limit, 2) their disordered atomic structure, which prevents effective study of their structure-to-property relationships, and 3) their poor glass forming ability, which limits bulk metallic glasses to sizes on the order of centimeters. We focused on understanding the first two major challenges by observing the mechanical properties of nanoscale metallic glasses in order to gain insight into its atomic-level structure and deformation mechanisms. We found that anomalous stable plastic flow emerges in room-temperature MGs at the nanoscale in wires as little as ~100 nanometers wide regardless of fabrication route (ion-irradiated or not). To circumvent experimental challenges in characterizing the atomic-level structure, extensive molecular dynamics simulations were conducted using approximated (embedded atom method) potentials to probe the underlying processes that give rise to plasticity in nanowires. Simulated results showed that mechanisms of relaxation via the sample free surfaces contribute to tensile ductility in these nanowires. Continuing with characterizing nanoscale properties, we studied the fracture properties of nano-notched MG nanowires and the compressive response of MG nanolattices at cryogenic (~130 K) temperatures. We learned from these experiments that nanowires are sensitive to flaws when the (amorphous) microstructure does not contribute stress concentrations, and that nano-architected structures with MG nanoribbons are brittle at low temperatures except when elastic shell buckling mechanisms dominate at low ribbon thicknesses (20 nm), which instead gives rise to fully recoverable nanostructures regardless of temperature. Finally, motivated by understanding structure-to-property relationships in MGs, we studied the disordered atomic structure using a combination of *in-situ* X-ray tomography and X-ray diffraction in a diamond anvil cell and molecular dynamics simulations. Synchrotron X-ray experiments showed the progression of the atomic-level structure (in momentum space) and macroscale volume under increasing hydrostatic pressures. Corresponding simulations provided information on the real space structure, and we found that the samples displayed fractal scaling ($r^d \propto V$, $d < 3$) at short length scales (< ~8 Å), and exhibited a crossover to a homogeneous scaling ($d = 3$) at long length scales. We examined

this underlying fractal structure of MGs with parallels to percolation clusters and discuss the implications of this structural analogy to MG properties and the glass transition phenomenon.

PUBLISHED CONTENT AND CONTRIBUTIONS

(1) Chen, D. Z.; Jang, D.; Guan, K. M.; An, Q.; W. A. Goddard, I.; Greer, J. R. *Nano Letters* **2013**, *13*, DOI: 10.1021/nl402384r,
D.Z.C. performed in situ tensile experiments, EDX, XRD, and SEM analysis, fabricated samples using FIB, developed the electroplating process, prepared the data, and wrote the manuscript with input from D.J., Q.A., K.M.G., W.A.G., and J.R.G.

(2) Gu, X. W.; Jafary-Zadeh, M.; Chen, D. Z.; Wu, Z.; Zhang, Y.-W.; Srolovitz, D. J.; Greer, J. R. *Nano Letters* **2014**, *14*, DOI: 10.1021/nl5027869,
D.Z.C. fabricated notched samples and assisted in sample characterization and data interpretation.

(3) Chen, D. Z.; Gu, X. W.; An, Q.; Goddard, W. A.; Greer, J. R. *Applied Physics Letters* **2015**, *106* 061903, DOI: 10.1063/1.4907773,
D.Z.C. fabricated samples, assisted in conducting experiments and performing simulations, interpreted the results, and wrote the manuscript with input from all authors.

(4) Gallant, B. M.; Gu, X. W.; Chen, D. Z.; Greer, J. R.; Lewis, N. S. *ACS Nano* **2015**, *9*, DOI: 10.1021/acsnano.5b00468,
D.Z.C. assisted in tensile tests and interpretation of data.

(5) Lee, S.-W.; Jafary-Zadeh, M.; Chen, D. Z.; Zhang, Y.-W.; Greer, J. R. *Nano Letters* **2015**, *15*, DOI: 10.1021/acs.nanolett.5b01034,
D.Z.C. assisted in sample fabrication, characterization, interpretation of results, and manuscript preparation.

(6) Adibi, S.; Branicio, P. S.; Liontas, R.; Chen, D. Z.; Greer, J. R.; Srolovitz, D. J.; Joshi, S. P. *Extreme Mechanics Letters* **2015**, *5*, DOI: 10.1016/j.eml.2015.08.004,
D.Z.C. assisted in interpretation of results and preparation of the manuscript.

(7) Chen, D. Z.; Shi, C. Y.; An, Q.; Zeng, Q.; Mao, W. L.; Goddard, W. A.; Greer, J. R. *Science* **2015**, *349*, DOI: 10.1126/science.aab1233,
D.Z.C. fabricated samples, assisted in X-ray tomography and molecular dynamics simulations. D.Z.C. interpreted the results and wrote the manuscript with input from all authors.

TABLE OF CONTENTS

LIST OF ILLUSTRATIONS

LIST OF TABLES

NOMENCLATURE

$\Delta\epsilon$	strain within the shear band volume *p. 47*
ΔG	activation barrier for free volume jump *p. 23*
Γ	shear band energy *p. 46*
γ	geometrical factor taken to be 0.5 *p. 23*
λ	average free volume jump length for a unit of free volume *p. 23*
ν	Poisson's ratio *p. 48*
Ω	average atomic volume *p. 23*
ϕ	packing fraction *p. 23*
ϕ_c	critical volume fraction (percolation threshold in continuum) *p. 56*
ϕ_j	jamming packing fraction (point j) *p. 59*
ρ	bulk density *p. 23*
σ_y	yield strength *p. 46*
τ	shear stress *p. 23*
ξ	correlation length in percolation models *p. 56*
d	dimensionality *p. 53*
f_D	Debye frequency *p. 23*
L_d	characteristic diffusion length *p. 24*
p_c	percolation threshold *p. 55*
r_{avg}	metallic radius of a single element of interest (one half of the room temperature lattice parameter), or average of elements of interest *p. 62*
r_{is}	outer radius of the ith coordination shell in the real space RDF *p. 62*
v^*	average critical free volume necessary for a jump *p. 23*
v_f	average free volume *p. 23*
A	aspect ratio of the sample *p. 46*
a	major radius of elliptical cross section *p. 48*

c	speed of sound *p. 23*
D	diffusion coefficient *p. 23*
E	Young's modulus *p. 46*
K	bulk modulus *p. 23*
k	Boltzmann constant *p. 23*
L	length of cylindrical tube *p. 48*
M	mass *p. 53*
p	occupancy probability in percolation *p. 55*
q_i	i^{th} peak in momentum transfer (x-ray diffraction) data *p. 53*
r	distance in real space *p. 53*
T	temperature *p. 23*
t	layer thickness of cylinder *p. 48*
T_g	glass transition temperature *p. 58*

Chapter 1

INTRODUCTION

At the University of Texas at Austin, I worked primarily on two topics, graphene (under Rodney Ruoff) and polymer nanocomposites (under Joseph Koo). One thing that struck me was the stark difference between our approach for understanding ordered and homogeneous materials (e.g. graphene) and disordered and heterogeneous materials (e.g. polymer nanocomposites). For graphene, the structure of the material is easy to visualize - carbon atoms arranged in a honeycomb-shaped sheet. Polymer nanocomposites, on the other hand, are a mess - all we know is that the nanomaterials are embedded in a polymer matrix and its concentration, but not even something simple like how well-mixed it is (e.g. average spacing of solute). We characterize ordered systems at the fundamental building-block level, e.g. via crystal structures, and such descriptions are rich and useful for our understanding of the structure. We characterize disordered systems at the system level, e.g. concentrations of solutes and phases, or composition of the overall sample. The fundamental constituents can no longer fully describe the disordered system because the arrangement, or *topology* of those constituents are an integral part of the overall system structure. With isolated graphene sheets, we can apply an approach from fundamental physics. However, if you simply mix those sheets into a polymer matrix, the problem becomes indefinitely more complex. Working with these heterogeneous, disordered materials as an undergraduate researcher, I often felt like an engineer, applying different amounts of additives and characterizing the composite to see how the properties changed. Somewhere on the spectrum between individual graphene sheets and graphene sheets randomly dispersed in an amorphous matrix, we lose our ability to fully describe the structure. As scientists, we seem to have a discomfort with disorder, but this discomfort is not a two-way street, as disordered materials often have very repeatable *properties*. Make two nanocomposites in the same way, and they will have the same properties regardless of the local coordinates and orientations of each graphene flake. There is an underlying regularity to the disordered mess.

Our discomfort with disorder is illustrated by our choice of nomenclature for non-crystalline materials, which we lump together to call *amorphous*, a word with connotations of structureless, formless, and unclassifiable. As material scientists, we

often talk about understanding structure-to-property relationships in materials. How can we understand the structure and properties of such disordered and "formless" materials? It is instructive to study a material that has arguably the most disorder, metallic glasses, which are disordered at the atomic level. In this dissertation we will explore the peculiar properties of metallic glasses at the nanoscale and attempt to understand those properties by inferring changes/differences in the state of the atomic-level structure. These differences are extremely difficult to capture experimentally, as amorphous materials always appear amorphous even though their properties (and structures) depend greatly on their fabrication histories. *Structural* differences are hard to characterize in glasses, but their overall property differences are not. Therefore, the material scientist's approach of structural understanding brings property understanding is reversed for amorphous materials. In many cases, one must start with the properties and infer the structural details. Towards the end of this dissertation we will attempt to characterize the atomic-level structure of these disordered metallic glasses by looking at their local dimensionality. We will utilize the percolation framework as a potential way for understanding how differences in atomic structure arise in metallic glasses and how we may begin to understand and characterize them, thereby correcting the order of structure-to-property relationships.

1.1 Background and Brief Outline

Amorphous metals, or metallic glasses, were first discovered in 1960 by the graduate students of Pol Duwez, who was, incidentally, the advisor of two members on my Thesis Committee (William A. Goddard and William L. Johnson). Duwez and his students alloyed Au with Si and studied its structure after splat quenching, and they were surprised to find that at certain amounts of Si, the structure was not crystalline.[1] Since their discovery, metallic glasses have garnered a lot of attention as potential structural materials. They have high strengths, high elastic limits, corrosion resistance, and great processability. However, their lack of mechanisms for stable plastic flow is a major Achilles heel. At room temperatures, a catastrophic shear band propagates at the elastic limit - the amount of useful plasticity is effectively zero. I will start off by discussing our experiments on nano-sized metallic glasses, which show that metallic glasses have intrinsic mechanisms for plastic flow at the nanoscale. Then I will discuss the atomistic origins of this tensile ductility in nano-wires using molecular dynamics simulations. The challenges that arise in developing intuition on the subtle structural differences that give rise to these

nanoscale phenomena will motivate our discussion on the atomic-level structure in metallic glasses.

Chapter 2

ORIGIN OF SIZE-EFFECT IN DUCTILE NANO-SIZED METALLIC GLASSES

Substantial research has been directed at alleviating the brittleness of metallic glasses (MGs) under tension, where deformation is typically marked by elastic loading followed by catastrophic failure via shear localization within a narrow region called a shear band.[2] Some such toughening efforts make use of various heterostructures and composites, such as the inclusion of dendritic phases, macro-pores, and other obstacles to impede shear band propagation.[3–5] These methods are effective in delaying brittle failure, but intrinsic mechanisms for sustained plasticity in MGs are not activated at room temperatures. An assumption that many literature reports make on bulk monolithic metallic glasses is that the only plasticity carriers are shear bands. Recent *in-situ* nanomechanical experiments on MGs have shown a "brittle-to-ductile" transition, which emerges in ~100 nm-sized MG wires/pillars fabricated using Focused Ion Beam (FIB) milling and subjected to compression[6–8] and tension[9, 10]. These observations suggest a possible mechanism for intrinsic ductility in metallic glasses at room temperatures, one that may not rely on impeding shear band propagation.[1]

The origin of this so-called brittle-to-ductile transition is unclear in part because the experimental results are inconsistent, with some literature reporting this transition to occur at 400 nm[8], 200 nm[6], and 100 nm[7, 9, 10] or not seeing any suppression of catastrophic failure even for samples of 150-300 nm[11–14]. Most of the existing literature on nano-mechanical deformation of individual metallic glass nano structures describes experiments on samples fabricated using a focused ion beam (FIB). This milling technique irradiates the sample surface with a relatively high-energy ion beam, which can potentially lead to a modification of the local atomic arrangements or even to surface crystallization.[15–17] Molecular dynamics (MD) simulations by Xiao, et al. revealed that ion bombardments suppressed shear band formation in 106.4eV-irradiated Zr-based metallic glass nanowires (7.8 nm in diameter and 17.7 nm in length).[18] An alternate synthesis of individual nano-sized metallic glasses suitable for mechanical testing is necessary to ascertain whether the size-induced

[1] Parts of this chapter are published online at DOI: 10.1021/nl402384r

brittle-to-ductile transition is a real physical phenomenon and to shed further light on understanding the deformation mechanisms in metallic glasses at small scales. To date, there has been a paucity of "FIB-less" fabrication methods to produce individual nano-scale metallic glass specimens for nanomechanical testing. Vertically aligned cylindrical nanowires have been synthesized by nanomoulding from bulk samples[14, 19] (Fig. 1a) and thin metallic glass films have been electroplated onto indium-tin-oxide-coated (ITO) glass substrates[20] (Fig. 1b) and deposited using radio frequency magnetron sputtering[21]. None of these methods is well-suited for measuring the mechanical properties of individual nano-sized samples. Selectively removing individual moulded nanowires is one possibility for producing such samples, and tensile experiments on removed $Pt_{57.5}Cu_{14.7}Ni_{5.3}P_{22.5}$ nanowires revealed that for samples ranging from ~100-150nm in diameters and ~1-3μm in gauge lengths, ion irradiation was able to induce a brittle-to-ductile transition, while subsequent annealing reversed it.[14]

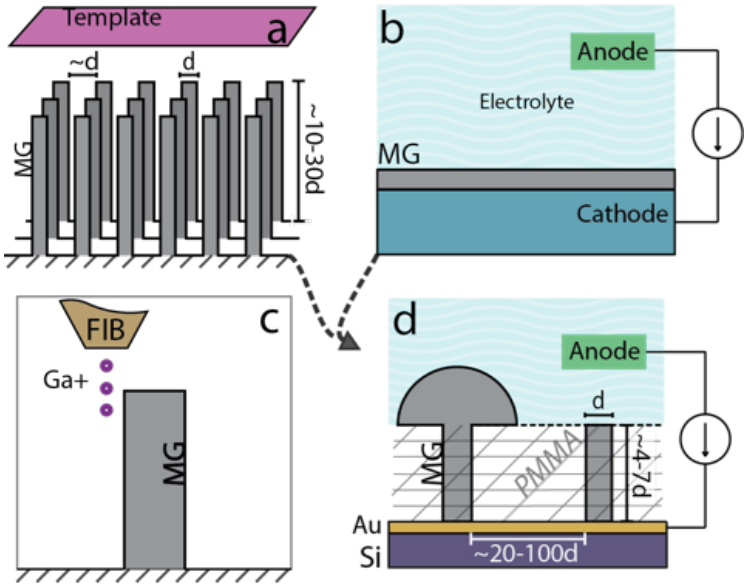

Figure 2.1: Scope of fabrication methods for nano-sized MG specimen. a) Templated metallic glass nanowires fabricated without the use of ion beam irradiation. b) Electroplating method for creating thin metallic glass coatings and films on substrates. An appropriate electrolyte solution is provided with a favorable current density, which drives the ions toward the cathode/substrate. Magnetron sputtering is also possible c) Focused ion beam milling of a bulk metallic glass into nano-scale dimensions for nanomechanical testing. Both compressive and tensile samples can be made in this fashion. d) Templated electroplating procedure used in this work, which utilizes a spin-coated PMMA to act as a mask, isolating the conductive path between anode and cathode at select pillar-shaped holes. Tensile and compressive samples can be fabricated by using this technique.

2.1 Electroplated Ni-P metallic glass nanowires

We fabricated $Ni_{1-x}P_x$ metallic glass nano-tensile samples with ~100nm- and 500nm- diameters and ~650nm- and $2\mu m-$ heights. This synthesis was carried out by electroplating the metallic glass into a Polymethylmethacrylate (PMMA) template, which was spin-coated onto a pre-sputtered Au seed layer on a Si chip and patterned via e-beam lithography (Fig. 2.1d). In addition, a $2\mu m-$thick film was separately electroplated directly onto another substrate by following the same procedure, and nano-tensile samples with identical geometries were FIB-carved into the film. The two sets of samples - electroplated and FIB-carved - were virtually identical to each other, both in composition and geometry (see Table 2.1 & 2.2 for chemical composition analysis and Figure 2.3 for the SEM images of representative samples). Experiments on these samples allowed for a direct comparison between the mechanical responses of otherwise the same metallic glass nano structures with irradiated vs. as-fabricated surface states. A Ni-P system was chosen because it lends itself well to electroplating. NiP metallic glasses may have different short range order (SRO) compared with the more common binary glass, CuZr, which has more metallic-like bonding (see Appendix discussion).[22] Tensile results revealed catastrophic failure in 500nm-diameter samples and post-elastic deformability in 100nm-diameter samples fabricated by both techniques. The extent of tensile ductility was nearly a factor of three greater in FIB samples, which suggests that a less relaxed (irradiated) surface state may facilitate homogeneous plastic flow via activation of numerous diffuse shear bands.

Focused ion beam (FIB) milled		
Comp. (wt%)	Diameter (nm)	Length (nm)
P - 14.0 Ni - 86.0	93.4 ± 7.77	598.2 ± 21.97

Table 2.1: Compositions and geometries of FIBed samples

Template-electroplated (EP)		
Comp. (wt%)	Diameter (nm)	Length (nm)
P - 14.9 Ni - 85.1	104.8 ± 6.46	633.0 ± 76.57

Table 2.2: Compositions and geometries of EPed samples

Figure 2.2 shows an array of electroplated pillars (Fig. 2.2(a)), tensile (Fig. 2.2(b)) and compressive (Fig. 2.2(c)) samples, dark-field transmission electron microscopy (TEM) image (Fig. 2.2(d)), X-ray diffraction (XRD) pattern (Fig. 2.2(e)), and energy-dispersive X-ray spectrum (EDX) (Fig. 2.2(f)). TEM and EDX analyses

were performed on a representative nano-pillar, while the thin metallic glass film was characterized by XRD and EDX. XRD was not performed on the nanopillars because they are smaller than the x-ray beam spot size. The feature-less dark field TEM image and the corresponding diffuse-ring electron diffraction pattern of a 500 nm electroplated nano-tensile sample (Fig. 2.1d) confirm the amorphous microstructure of these electroplated alloys. The EDS analysis (Fig. 2.1f) of relative concentrations of Ni and P revealed that the concentrations of phosphorous, ~14.9 wt% in the nano-pillars and ~14 wt% in the thin film, were virtually identical. The substantial amount of carbon (~4.5 wt%) and oxygen (~4 wt%) on the surface of the electroplated samples was likely a result of the residual organic solvents used to remove the PMMA. The FIB-machined samples also contained a considerable amount of carbon (~3.4 wt%) and oxygen (~1.2 wt%), typical of most metallic surfaces exposed to air. The effect of these surface impurities on the mechanical properties is likely negligible because they do not form continuous layers and hence are not able to bear any load (see Appendix for additional discussion on surface contamination). XRD spectra of the electroplated thin film, shown in Figure 2.2e, reveals the presence of three strong peaks: two for the Si substrate (100) and the seed Au layer ([420]). The broad peak at $2\theta = 20^\circ$ stems from the glass slide onto which the sample was mounted. No known peaks for nickel (2θ = ~45°, Ni [111]) were observed, instead a broad weak peak (indicated by the blue arrow) was present near 2θ of 45°. These observations imply that the electroplated Ni-P metallic alloy was amorphous, consistent with reported literature.[23]

2.2 *In-situ* tensile experiments

Figure 2.3 shows tensile engineering stress vs. engineering strain data for typical 100nm-diameter samples fabricated by both techniques as well as the progressions of the corresponding in-situ SEM images during each experiment, which coincide with the same letter-labeled points in the data. The strain was calculated from the displacement using the frames from the in-situ SEM video rather than the displacement signal from the nanoindenter, a method which has been shown to be more accurate in nano-mechanical experiments[10, 24, 25] (see Appendix for additional information). Evidently, both the FIB and EP samples with 100nm diameters deformed plastically prior to failure. The red dotted lines drawn from the origin serve to emphasize the deviation from linear elastic regime (to guide the eye), which occurred at the strain of 2.6 ± 0.7% for the FIB-machined samples and of 2.9 ± 0.5% for the EP samples. The yield strengths of FIB-machined samples

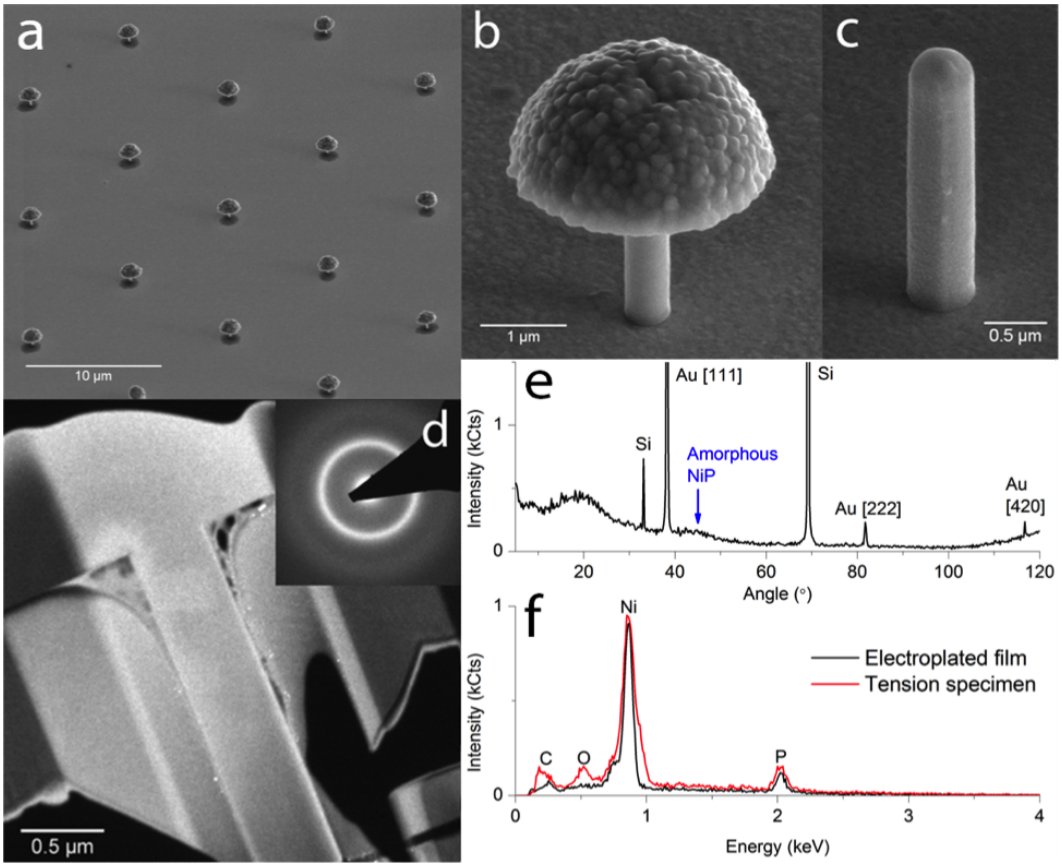

Figure 2.2: Microstructure characterization of fabricated MG samples. SEM images of (a) a ~10 micron-spaced array of tensile pillars created by the templated electroplating process. b) Typical tensile and (c) compressive metallic glass nano structures. (d) A dark field (DF) TEM image of a typical electroplated sample (~500nm-diameter). The white areas outside of the sample correspond to the amorphous Si redeposition during sample preparation process. Inset shows the diffuse diffraction rings typical of an amorphous material. (e) X-ray diffraction (XRD) spectrum of an electroplated NiP film on Si (100). No Ni or P crystalline peaks are present. (f) EDX spectra of the electroplated film and a nano-tensile specimen, which demonstrate a virtually identical chemical makeup.

were slightly lower, 1553 ± 365 MPa versus 1663 ± 291 MPa for EP samples. The total elongation at failure was 5.0 ± 1.2% for FIB-machined samples and 4.0 ± 0.9% for the EP ones. The samples presented are representative of the overall results across ten samples (five of each type), and the average moduli of FIB and EP samples were similar: 63.56 ± 13.38 GPa and 60.26 ± 17.69, respectively. The SEM image in the inset of Figure 3(b') displays necking in a 100nm-diameter Ni-P metallic glass nano-cylinder fabricated by focused ion beam, a behavior highly atypical for metallic glasses, which is consistent with a previous report on similarly

conducted experiments on Zr-based metallic glass nano-structures.[10] Necking was less observable in the electroplated samples (Fig. 2.3(b)) likely because of the limited ductility and poorer image contrast. Although both the EP and FIB samples with 100nm diameters exhibited some deformability, the final failure always commenced via shear banding in all samples. These observations are equivalent to those of the tensile experiments on the FIB-fabricated Zr-based metallic glass nano samples, which showed deformation and necking leading to final failure by shear banding.[10] The stress-strain data (Fig. 2.3) indicates that the FIB and the EP samples had the same average tensile strength of ~1.9 GPa (±0.36 for FIB, ±0.37 for EP), but the FIB specimens were, on average, capable of sustaining nearly three times greater plastic strain prior to failure of ~2% compared to ~0.76% for the electroplated samples. Here, plastic strain is defined as the total strain at fracture less the elastic strain, $\epsilon_p = \epsilon_f - \epsilon_y$. This dissimilarity in the amount of plastic flow between the two sets of samples may be an indication that the FIB-induced irradiation on the sample surface contributes to the tensile ductility of the sample but is not solely responsible for its presence.

These results are diametrically opposite to the tensile response of the 500nm-diameter electroplated samples, shown in Figure 2.3, as well as of bulk metallic glasses and FIB-machined metallic glass samples of equivalent diameters from literature[7, 8, 10, 26], which is generally marked by an elastic loading followed by a sudden and catastrophic failure via shear banding with no nominal plastic deformation or necking prior to failure.[2] The 500nm-diameter electroplated samples were fabricated via the same electroplating process and had a phosphorous content of ~16.5 wt%. This slight increase in phosphorous content may affect the modulus and strength of the samples,[27] but it is unlikely to be solely responsible for the brittle behavior in these samples. EDX and TEM analysis of the 500nm-diameter samples confirmed that they were also amorphous.

The results of these experiments can be summarized with two main observations. First, tensile ductility in the 100nm-diameter and a lack thereof in the 500nm-diameter electroplated Ni-P metallic glass samples suggests that the brittle-to-ductile transition is a result of the size effect in metallic glasses rather than of any irradiation effects. Second, surface irradiation with low-energy Ga ions appears to tune the amount of deformability in the metallic glasses whose external dimensions are below a certain critical length scale, i.e. a more pronounced necking and increased plastic strain prior to failure in the FIB-fabricated samples with identical chemical

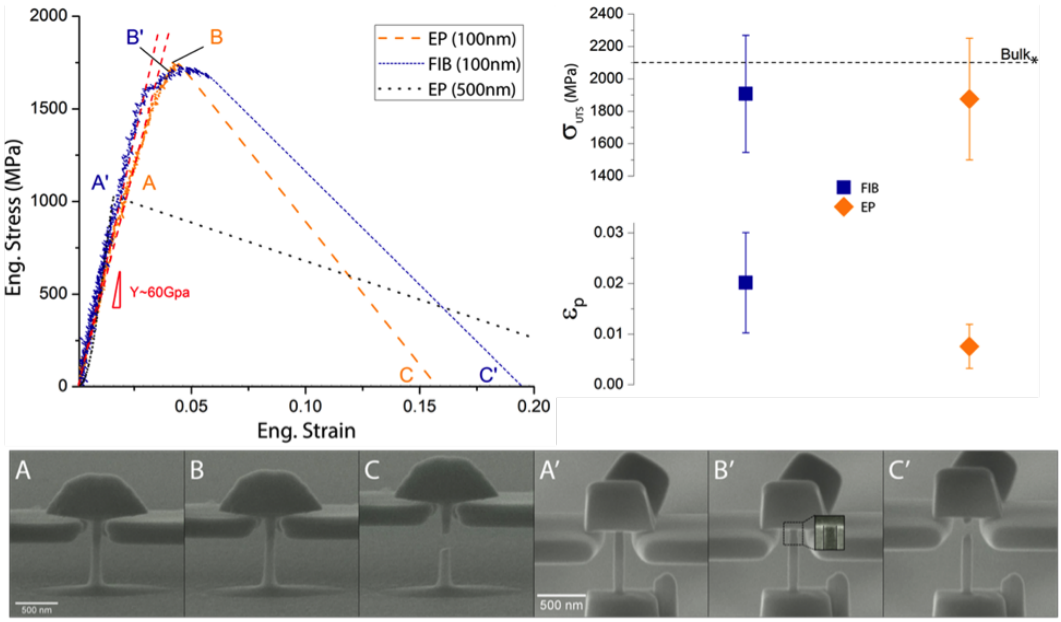

Figure 2.3: Mechanical behavior of EP and FIB samples under tension. Upper left: Engineering stress-strain for EP 500 nm, EP 100 nm, and FIB samples along with video stills from in situ SEM (A-C, A'-C'). A linear red dotted line is added to emphasize the deviation from elastic loading. The 500 nm EP samples break catastrophically while both 100 nm specimen show tensile ductility. A, A') Initial contact between grip and sample, with purely elastic loading. B, B') FIB samples show noticeable necking prior to failure, visible in the inset of B'. Necking is less pronounced in EP samples. C, C') Fracture of specimen with both types marked by shear banding. Upper right: Ultimate tensile strength and plastic strain for both sample types. EP and FIB samples show identical tensile strength (~1.9 GPa). FIB specimen are able to sustain nearly three times higher mean plastility prior to failure ($\epsilon_p = \epsilon_f - \epsilon_y = 3\%$ versus 1.5%), within one standard deviation of EP counterparts. *Bulk refers to tensile strength calculated from microhardness values using a Tabor factor of 3.[23]

composition as the electroplated ones. These results suggest that the microstructural disorder in the vicinity of the free surface may contribute substantially to the mechanism of shear band formation and propagation.

2.3 Discussion of experimental findings

Post-elastic deformation in metallic glasses is generally carried by the spontaneous motion and coalescence of shear transformation zones (STZs) via collective rearrangements of atomic clusters (on the order of ~100 atoms) ubiquitously populating the microstructure of the amorphous metals.[28, 29] At yield stress, some of the STZs coalesce and assemble into large planar bands, generally called shear bands.[2]

Shear band formation and propagation is a highly localized deformation mechanism in metallic glasses strained at room temperature. Homogeneous deformation in bulk metallic glasses has typically been observed only at temperatures above or near the glass-transition point.[30] In contrast to the room temperature experiments in this work, the high-temperature tensile response in metallic glasses has a peak stress close to the elastic limit of the material and subsequent work softening, with failure occurring only when the sample gauge section draws down to a point.[31] Both sets of the EP and FIB-fabricated samples with 100 nm diameters in this work showed considerable differences in their behavior under tension as compared with their bulk counterparts: ultimate tensile strength extended beyond the elastic regime, which is an earmark of work hardening, and failure occurred via shear banding rather than by drawing-to-a-point. These outcomes imply that the size- and/or surface-effect in nano-sized metallic glasses may delay the onset of shear banding.

These findings differ from those reported by Magagnosc, et al. on uniaxial tension of moulded Pt-based metallic glass nanowires with diameters of ~100-150 nm, which compared FIB irradiated samples to the as-moulded ones.[14] The FIB-exposed samples in that work also showed extended plasticity of ~2%, qualitatively similar to the results of this work, but they failed by necking down to a tip rather than by shear banding. The as-moulded samples in Magagnosc, et al.[14] did not display enhanced plasticity even at ~100 nm. A possible reason for this difference is that the ~1-3 μm-long gauge sections of the Pt-based metallic glass samples in Magagnosc, et al. were 2-5 times longer than those in the Ni-based samples in this work. Large-scale MD simulations on Cu nanowires under uniaxial tension demonstrated that the sample length plays a significant role in determining brittle or ductile behavior.[32] In that work, the simulated 20-nm diameter single crystalline Cu nanowires with lengths of 188, 376, and 751 nm exhibited ductility and necking while the 1503nm-long nanowire failed by unstable shear localization and abrupt failure when pulled in tension to ~7% strain. The authors explained this phenomenon by the higher stored elastic energy in longer wires, which in their work meant that the longer sample had highly concentrated dislocation activity on mainly the same slip systems and in a localized shear region.[32] Although no dislocations are present in metallic glasses due to a lack of crystallographic order, the analogous line of reasoning that a higher stored elastic energy in longer samples may lead to shear banding is applicable because the deformation process occurs via shear in both cases.

2.4 Molecular dynamics of $Ni_{80}Al_{20}$

To elucidate the specific role of the irradiation on the mechanical response of metallic glass nanopillars, molecular dynamics simulations were conducted on $Ni_{80}Al_{20}$ binary alloy. This particular system was examined rather than a replica NiP system because of the limited availability of appropriate Ni-P interatomic potentials. The mechanical properties of $Ni_{80}Al_{20}$ should be comparable with those of the Ni-P metallic glasses used in the experiments, which have compositions close to $Ni_{80}P_{20}$. Both types of samples are Ni-rich metallic glasses, and the inclusion of P or Al should play similar roles in increasing the glass forming ability in both cases. All the simulations were carried out using LAMMPS,[33] and the energies and forces were determined using an embedded-atom method (EAM) potential for Ni-Al binary alloys.[34] Further details on these simulations can be found in the appendix.

In the simulations, two sizes of nanopillars (400,436 atoms: 10nm diameters and 66.9nm lengths, and 7,210,516 atoms: 30 nm diameters and 134.2 nm lengths) were cut from replicated $Ni_{80}Al_{20}$ liquid configurations. The liquid pillars were then quenched to room temperature at a cooling rate of $1 Kps^{-1}$, resulting in a material system similar to the EP pillars used in the experiments. A reflective potential wall is applied outside the pillar during quenching to confine its shape, similar to the simulated casting method developed by Shi.[35] To emulate the FIB pillars, we implanted Al atoms randomly outside the cylinder with a fluence of $0.0625/nm^2$, a value calculated using the experimental irradiation conditions. An inward velocity corresponding to 1 keV was then applied to all of the inserted Al atoms. Since the fluence was very small compared to the number of atoms in the system, the resulting increase in relative Al content in the irradiated samples was negligible. Uniaxial tension was then applied to both pillar types at a constant strain rate of $0.0001\ ps^{-1}$. Figure 2.4 shows the stress-strain response of these pillars: FIB samples transition from elastic to plastic flow at slightly earlier strains, and the yield strengths of FIB samples are also slightly lower, but the overall difference becomes more subtle as the pillar diameter increases. The strengths of all simulated samples were significantly higher than those obtained in the experimental values. This can be attributed to the high strain rates, a limitation imposed by the large size of our simulations and increasing computational time.

The observed size-induced emergence of ductility in nano-sized metallic glasses can be rationalized in terms of energetics. Since samples produced by both fabrication techniques ultimately failed by shear banding, the total elastic strain energy stored

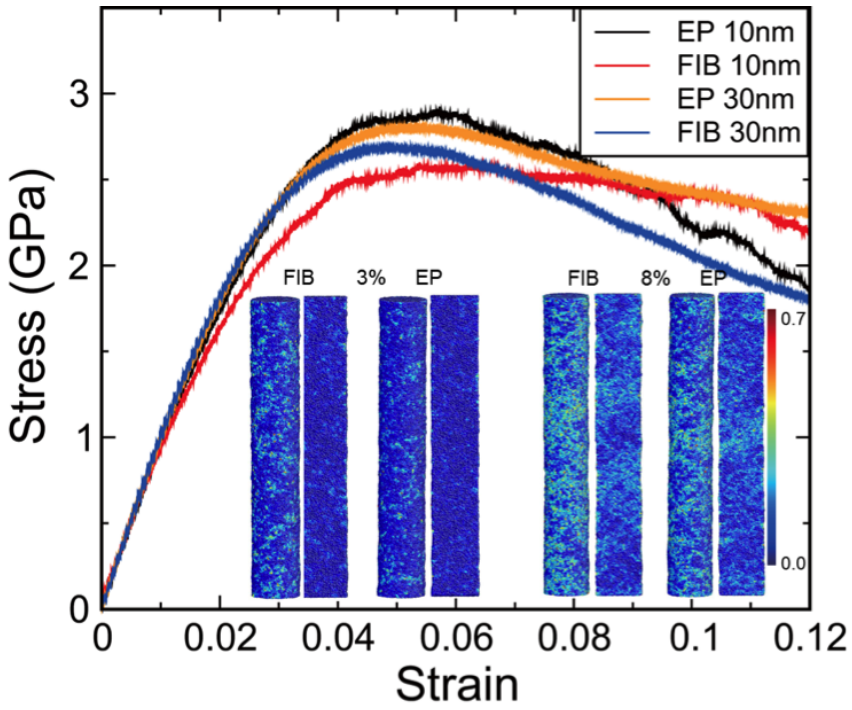

Figure 2.4: Stress-strain curves of EP and FIB samples for the binary $Cu_{46}Zr_{54}$ binary alloy system simulated via Molecular Dynamics using LAMMPS. Results for 10 nm and 30 nm pillars deformed at strain rates of 0.0001 ps^{-1} are presented. Atomic local strain analysis is provided at 3% and 8% strains for both EP and FIB samples, with color-coded mapping of strain intensity ranging from 0.0 (blue) to 0.7 (red). A pair of strain mappings is shown for each combination of sample type and strain with the left ones corresponding to pillar surfaces, and right ones corresponding to pillar cross-sections.

in a sample with a characteristic dimension d scales as d^3. The surface energy that a fractured surface or a shear band would have to surmount to propagate scales as d^2, where d is the diameter. Thus, at sufficiently low sample sizes, the surface energy term dominates over the elastic strain energy, and it becomes progressively unfavorable for catastrophic failure to occur at smaller deforming volumes (see Fig. A.2 in Appendix). Within this shear band-dominated framework, there is a critical diameter at which the two energies coincide, and the experiments described here suggest that this length scale is between 100 nm and 500 nm for this particular metallic glass. Consistent with the experimental results presented here, the theoretical work of Thamburaja on the strained small-scale metallic glasses with fixed diameter-to-length aspect ratios of 1:2 and diameters ranging from 8.5nm to 136nm also revealed shear band suppression.[36] In that work, the non-local, continuum-based theory and classical thermodynamic arguments were incorporated within the finite element

framework, which revealed that sample size reduction delayed and diminished the severity of shear localizations such that the samples smaller than the shear band nucleus size, on the order of 28 nm, deformed homogeneously only.36 Although compression results cannot be directly compared to ones obtained in tension due to the apparent tension-compression asymmetry in metallic glasses in plasticity,[37] there have also been numerous observations of size-induced shear band suppression in taper-free pillars under in-situ compressive loading.[38, 39]

The differing amount of post-elastic deformation observed in the samples fabricated by FIB vs. by EP may be explained by the surface modification induced by Ga ion bombardment. During FIB milling, the ion beam knocks the metallic glass atoms out of their native positions and generates free volume which may disrupt local icosahedral symmetries (see Fig. A.2 in Appendix). Such displaced atoms have higher potential energies, which increases their probability of participating in plastic deformation via a shear transformation because the energy cost of moving such atoms is lowered, akin to the free volume driven mechanism for homogeneous flow (see Fig. 4).[31] This is corroborated by the observation that our FIB samples began plastic deformation at a slightly earlier strain (~2.6% versus ~2.9% in EP), and thus at a lower strain energy. As expected, we also see a marginal decrease in yield strength for FIB samples (~1550 MPa versus ~1660 MPa for EP), which lie within their mutual error bars. Plastic deformation at lower strain energies in this case may be a sign of the movement of FIB-displaced, high potential energy atoms. The presented arguments are also supported by Raghavan, et al.'s work on Ni ion-irradiated Zr-based metallic glasses, which shows free volume generation leading to enhanced plasticity in fabricated micropillars[40] and irradiation-induced transition to homogeneous flow under nano-indentation[41]. In addition to the size effect, this surface effect may further deter crack initiation at the free surface and stifle catastrophic failure. This would allow the formation of instabilities, such as necking or drawing to a point to take place prior to fracture, which is supported by the results in the uniaxial tensile experiments presented here and in Magagnosc, et al.,[14] as well as by the nano-indentation experiments on a magnetron-sputtered Zr-based metallic glass by Liu, et al.[42] and a bulk Zr-based glass by Raghavan, et al.[41], mentioned above. It is reasonable that the surface state with more free volume and higher potential energy per atom may suppress catastrophic shear banding and explain the experimental observations presented here.

To reveal physical mechanisms of deformation as a function of surface energetics,

we calculated the atomic local strain at 3% and 8% strains for the 10 nm pillars to visualize and quantify regions with pronounced plasticity and atomic activity. These are depicted in the inset of Figure 2.4 and show that the surface atoms (left mapping in each pair) carry most of the plasticity at 3% strain, while the pillar cores (right mapping) show little activity. FIB samples also display more strain activity on the surface compared to EP samples. Shear localizations emerge at 8% strain in the pillar cores and span the entire sample diameters. In this case, the FIB samples have slightly more diffuse shear regions, whereas these regions appear more concentrated in the EP samples. The main observations from the simulations are: (1) the surface atoms carry most of the early plasticity and (2) the FIB pillars contain more diffuse shear localizations. These findings corroborate our experimental observations and proposed phenomenological theory.

2.5 Conclusions

We developed an electroplating-based nano-fabrication methodology to create isolated metallic glass nano structures, which does not utilize ion irradiation. In-situ uniaxial tensile experiments on such-fabricated Ni-P metallic glass nano structures and on the nominally identical ion-irradiated (FIB) ones revealed that samples with 100nm-diameters produced by both fabrication techniques displayed post-elastic deformability and necking at room temperature. This is in contrast to the immediate failure via a single sample-spanning shear band of 500nm-diameter nano structures tested and fabricated by the identical electroplating methodology, as well as of FIB-produced and bulk metallic glasses[2, 26]. These findings demonstrate that the brittle-to-ductile transition in Ni-based metallic glasses is likely size-induced and is not a sole effect of ion irradiation. The irradiated samples exhibited a factor of three greater plastic strain-to-failure than the electroplated ones. The lower elastic strain in FIB samples suggests that ion irradiation perturbs the surface energy state to produce atoms with higher potential energies and lower icosahedral symmetries, which are more likely to participate in shear transformations. This provides a plausible explanation for the surface-state effect in irradiated metallic glasses, and it is well-supported by our simulations results, which show that surface atoms carry the early plastic strain, an effect that is more pronounced in the simulated FIB samples, and that shear transformations are more diffuse in simulated FIB samples. Experimental observations such as those in this work further our understanding of the underlying deformation mechanisms in amorphous metals, which have generally been difficult to study and are not well understood.

Chapter 3

WORK HARDENING IN A METALLIC GLASS

Work hardening is a peculiar phenomenon in nano-sized metallic glass samples. In particular, Jang *et al.* demonstrated a transition in failure mode from shear banding at the elastic limit to ductile necking-to-shear-banding in Zr-based MG wires when the diameters were reduced to ~100 nm. Stress-strain data for these samples shows distinct work hardening and permanent plastic deformation upon loading and unloading past the elastic limit.[43] Similar plasticity and necking have been reported for electrodeposited 100nm-diameter NiP MGs, with and without the use of Ga+ ion beam (Chapter 1).[44] Necking and strain hardening are typical for crystalline metals and metal alloys, whose plastic flow is enabled by the motion and interactions of dislocations, but highly atypical for amorphous metals. These findings leave us with two significant open questions: (1) Is there an analogous process that occurs in amorphous metals and (2) what is the role of this process with respect to the sample size? In our earlier work, we had speculated that this size effect points to a surface modulated mechanism for the hardening, an idea supported by the additional enhancement in ductility in ion beam-irradiated samples.[44] To explore the physical origins of emergent hardening in nano-sized metallic glasses we performed in-situ nano-tensile experiments on smaller, ~70nm-diameter, electrodeposited NiP MG samples, with a surface area-to-volume ratio of ~0.06, compared to ~0.04 for ~100nm samples, enhancing the relative role of the sample surface by 50%.[1]

3.1 Electroplating smaller samples

To fabricate the 70nm-diameter NiP samples, we employed the same fabrication parameters described previously with a reduced pore size in the templates. This enabled the fabrication of chemically identical but smaller electroplated NiP MG samples as compared to those in our previous work (see Tables 2.1 & 2.2 for chemical composition and geometries). These smaller samples allow us to compare the relative contributions to ductility from (1) the high potential energy atoms within the surface caused by ion irradiation and of (2) increased surface area to volume ratio of an as-plated randomly packed nano-metallic glass.

[1]Parts of this chapter are published online at DOI: 10.1063/1.4907773

Figure 3.1 shows an array of electroplated pillars (Fig. 3.1a), as well as a schematic of the fabrication process (Fig. 3.1b). Details of the electroplating technique were described in the previous chapter. Robust repeatability of the electroplating process suggests that the smaller-diameter pillars studied in this work have nominally the same chemical composition and amorphous microstructure as the 100nm-diameter samples from Chapter 1.

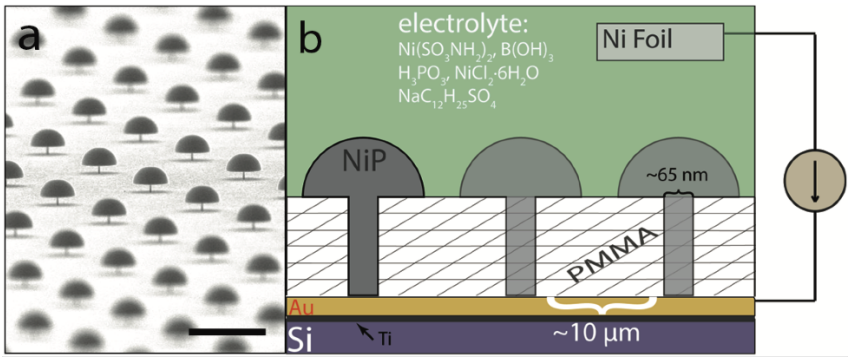

Figure 3.1: Electroplating smaller Ni-P samples. a) Characteristic electroplated metallic glass samples. Scale bar is 6.5 µm. b) Schematic of the template electroplating procedure.

3.2 Sample characterization and testing

Figure 3.2 shows scanning electron microscope (SEM) images of a typical as-plated sample (Fig. 3.2a) as well as a time-lapsed progression from the in-situ tension movie (Fig. 3.2b-f). The corresponding engineering and true stress versus strain data is provided for the representative sample (Fig. 3.2g and h). The true stresses and strains were obtained by measuring the sample diameter in the neck region using image analysis and in-situ SEM video snapshots. Average values for engineering ultimate tensile strength and plastic strain for the seven tested samples are provided in Figure 3.3, along with those for the previously tested 100nm-diameter electroplated (EP) NiP samples and 100nm-diameter FIB-milled NiP samples from Chapter 1 for comparison. Pillar diameter is the only attribute in these samples that is varied, with the exception of the FIB-milled sample, which was FIB-carved from an electroplated thin-film. Uniaxial tensile experiments were performed in a custom-made in situ SEM with a nanomechanical module, InSEM (Nanomechanics, Inc.), at a constant nominal displacement rate (0.4-6 nm/s), resulting in a global strain rate of ~0.001 s^{-1}. The ultimate tensile strengths were comparable across all samples: 1.92 ± 0.14 GPa for 70 nm EP, studied in this work, 1.87 ± 0.38 GPa for 100 nm EP, and 1.91 ± 0.36 GPa for 100 nm FIB-carved sample (Chapter 1). Plastic strain,

defined as the difference between the total strain and the elastic strain, $\epsilon_p = \epsilon_{total} - \epsilon_{elastic}$, were nearly the same for 70 nm EP and 100 nm FIB samples at 2.0 ± 0.5% and 2.0 ± 1.0% strain, respectively. These values were ~2.5 times higher than the plastic strain for 100 nm EP samples, ~0.8 ± 0.4%. Elastic moduli were consistent across all samples: 71.4 ± 32.9 GPa for 70 nm EP, 63.6 ± 13.4 GPa for 100 nm FIB, and 60.3 ± 17.7 GPa for 100 nm EP. Contrary to the catastrophic failure via shear banding at the elastic limit often seen in large MG samples, the 70nm-diameter samples studied in this work show significant nonlinear plasticity along with necking and work hardening, characteristics typically associated with the tension of ductile metals and alloys. A high degree of plasticity is also manifested in the true strains at failure: ~18% for the 70 nm samples and ~14% for 100 nm FIB samples. Although necking in nano-sized metallic glasses has been observed experimentally, outside this work and that in Chapter 1, it has either been in non-freestanding samples[45] or in samples that have been FIB-carved[43, 44, 46, 47]. An important aspect of this result is that failure still initiates via the dominant fracture mode of metallic glasses, which is shear banding. We did not observe any change in failure morphology, which suggests that the material likely remained glassy.

3.3 Free surface relaxation pathways

One mode of deformation in MGs is the spontaneous collective rearrangement of ~10-20 atom-sized clusters,[**apl2015-16**, 48–52] commonly referred to as shear transformation zones (STZ).[53, 54] Room-temperature plasticity in metallic glasses is typically nonexistent because at these conditions the STZs strain-soften and coalesce quickly to form shear bands that lead to sample failure. Homogeneous deformation in monolithic BMGs can typically only occur at elevated temperatures, above or near the glass-transition, with failure marked by necking and drawing to a point in place of shear banding and strain softening.[55–58] In contrast to the mechanical response of both room-temperature and elevated-temperature bulk metallic glasses, the 70 nm EP samples studied in this work, as well as 100 nm FIB and EP samples, show significant post-elastic deformability while maintaining shear band propagation-mediated failure. Based on these observations, smaller samples (70-100 nm EP) and samples with a modified surface (100 nm FIB) show mechanical response that is intermediate to both the room-temperature and near T_g-temperature response in monolithic bulk MGs. What sets it apart is the emergence of work hardening, which suggests that an internal hardening mechanism exists as well.

This leaves us with the unusual result that nano-sized metallic glasses not only

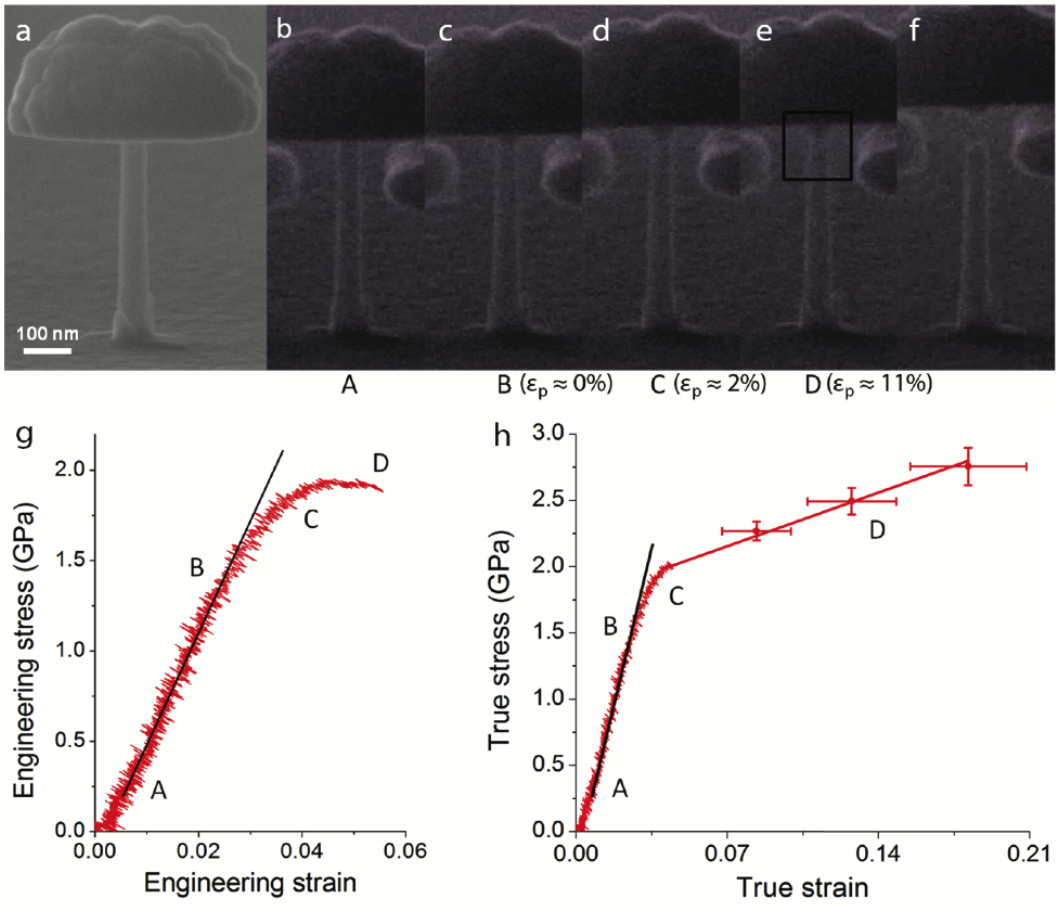

Figure 3.2: Electron micrographs and stress strain data showing work hardening behavior. a-f) Corresponding in-situ SEM micrograph snapshots of the deformation (contrast adjusted). Necking can be observed in the boxed region of panel e. g,h) Engineering and true stress strain curves with corresponding SEM images at A: initial loading, B: elastic limit, C: plasticity, and D: necking prior to failure. Error bars represent measurement error of diameter in necked region.

deform plastically, but work harden as well. Although energy-scaling arguments, such as the one presented in refs. [43, 47, 59] describe the emergence of size-induced shear band suppression using the competition between crack-like shear banding and homogeneous plastic flow, no intuition about the underlying physical process is gained from such an argument. To gain insight into the physical and microstructural origin for the enhanced ductility, we analyzed the results of MD simulations on 30nm-diameter $Ni_{80}Al_{20}$ pillars. These simulations were conducted using an embedded atom method (EAM) potential in LAMMPS, with further details on the parameters provided in Chapter 1. A Ni-Al EAM potential was chosen over a Ni-P potential because the Ni-Al system has been well tested for mechanical

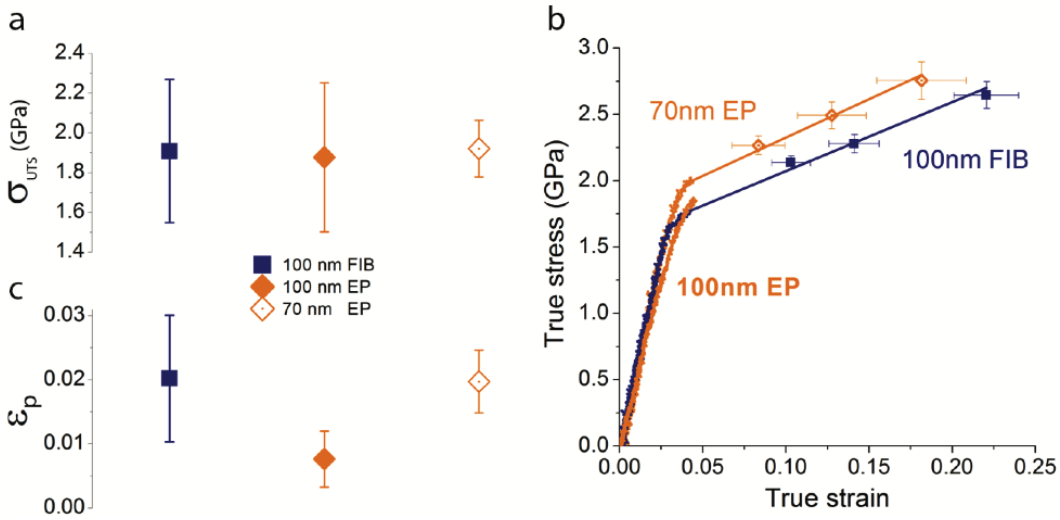

Figure 3.3: Comparison of mechanical response in differently-sized samples. a) Ultimate tensile strengths for all samples. b) True stress strain comparison. c) Engineering plastic strains.

properties while the existing Ni-P potentials are more optimized for atomic scale deformation. Despite the differences in chemistry and stoichiometry between the Ni-Al and the Ni-P glasses, their mechanical properties are likely indistinguishable because both systems are amorphous and have comparable short range order caused by the similarities in their atomic bonding. In this analysis we tracked the evolution of free volume distribution across two different sample types, as-cast (Fig. 3.3(a,c), left side) and irradiated (Fig. 3.4(b,d), right side), as a function of tensile strain by binning the pillars with concentric hollow cylinders with 1Åthickness (Fig. 3.4e) using a simple Voronoi tessellation. Here the free volume distribution is estimated by an excess Voronoi volume, which is the mean binned Voronoi volume taken at each strain value (0, 1, 3, 5, and 7%) minus the mean Voronoi volume over the whole system at the initial configuration (0% strain). The computations reveal that during initial elastic loading (0 to ~5% strain) the free volume in both samples increased uniformly and isotropically, albeit the irradiated system initially had ~2-3% higher free volume near the free-surface (0.6-0.9 d/d_{max}) compared to the as-cast system due to the collision cascades caused by the irradiation process. These findings are not surprising because both are characteristic of bond length dilation associated with elastic deformation. Once ~5% plastic strain is attained, the free volume starts to evolve differently for the core atoms ($d/d_{max} < 0.95$) than in the near-surface region ($d/d_{max} > 0.95$), attaining saturation in the core despite the local atomic displacements showing significant activity. Conservation of total volume

during plastic deformation is expected in metals where crystallographic slip via shear processes give rise to plasticity, but it does not necessarily hold for metallic glasses, whose common mechanisms of atomic-scale deformation are STZ-type and diffusive-jump-type, both of which are dilatational rather than based on shear.[55] A semi-permanent local increase in free volume is thought to occur in the course of either mechanism in addition to a transient dilatation, which is necessary to overcome the local saddle point configurations in energy.[55] Indeed, in contrast to pillar samples, similar MD simulations on a bulk NiAl metallic glass system with periodic boundaries in all directions shows that the Voronoi volume continues to increase during plasticity, after loading past 5% strain (See Supporting Information for details). Following these observations, in order to maintain a constant free volume distribution at the pillar cores, free volume in the near-surface regions have to absorb the local dilatational processes, setting up a mechanism whereby the free surface and the near-surface region may serve as free volume 'sinks'. We postulate that in the course of plasticity, two possible mechanisms are at play: (1) near-core region dominates the deformation and prevents the core atoms from undergoing local dilatations, or (2) the core-atoms first undergo local dilatations, which subsequently rearrange and migrate toward the free surface through a diffusion-like process, and annihilate. The first mechanism is unlikely, as we know from previous mappings of the local atomic displacements that the core atoms are involved in significant local displacements during plastic deformation.11 The second proposed mechanism is consistent with the observed ~10% increase in the excess free volume between 3 and 5% strain followed by a ~10% decrease between 5 to 7% strain in the near-surface region of the as-cast system (Fig. 3.4a) (See Supporting Information for details of the MD analysis). In this case, the ability of the atomic clusters that are in the vicinity of the free surface to absorb excess free volume may derive from their relatively unconstrained access to the lower local free volume configurations. Depletion in the overall free volume at the core of the pillar as a result of this migration appears to inhibit shear localization and shifts the overall deformation to a quasi-homogeneous mode. This postulated surface-mediated relaxation can also explain the necking behavior that emerges when nano-sized metallic glasses are pulled in tension: it allows the sample to attain a steady-state of free volume creation and annihilation within the neck. Therefore, within this phenomenological description, the observed size effects are due to increases in the surface area to volume ratio, which allows the entire sample to undergo more homogenous-like deformation before significant shear localization can occur.

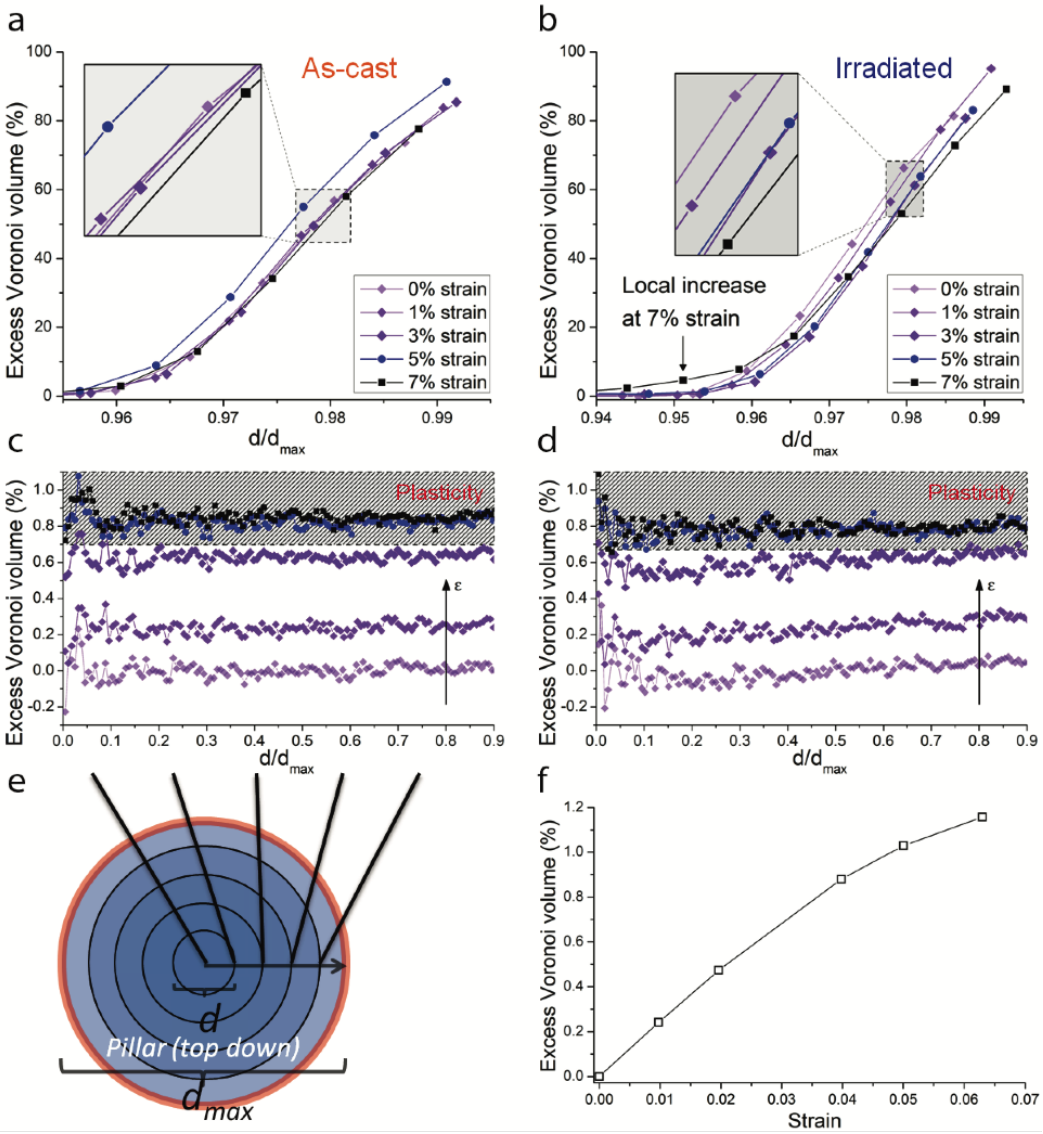

Figure 3.4: Tracking volume evolution during deformation in MD. a) Excess Voronoi volume in the near surface region (outer 5-6% of pillar) for the as-cast system and b) the irradiated system. c) Excess Voronoi volume in the core region for the as-cast system and d) the irradiated system. The grated region indicates when plasticity occurs. Each point in plots a-d represents values averaged over a 1Å-thick hollow cylindrical bin. e) A coarse-grained top-down schematic of the binning procedure. The core region (blue) is plotted in c and d, while the near-surface region (red outer ring) is plotted in a and b. f) Excess Voronoi volume versus strain for a bulk NiAl system.

Enhanced ductility has also been reported for nano-sized samples whose surfaces have been bombarded with ions, for example during FIB-milling.[43, 44, 46, 47] The plasticity mechanism postulated here applies to that phenomenon as well. Irradiating

the sample with energetic ions causes two effects: (1) it broadens the near-surface region and (2) it increases the energy of the free surface by generating excess free volume near the surface, inducing a roughly homogeneous distribution of saddle-point configurations in the region. This results in a local decrease in free volume during elastic loading (Fig. 5-right), and in the relaxation of the saddle-point configurations near the surface. Between 3 and 5% plastic strain, the free volume in the near-surface region no longer decreases, which suggests a competition between the free volume generation due to dilatation and the loss of free volume at a sink like the free surface. More revealing is the process between 5 and 7% plastic strain, where a local increase in free volume of ~5% occurs further from the free surface than what is observed for the as-cast sample (d/d_{max} ~0.95) and further relaxation occurs closer to the free surface (d/d_{max} > 0.98). These observations suggest that FIB-milling may effectively broaden the near-surface region, reducing the diameter of the core region and further promoting homogeneous deformation. It may be the unique interplay between the atomic arrangements within the core and the surface in the nanometer-sized metallic glasses that gives rise to the observed ductility.

3.4 Estimation of characteristic timescale for relaxation

In order to validate that such a relaxation through the free surface can be responsible for the observed phenomena, the relevant timescale for the proposed diffusion-like relaxation process can be compared to that for shear banding. Following the work of Spaepen on free volume evolution during homogeneous and inhomogeneous flow in metallic glasses,[57] we can estimate a diffusion coefficient for the evolution of free volume using the following:

$$D = \frac{1}{6}\,\nu\lambda^2 \exp\left(\frac{-\gamma v^*}{v_f}\right)\exp\left(\frac{-\Delta G}{kT}\right) \tag{3.1}$$

where f_D is the Debye frequency, λ is the average free volume jump length for a unit of free volume, γ is a geometrical factor taken to be 0.5, v^* is the average critical free volume necessary for a jump, v_f is the average free volume, $\Delta G = \tau\Omega$ is the activation barrier which depends on shear stress τ and on the average atomic volume Ω, k is the Boltzmann constant, and T is temperature. The Debye frequency is given by $f_D = (3N/4\pi V)1/3c$, where $c = \sqrt{K/\rho}$ is the speed of sound, K is the bulk modulus, estimated to be ~130 GPa from a Ni-based BMG,19 and $\rho \approx 7.8 g/cm^3$ is the density.20 Using a packing fraction of $\phi \approx 0.68$,21 we can estimate N/V

to be ~8.3 $\times 10^{28}$ atoms/m^3, using the known average atomic volume of $Ni_{75}P_{25}$. This gives a diffusion coefficient of $D \approx 5 \times 10^{10} nm^2/s$ (Refer to the Supporting Information for details on other parameters). We can then estimate the characteristic diffusion length, $L_d = \sqrt{4Dt}$, as ~446 nm over 1 μs. In comparison, experiments with a high-speed camera estimate shear band velocities for a Zr-based MG to be from 2.8 to 5.6 nm/μs under compression, which is notably less than the estimated characteristic diffusion velocity for free volume.22 This suggests that the proposed dilatation-relaxation process can happen faster than the shear localization and may explain the ductility in these samples.

3.5 Discussion of work hardening and implications

The physical origin of work hardening in the nano-sized MG samples may stem from the same mechanism as the one we proposed for ductility: surface-mediated relaxation within the atomic arrangements in the outer surface region leading to a deficiency of free volume in the core of the nano-sized cylinder, suppressing the coalescence of free volume into a catastrophic shear band. In this mechanism, hardening may occur after the rate of free volume annihilation through the surface becomes comparable with the rate of free volume generation within the sample, which results in quasi-homogeneous flow and a state of free volume "starvation," somewhat analogous to dislocation starvation in single crystalline nanopillars.[60]

Amorphous metals represent a particularly challenging type of material to study due to their lack of crystallographic order, rendering typically powerful characterization techniques for crystals such as transmission electron microscopy (TEM) and electron backscatter diffraction (EBSD) far less useful. There also appears to be a disconnect between experimental observations for bulk metallic glasses (BMGs) and nanomechanical observations for nano-sized metallic glasses (nano MGs). When tested in the macroscale, the only plasticity mechanism present in room temperature monolithic samples seems to be the shear band, which is problematic, as once shear localization occurs, the sample typically fails catastrophically, especially in tension.[55] In the nanoscale, however, there is the observation of a size effect in tensile failure mode, which transitions from that of brittle-like shear band propagation in larger samples (i.e. greater than ~100 nm) to a more ductile mode in which shear banding is suppressed and necking/work hardening is observed.[43–45] The difference in observed phenomena here is likely due to the rate dependence of the amorphous system on the structural dynamics of being driven from their metastable state: in bulk samples at room temperature, the system cannot relax appreciably in

response to strain energy, whereas in nano-sized samples this can occur through the free surface. The potent result of such a mechanism is that the nano-sized samples exhibit mechanical properties foreign to room temperature monolithic metallic glasses, namely ductility and work hardening, and that these properties can be obtained by simply tuning the surface area to volume ratio. The idea that plasticity in metallic glasses is dependent on structural dynamics is also supported by numerous experiments showing its strain-rate and temperature dependence. Slower strain rates and higher temperatures conditions, marked by viscous homogeneous flow, typically lead to more ductile metallic glasses.[55–58]

Plasticity in BMGs can be achieved through introducing microstructural/heterostructural means for impeding shear band propagation,[61, 62] and plasticity in nano MGs arises due to size scaling effects from the increasing surface area to volume ratio.[43, 44] However, what remains to be realized is that both of these separate, but related, mechanisms can be utilized in conjunction. For example, nano-sized heterostructures, or nanopores, may be able to exploit both mechanisms to suppress shear banding as well as impede the propagation of existing shear bands. A mastery of this might allow us to one-day make ductile metallic glasses that both deform and harden like steels and possess superior strength and stiffness.

Chapter 4

FRACTURE OF NANO-NOTCHED WIRES

Nanomaterials have been lauded for performance enhancements in applications as diverse as energy,[63, 64] electronics,[65, 66] biotechnology[67] and even structural materials.[68, 69] Understanding nanoscale mechanics is critical for the implementation of nanomaterials in all applications (even where the application is not primarily structural) since a minimum level of mechanical robustness is necessary for prolonged operation. Many engineering materials show enhanced strength,[70, 71] ductility (in intrinsically brittle materials),[72, 73] and fracture toughness[74] when shrunk to the nanoscale. This leads to the possibility of designing strong and tough functional materials based on nanostructural building blocks. Such design principles are widely applied in nature where hard biomaterials like crustacean shells, radiolaria, and spider silk simultaneously possess remarkable strength and toughness.[75][1]

One class of promising nanosized structural materials is metallic glass because of its high strength and enhanced ductility compared to the bulk.[73, 77, 78] The fracture behavior and toughness of nanometallic glasses must also be evaluated; unpredictable catastrophic failure has been an outstanding issue that has prevented the widespread insertion of bulk metallic glasses into devices and composites.[79–81] Recent work suggests that the tensile strength of bulk and nanoscale metallic glasses may be insensitive to notches.[82, 83] The observed notch insensitivity at the nanoscale may be related to the concept of nanoscale flaw tolerance, a continuum-based theory which suggests that the strength of intrinsically brittle materials approaches its theoretical limit and does not diminish due to the presence of flaws when the sample size is reduced to a critical length scale on the order of hundreds of nanometers.[84] The theory of flaw tolerance at the nanoscale can also be applied to materials which exhibit limited plastic deformation for small yielding conditions.[85] These observations provide the impetus for an in-depth investigation of local stresses at the notch root and the mechanisms of failure in nanoscale metallic glasses.

Wendy Gu, et al.'s earlier work on fracture in ~100 nm nanocrystalline Pt nanotensile

[1] This chapter is published in [76]

samples with prefabricated flaws revealed flaw-insensitivity in strength and flaw-sensitivity of failure localization.[86] Experiments and MD simulations showed that these behaviors stem from the competition between stress concentrations at the structural flaw (external) and at discrete microstructural features such as grain boundaries (internal). Although structural flaws serve as strong stress concentrators and generally govern failure location, plasticity within the grains in nanocrystalline metals reduce the stress at the flaw to the level of the stress concentrators of microstructural origin within the structure. The fracture strengths of all nc-Pt samples were similar regardless of whether failure occurred at the structural flaw or within the microstructure. This fracture behavior arises from the combination of the discrete stress landscape within the nanocrystalline microstructure and the nanoscale sample size.[86]

Flaw-insensitivity in strength was observed when microstructural stress concentrations (e.g., grain boundaries and triple junctions) superseded the stress concentrations associated with structural flaws.[86–88] By this argument, strength should be sensitive to structural flaws in the absence of microstructural stress concentrations, such as in the case of the nanosized metallic glass samples studied in this work. The intrinsic mechanical length scale in metallic glasses is associated with clusters of ~100 atoms (i.e., a few atomic diameters in size) that serve as shear transformation zones (STZs) upon deformation. Beyond this nearly atomic scale, metallic glasses exhibit a homogeneous internal energy landscape. This means that an external stress concentrator, such as a structural flaw, should determine failure location, strength, and mechanism when the length scale of the stress concentrator exceeds the size of this atomic-level, internal stress fluctuation. In this work, we focus on elucidating the mechanisms of failure in nanoscale metallic glass containing a structural flaw through experimental nanomechanical testing and molecular dynamics simulations.

4.1 Fabrication of notched nanowires

Ni-P metallic glass nanostructures were electroplated into a poly(methyl methacrylate) (PMMA) thin film that was patterned with an array of 70-75 nm-diameter holes using e-beam lithography (Figure 4.1A).[89] A gold layer underneath the PMMA layer served as the cathode for electroplating. A 75 at. % Ni-25 at. % P metallic glass was plated by applying a 80 mA/cm^2 current between the Au-PMMA electrode and a Ni counter electrode in a nickel sulfamate-based aqueous bath as described in Chapter 1 and Appendix. Cylindrical nanocylinders were formed by plating continuously for 35 s. Notched metallic glass nanocylinders were formed by first

plating into a template continuously for 15 s, followed by four successive 5 s periods interrupted by ~10 min pauses.[86] The plating was continued until the metallic glass nanocylinders began to overgrow the PMMA thin film surface. The PMMA layer was removed after the electroplating process to leave freestanding cylindrical tensile testing samples with protrusions at the ends that serve as tension grips.

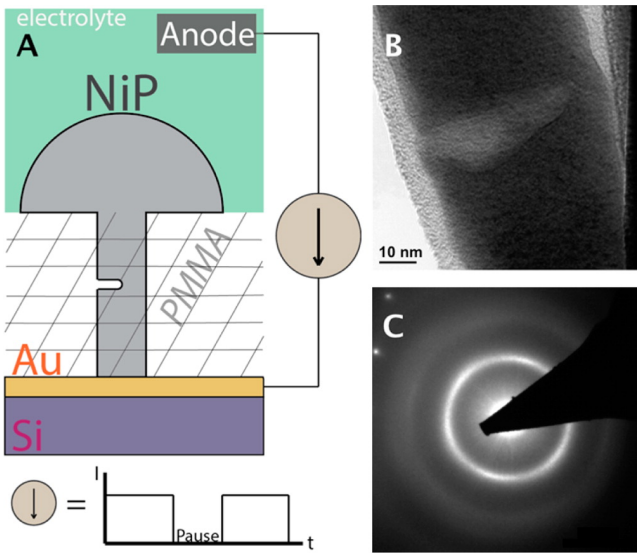

Figure 4.1: Fabrication and characterization of notched nanowires. (A) Schematic of templated electroplating of notched Ni-P nanocylinders using a 'paused' electroplating method. (B) Bright field TEM image of the notched region in a Ni-P nanocylinder. (C) Corresponding electron diffraction pattern showing the amorphous nature of the nanocylinder. Single crystal diffraction peaks are due to the Cu TEM grid.

4.2 SEM and TEM characterization

The sample and notch geometries were characterized using scanning electron microscopy (SEM) (FEI Quanta). The notched cylindrical samples had diameters of 69 ± 2 nm and lengths of 851 ± 11 nm. The notches appear as thin lines when imaged in SEM at 20 kV, so the resolution of these observations were limited to features above ~10 nm. Despite this limited resolution, small variations in notch length and height were observed qualitatively. The imaging conditions resulted in an electron beam penetration depth that was a significant fraction of the cylinder diameter and images of the notch include information both from the surface and from within the cylinder. All notched samples were fabricated using a paused electroplating methodology and contained a notch 768 ± 10 nm from the base of the cylinder. Three of the seven nanocylinders that were tested contained an additional

notch at 638 ± 12 nm from the base of the cylinder. Unnotched nanocylinders with diameters of 74 ± 3 nm and lengths of 434 ± 10 nm were also fabricated. The difference in the dimensions of the notched and unnotched samples was caused by variations in the e-beam lithographed templates used to create these samples.

Transmission electron microscopy (TEM) was used to obtain higher resolution images of the notches and to analyze the microstructure of the nanocylinder. Samples were transferred from the growth substrate to a Cu TEM half-grid with minimal mechanical perturbation and no focused ion beam (FIB) damage (details of TEM sample preparation are included in the Supporting Information). Bright- and dark-field TEM images and electron diffraction patterns confirmed that the nanoscale metallic glass samples were amorphous (Figure 4.1B and C).[77] A small amount of ordering was observed and is likely associated with crystallinity within the e-beam deposited C and W layers on the surface of the Ni-P nanocylinder. The spots visible in the upper left corner of the diffraction pattern in Figure 4.1C are associated with the Cu TEM grid supporting the nanocylinders. The notch shown in Figure 4.1B has a height of 10 nm and a rounded notch root similar to that shown schematically in Figure 4.1A. The width and depth of the notch could not be accurately measured using the TEM because of difficulties distinguishing between surface features and those within the nanostructure. Qualitatively, the TEM images revealed that the notch extends a significant distance across the diameter of the sample and that the structure is thinner at the notch than at surrounding areas based on diffraction contrast. No change in the amorphous structure between the notch region and the rest of the structure was observed.

4.3 *In-situ* mechanical tests

In situ SEM uniaxial tension tests were performed at a nominal strain rate of 0.001 s^{-1} on notched and unnotched Ni-P nanocylinders using the InSEM system.[90] Unnotched Ni-P samples were glued to the substrate using a small amount of e-beam deposited W (Nova 200, FEI) (Figure 4.2A). It was not necessary to glue notched Ni-P samples because they always broke within the cylindrical gauge length at stresses lower than the interfacial strength between the sample and the underlying substrate (Figure 4.2C). Videos of the in situ SEM mechanical experiments can be found in the Supporting Information of this manuscript online.[76]

Unnotched, ~75 nm diameter Ni-P nanocylinders showed ~3% post-elastic deformation in tension in contrast with the brittle failure observed in wider Ni-P metallic

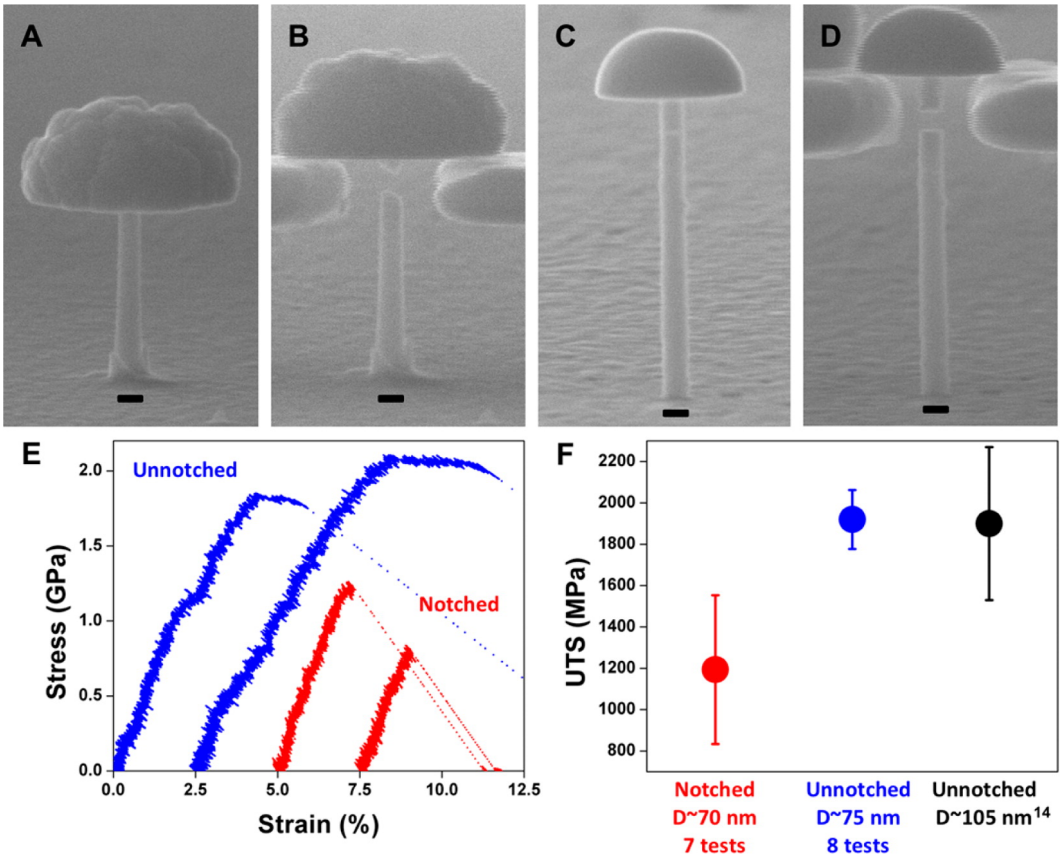

Figure 4.2: *In-situ* tensile tests on notched nanowires. SEM images of an unnotched Ni-P nanocylinder (A) before and (B) after tensile testing and a notched Ni-P nanocylinder (C) before and (D) after tensile testing. The scale bar represents 75 nm. (E) Characteristic stress-strain curves for notched (red) and unnotched Ni-P nanocylinders (blue). (F) Comparison of the UTS of notched and unnotched Ni-P nanocylinders with ~70 nm diameters and unnotched Ni-P nanocylinders with a ~105 nm diameter.[77]

glass samples of the same composition.[77] The ultimate tensile strength (UTS) of the eight tested unnotched cylinders was 1.9 ± 0.1 GPa, consistent with previously reported strengths of thicker, 105 nm diameter Ni-P metallic glass nanocylinders.[77] Failure in the unnotched samples occurred through necking, followed by shear banding resulting in an angled fracture surface (Figure 4.2B). The fracture planes were inclined, on average, by ~° relative to the loading axis but showed variation in the 5-42° range, as measured from the SEM images. We note that, because the fracture surface was not always aligned with the viewing direction, the values reported here should be considered lower bounds on the fracture angle for each sample.

The notched Ni-P nanocylinders always broke at the notch. Their average failure stress, 1.2 ± 0.4 GPa, was significantly lower than that of the unnotched nanocylin-

ders. Six of the seven tested notched samples broke at an UTS lower than that of the unnotched pillars. One notched pillar broke at an UTS of 1.9 GPa. Notched samples that failed at ~1.2 GPa exhibited limited plastic strain, 0.3%, as compared to 3% plastic strain in the unnotched nanocylinders (Figure 4.2E). This is a clear demonstration that the stress concentration at the notch plays a key role in the deformation mode. Nanoscale metallic glasses have previously been shown to exhibit increased ductility, but no increases in strength when reduced below ~100 nm in size.[73, 91] If the only role of the notch was to decrease the effective diameter and the cross-sectional area of the nanocylinder, then increasing the notch size should lead to higher ductility. Figure 4.2F proves that the Ni-P samples are in a size-independent regime with regards to strength, because decreasing the unnotched sample diameter from ~105 nm to ~75 nm does not change the UTS (~1.9 GPa in both cases). The decrease in UTS observed in the notched ~70 nm samples (~1.2 GPa) must be due to the effect of the notch rather than due to a reduction in the sample diameter.

The fracture surface in the notched samples was inclined 4° relative to the loading axis on average, with all samples breaking at angles within the 0°-10° range (Figure 4.2D). Part of the observed "fracture surface" may, in fact, be the surface of the notch; this is difficult to quantify because the notch sizes could not be precisely determined.

4.4 Molecular dynamics simulations

To elucidate the physical origin of the effect of the notch on failure, we performed large-scale molecular dynamics (MD) simulations on notched and unnotched $Fe_{75}P_{25}$ metallic glass nanocylinders. The atomic interactions within the Fe-P metallic glass were modeled using the embedded atom method (EAM) potential parametrized by Ackland et al.[92] We focus on Fe-P metallic glasses rather than Ni-P glasses here because no Ni-P potentials that have been validated against measured mechanical properties of Ni-P are available, while one does exist for Fe-P. Iron and nickel have similar electronegativity: both are transition metals from the same row of the periodic table, and the bonding in $Fe_{75}P_{25}$ and $Ni_{75}P_{25}$ is very similar. On this basis, we expect that Fe-P is a reasonable surrogate for Ni-P for MD simulations. However, like for MD simulations based upon any type of empirical potentials, the details of the predictions should be viewed with some skepticism. The high strain rate used in the MD simulations (5×10^7 s^{-1}) may also influence observed deformation mechanisms. For these reasons, we focus on major mechanistic features and trends in behavior when interpreting MD simulation results.

Simulations were performed using the large-scale atomic/molecular massively parallel simulator (LAMMPS).[93] Details of the molecular dynamics simulations are provided in the Supporting Information. The simulated unnotched samples were constructed as cylinders with a diameter of 40 nm and a length of 120 nm (Figure 4.3A). The notched sample was formed by cutting a rounded notch with length of 5.7 nm and height of 3.4 nm out of the unnotched sample (Figure 4.3E). Deformation and failure of the simulation samples were analyzed in terms of the local atomic von Mises shear strain, ϵ_{vM}.[94, 95] Visualization of ϵ_{vM} has been widely used to investigate shear band (SB) formation in metallic glasses.[94] Figure 4.3A-H show ϵ_{vM} for a central cross section of representative unnotched and notched nanocylinders at different applied strains, ϵ. Figure 4.3A-D show that the distribution of ϵ_{vM} in the unnotched sample is uniform up to the UTS, which corresponds to $\epsilon_{unnotchedUTS} \sim 10.8\%$. Beyond the UTS, a shear band forms, which leads to failure at an oblique angle ($\sim 45°$) relative to the loading direction. The notched nanocylinder does not fail through shear banding, but instead fails by crack initiation and propagation from the notch root after reaching the UTS (Figure 4.3E-H). The crack propagates from the notch in a direction orthogonal to the applied load. The engineering stress-strain data for both the unnotched and notched nanocylinders are shown in Figure 4.3I. The UTS for the unnotched and notched samples is attained at applied strains of $\epsilon_{unnotchedUTS} \sim 10.8\%$ and $\epsilon_{notchedUTS} \sim 5.8\%$, respectively. The UTS of the notched sample was ~25% lower than that of the unnotched sample. MD tensile test videos can be found in the Supporting Information.

4.5 Discussion of results

The MD simulations appear to be in excellent agreement with the experimental observations and unambiguously demonstrate that the notch governs the failure mode and mechanism in nanoscale metallic glasses. Both simulations and experiments show that the unnotched nanocylinders failed in a ductile fashion via shear banding, with the fracture surface oriented at an oblique angle with respect to the loading axis. The notched nanocylinders failed in a brittle manner via crack propagation from near the notch root, horizontally across the sample. The tensile strength of the notched sample was significantly smaller than that of the unnotched sample in both experiments (36% reduction) and simulations (25% reduction). The observed reduction in strength and transition in failure mode indicate that the notched metallic glass nanocylinders are notch sensitive.

MD simulations were previously performed on Cu-Zr nanoscale metallic glasses in

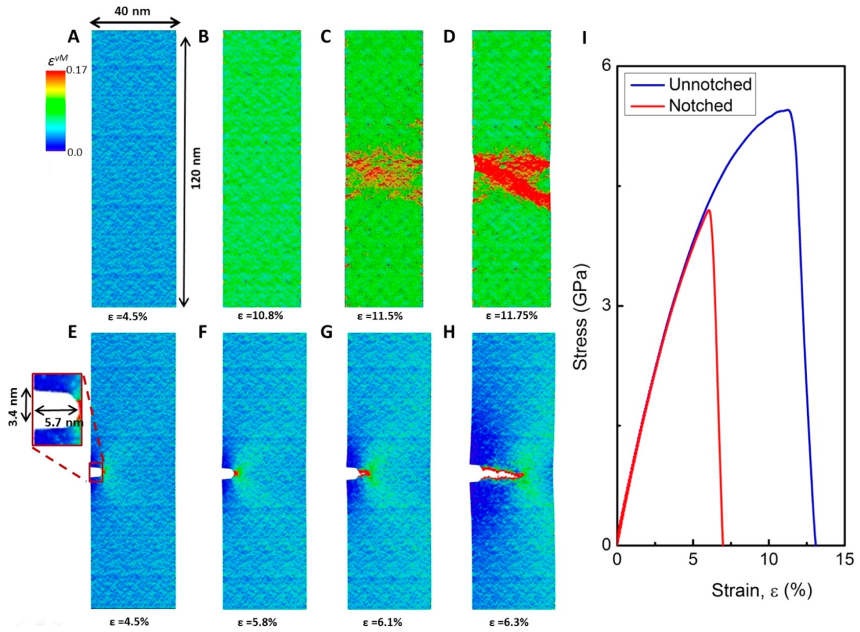

Figure 4.3: Molecular dynamics simulations of notched nanowires. Atoms are shaded according to their von Mises strain ϵ_{vM} in a cross-section of the unnotched sample at (A) ϵ = 4.5% (uniform ϵ_{vM}), (B) ϵ = 10.8% (strain at ultimate tensile stress), (C) ϵ = 11.5% (at the inception of shear band), and (D) ϵ = 11.75% (well-developed shear band). For comparison, ϵ_{vM} is plotted for the notched sample at (E) ϵ = 4.5% (elevated local strain at the notch), (F) ϵ = 5.8% (strain at the ultimate tensile stress and beginning of crack formation), (G) ϵ = 6.1% (crack propagates horizontally), and (H) ϵ = 6.3% (failure via crack propagation). (I) Stress-strain curves corresponding to the simulated tensile tests of unnotched and notched amorphous samples.

which failure always initiated from rounded flaws.[83] Our results agree with these simulations in fracture location but not in failure strength. The load at fracture was normalized by the cross-sectional area at the flaw to obtain a normalized UTS in the Cu-Zr metallic glass nanoscale sample. This normalized failure strength was found to be independent of notch size. The notch in the Fe-P metallic glass nanocylinders reduces the cross-sectional area of the cylindrical sample by 9%, but reduces its strength by 25%, which indicates notch-sensitivity at the nanoscale in this material. This difference in behavior is indicative of a difference in the underlying mechanism of failure between notched Cu-Zr and notched Fe-P glasses.[96] Cu-Zr deforms through shear banding that initiates at the notch,[83] while notched Fe-P fails through void formation and growth as shown in Figure 4.4. The plastic shear banding in Cu-Zr is able to relieve stress at the notch such that the stress concentration at the notch has a negligible effect on failure strength. Similarly,

stable shear bands propagate from notches in certain bulk metallic glasses which serves to strengthen the metallic glass and lead to notch insensitivity.[82] The stress relaxation mechanism of shear banding is unavailable to notched Fe-P so flaw sensitivity is observed instead.

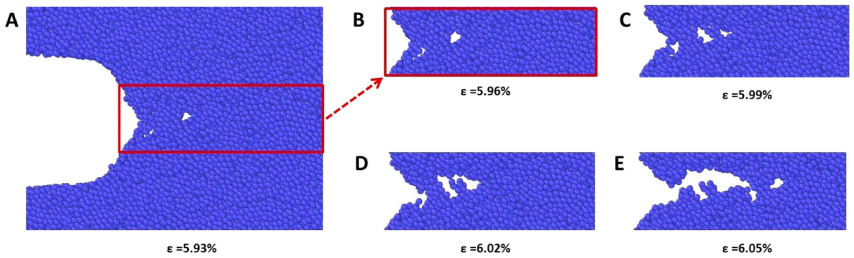

Figure 4.4: Detailed view of the deformation in notched nanowires. (A) Formation of atom-scale voids ($\epsilon = 5.93\%$), (B) growth of voids ($\epsilon = 5.96\%$), continued growth of voids and formation of additional voids at (C) $\epsilon = 5.99\%$ and (D) $\epsilon = 6.02\%$, and (E) coalescence of voids ($\epsilon = 6.05\%$). Images show a cross-section of the simulation nanocylinder.

Figure 4.4A-E shows several close-up views of the notch root region at different stages of loading. Microscopic voids were nucleated in front of the notch root at an applied strain of $\epsilon = 5.93\%$, a value slightly above $\epsilon_{notchedUTS} \sim 5.8\%$, and subsequently grew while additional small voids emerged (Figure 4.4A-C). The coalescence of these voids and their linkup with the dominant crack led to crack propagation (see Figure 4.4D-E) and eventually caused fracture and the formation of a horizontal fracture surface. Although fracture is microscopically ductile (because it occurs through void nucleation, growth and coalescence), the overall failure process can be viewed as brittle crack propagation because the total amount of plastic deformation is very small.

We postulate that the observed cavitation was caused by the substantial stress triaxiality ahead of the notch. The atomic stress triaxiality is defined as $\eta = \frac{Tr(\sigma)}{3\sigma_{vM}}$, where σ is the atomic stress tensor. When η is large, hydrostatic stress dominates, leading to void nucleation and growth. When η is small, shear deformation dominates, and shear banding is expected.[97, 98] We calculated η in both the notch root region (red region in the inset of Figure 4.5A), as well as for the whole sample excluding the notch root area (blue region in Figure 4.5A). Figure 4.5A shows P(η), the stress triaxiality distribution in the notch root area (red curve) in comparison with that for the remainder of the sample (blue curve) at an applied strain of $\epsilon = 4.5\%$. It is seen that η at the notch root is shifted toward more positive values and its average increased by almost 300% to 0.38 (red dash line) from $\eta = 0.13$ as compared with the rest of

the sample (blue dashed line). Figure 4.5B shows the normalized value of average stress triaxiality, $\frac{\eta_{notch-root}}{\eta_{remainder}}$, as a function of applied strain, ϵ. This figure indicates that during the uniaxial tensile test, there is a much greater degree of volumetric expansion at the notch root as compared with rest of the sample, which drives the nucleation and growth of the voids. Figure 4.5C-D shows the spatial distribution of η in the cross-section of the notched nanocylinder at the UTS (corresponding to ϵ = 5.8%). Much higher values of η are observed in front of the notch root. Voids are nucleated in these regions of large η near the notch root at a very small increment in the applied strain (to 5.9%), as seen in Figure 4.5E.

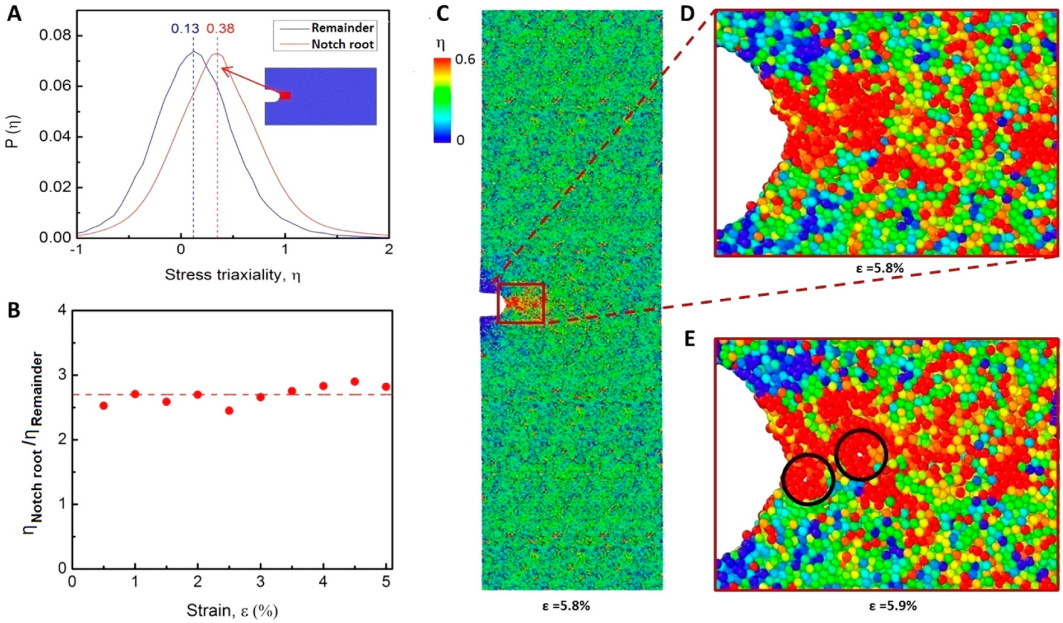

Figure 4.5: Stress triaxiality in notched nanowires. (A) Plot of the probability density of the stress triaxiality, P(η), at the notch root (red curve) in comparison with the P(η) for the remainder of the sample (blue curve) at an applied strain of ϵ = 4.5%. P(η) is calculated for a 2 nm thick slice through the cylindrical sample. The P(η) at the notch root is calculated for the region located in front of the notch root (red area in the inset). The data for the remainder of the sample are calculated for all other atoms in the sample (blue region in inset). (B) The normalized value of average stress triaxiality, $\frac{\eta_{notch-root}}{\eta_{remainder}}$, as a function of applied strain, ϵ. The spatial distribution of η in (C) the cross section of the notched nanocylinder at the strain corresponding to the UTS, (D) near the notch at the UTS, and (E) near the notch at a slightly higher strain ϵ = 5.9%. Voids nucleate at the notch root due to high localized η (indicated by the black circles).

Our results indicate that flaws are critical to the failure strength and failure mechanism in this nanoscale metallic glass. Recent theory suggests the emergence of flaw tolerance in solids at very small length scales which applies directly to brit-

tle materials.[84] The amorphous system examined here shows nontrivial localized plasticity through either shear banding or voiding. The present observations demonstrate that the effects of flaws are consistent with classical analyses and that these are remarkably robust and applicable down to the scale of the smallest man-made mechanical structures. While our earlier work showed that nanocrystalline metals can be flaw-tolerant in terms of strength,[86] this work conveys that the flaw tolerance is associated with the specific discrete microstructure rather than with the nanoscale sample size. The absence of a discrete microstructure, as is the case for the amorphous metallic glasses in this work, implies no flaw-tolerance in nanoscale materials that exhibit localized plasticity.

4.6 Summary

In summary, we explored the deformation mechanism and failure modes of notched and unnotched amorphous metallic glass nanostructures under uniaxial tension in experiment and atomistic simulation. Structural flaws reduce sample failure strength and are critical to the failure location and failure mode. In the unnotched nanocylinders, shear band formation led to failure at an oblique angle with respect to the loading direction. The notched nanocylinders showed virtually no ductility and failed via crack initiation and propagation along the extension of the notch root. We found that the nominally brittle propagation of cracks in the notched samples was a consequence of void nucleation, growth, and coalescence in response to the large stress triaxiality at the notch root. This work unambiguously demonstrates that the deformation mode and failure strength of nanostructures depends sensitively on the presence of structural flaws, even in the absence of discrete microstructural features. These findings demonstrate that flaw-insensitivity is not a general feature of nanoscale mechanical systems; classical models that describe the effects of flaws on failure can be applied at the nanoscale provided that localized plasticity can readily occur. An important caveat is that, even when localized plasticity is possible, discrete microstructural features in nanocrystalline materials can lead to internal stress concentrations that make material strength flaw-insensitive. Future nanotechnologists must take flaw-sensitivity at the nanoscale into account when designing the mechanical aspects of nanostructured materials and devices.

4.7 Low temperature behavior of metallic glass lattices

Metallic glasses (MGs) are amorphous alloys that are highly regarded for structural applications because of some of their favorable mechanical properties such as high

strength and high elastic limit.[99–103] However, most bulk MGs are brittle and fail catastrophically under tensile load because there are no effective plasticity mechanisms to suppress the sudden initiation and propagation of shear bands or cracks.[102–104] This lack of plastic deformability of MGs significantly limits their use in structural applications. Conventional toughening methods, for instance, making a composite with metallic phases, could improve the ductility of MGs, but the use of ductile and weak second phases usually degrades the yield strength.[105–107] Due to the recent interests in nanotechnology, the nanoscale size effects on the mechanical properties of MG materials have been extensively studied,[108–110] and it has been reported that nanosized MGs can exhibit extensive ductility without sacrificing the yield strength even under tensile stress.[111–113] Uniaxial mechanical tests of Pd-Si, Zr-based, and Ni-P MG nanopillars revealed a brittle-to-ductile transition by size reduction down to ∼100 nm in diameter.[111–113] Surprisingly, Zr-based and Ni-P MG nanopillars exhibit necking and strain hardening in uniaxial tensile tests.[112–114] In addition, radiation damage experiments at the nanoscale shows that MG nanopillars do not suffer from embrittlement when subjected to radiation damage with a Ga+ ion beam.[113–116] This is in contrast to high-strength conventional metals, which become brittle when exposed to high-energy radiation.[117–120] Unfortunately, these emergent phenomena of excellent resistance to brittleness in MGs are available only at the nanoscale. In order to harness this "smaller is more ductile" behavior and to proliferate it onto materials with large-scale dimensions, it is necessary to create a macroscopic meta-material that consists of nanosized components.[2]

Recent development in laser lithography and thin film deposition techniques has enabled the fabrication of large-scale meta-materials, such as hollow-tube microlattices or nanolattices. Their overall dimension ranges from micrometer to centimeter, but the tube-wall thickness of each hollow member is submicron.[121–126] Thus, the physical properties of these meta-materials can be controlled by the configuration of the lattice structure as well as the wall thickness of hollow members. Size reduction in MGs brings about the brittle-to-ductile transition, which suggests that MG meta-materials with nanoscale wall thicknesses would possess entirely different mechanical responses to bulk MGs. In particular, MG meta-materials with tube-wall thickness <100 nm are expected to become ductile macroscopic meta-materials, which cannot be easily achieved from bulk monolithic MGs.

[2]This chapter is published online at DOI: 10.1021/acs.nanolett.5b01034

In this chapter, we describe hollow-tube cubic-shaped octet $Cu_{60}Zr_{40}$ metallic glass nanolattices with the overall dimensions of 65 μm × 65 μm × 65 μm, and studied their mechanical behavior for three different hollow tube-wall thicknesses, 20, 60, and 120 nm, at two different temperatures, 298 and 130 K. The uniaxial compression experiments revealed two distinct transitions in deformation mode at room temperature: (1) brittle-to-ductile transition between 120 and 60 nm in wall thickness and (2) plastic-to-elastic transition between 60 and 20 nm in wall thickness. Also, we found that at 130 K, the deformation mode changes from brittle failure to elastic buckling without plastic deformation from 120 and 60 nm to 20 nm in wall thickness. Molecular dynamics simulations and analytical modeling were performed to understand these unique transitions in deformation mode and the effects of temperature in the context of size effect on the plasticity of MGs and elastic instability of hollow tube member.

$Cu_{60}Zr_{40}$ binary MG system was chosen because of its excellent glass forming ability of Cu-Zr systems.[104] The general description of nanolattice fabrication is available elsewhere,[122, 123, 125] and the only major difference is the deposition method. We used the radio frequency magnetron to co-deposit copper (Cu, 92 W RF power) and zirconium (Zr, 224 W RF power) at 2 $\times 10^{-5}$ Torr or lower, and the processing pressure was 3 mTorr of Ar gas on the polymer nanolattices.[127] After the sputter deposition, the polymer core was exposed by using focused ion beam (FIB) in a FEI Nova 600 Nanolab to mill away the surfaces along three of the sides of the nanolattice. The exposed core was then etched out in an oxygen plasma etcher for 2.5 h at 100 W and 300 sccm oxygen flow. The composition of the thin Cu-Zr film was confirmed as nearly $Cu_{60}Zr_{40}$ by energy dispersive X-ray spectroscopy in scanning electron microscope (SEM) and transmission electron microscope (TEM). Figure 4.6a shows the SEM image of an MG nanolattice with the wall thickness of ∼120 nm, and Figure 4.6b shows the individual hollow members. The HRTEM image of the inset in Figure 4.6b ensures the atomic configuration to be amorphous.

In-situ compression experiments at the room and cryogenic temperatures were performed in a specialized in situ nanomechanical instrument. We have custom-built an instrument to conduct in situ nanomechanical experiments at cryogenic temperatures by retrofitting our Quanta SEM (FEI, OR) with a nanomechanical arm, InSEM (Nanomechanics, Inc., TN), and a temperature control system (Janis Research, MA). Details about this cryogenic experimental setup and the equipment are available elsewhere.[128, 129] Uniaxial compression experiments were conducted

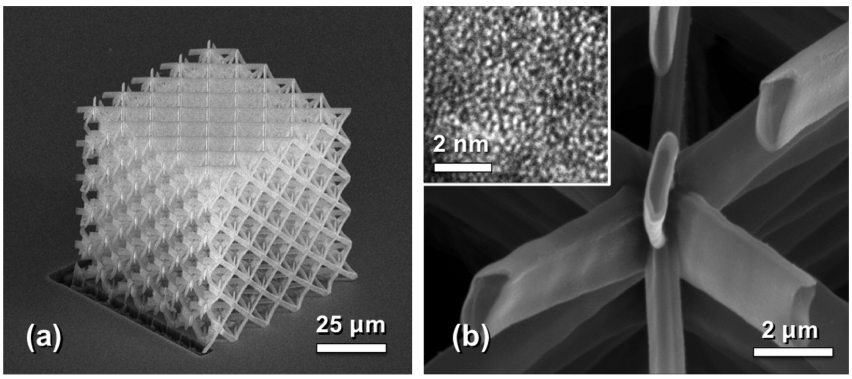

Figure 4.6: SEM images of MG nanolattices. (a) Hollow-tube octet $Cu_{60}Zr_{40}$ nanolattice and (b) the magnified view of hollow lattice members. The inset in b is the HRTEM image of atomic configuration.

at 298 and 130 K at a prescribed nominal displacement rate of 100 nm/s, which corresponds to the engineering strain rate of about 1.5 $\times 10^{-3}$ s^{-1}. We ensured that the thermal drift within the chamber was always less than 1 nm/s, which was possible by simultaneous cooling of the sample stage and of the indenter tip. Note that, in this study, we are going to focus on the deformation modes (brittle fracture, plastic deformation, and elastic instability) more than the strength as a function of relative density that most nanolattice works have considered.

Figure 4.7a shows the engineering stress-strain data for the compression of $Cu_{60}Zr_{40}$ nanolattices with the wall thickness of ~120 nm. The large strain bursts correspond to the brittle collapse of nanolattice layers. The snapshots in Figure 4.7a clearly show catastrophic layer-by-layer collapse during deformation of the lattice (see also Supporting Information 1). In contrast, Figure 4.7b shows that the nanolattices with the wall thicknesses of ~60 nm had a smoother stress-strain behavior with the layer-by-layer collapse commencing in a smooth, noncatastrophic manner (see also Supporting Information 2). These results in Figure 4.7a,b indicate that a transition from catastrophic and discrete deformation to smooth plastic flow occurs at some critical metallic glass wall thickness between 60 and 120 nm. Some MG nanolattices with 60 nm in thickness exhibit the relatively large strain burst at room temperature. Cross-linking process and metal deposition could produce uncontrollable local variation of surface structures, structural defects, or layer thickness, which would lead to the variation in mechanical behavior, such as large strain bursts. In this paper, 'brittle' means catastrophic failure of the layers without any noticeable plastic strain and is represented by a large strain burst with displacement magnitude equal to or larger than the gap between two adjacent layers. 'Ductile' means smooth plastic

flow and is represented by strain events with the displacement magnitudes much smaller than the gap between two adjacent layers. In this case, the hollow members do not catastrophically fracture and instead plastically bend via stable shear or homogeneous deformation.

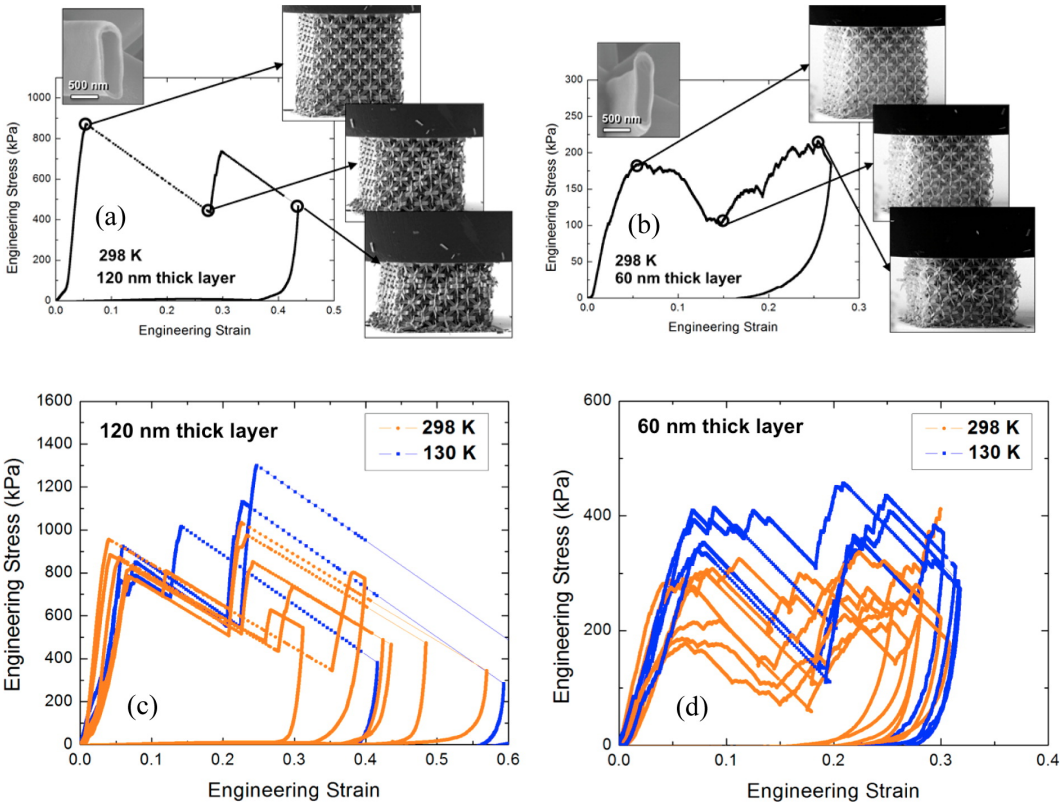

Figure 4.7: Engineering stress-strain curve of MG nanolattices. Wall thickness of (a) 120 nm and (b) 60 nm at 298 K. Insets include the cross-section of hollow member and snapshots during mechanical deformation. (c) Engineering stress-strain curves of MG nanolattices with the wall thickness of (c) 120 nm and (d) 60 nm at 298 and 130 K.

At room temperature (298 K), the average extent of the strain bursts in 60 nm thick samples is significantly smaller than that in 120 nm thick samples. This indicates that the plasticity and possible fracture events in the 60 nm thick samples are local, rather than global; in contrast, the 120 nm thick samples experience macroscopic layer collapse, which correspond to the extensive strain bursts. It is useful to inquire whether the small strain bursts in 60 nm thick samples are caused by local brittle fracture or by local plastic deformation. Cryogenic experiments are useful in uncovering this information because plastic deformation at low temperatures is suppressed, and if local brittle fracture were to drive the small strain bursts, no significant differences would be observed in the stress-strain data obtained at RT and

130 K. The distinct difference in the stress-strain data for the 60 nm thick samples at cryogenic and room temperatures can prove the existence of plastic deformation, which is temperature-sensitive. Thus, we performed uniaxial compressions on samples with the same wall thicknesses of 120 and 60 nm at 130 K to assess whether plastic deformation that was observed in the 60 nm thick samples at room temperature would be suppressed. Figure 4.7c shows the engineering stress-strain data for the experiments on the 120 nm thick samples at 298 and 130 K. The deformation appears to be discrete and jerky, with material failing in brittle manner at both temperatures (see also Supporting Information 3). Figure 4.7d shows the same data for the 60 nm thick samples, whose behavior is distinct at each temperature: discrete at 130 K and smooth at 298 K (see also Supporting Information 4). These results unambiguously point to the emergence of brittle-to-ductile transition that occurs in the $Cu_{60}Zr_{40}$ metallic glasses between 120 and 60 nm.

Surprisingly, $Cu_{60}Zr_{40}$ nanolattices with the nominal wall thicknesses of 20 nm recovered fully at both 298 and 130 K even upon severe compression. The SEM images in Figure 4.8 taken during the compression of the nanolattices at 298 K (Figure 4.8a-f) and 130 K (Figure 4.8g-l) show that the weakest regions in the MG nanolattices are completely compressed until adjacent layers come in contact with one another, which corresponds to significant local strain [see also Supporting Information 5 (298 K) and 6 (130 K)]. Nevertheless, the deformation was fully shape-recoverable, a result similar to that reported for nanocrystalline Ni microlattices,[121] metallic glass Ni-P microlattices,[126] and alumina nanolattices.[123] The full shape recovery of 20 nm thick samples implies that some fraction of members exhibit purely elastic behavior without the loss of strain energy. Note that the stress-strain data of this ~20 nm thick case are not presented in this paper due to the data reliability issue, but they are available as the Supporting Information 7. We realized that it is difficult to achieve a uniform 20 nm thickness on the 3-D polymer scaffold with our sputtering method. Furthermore, in the middle of sample fabrication, the focused-ion-beam milling process redeposits Si atoms at the bottom parts of nanolattices, which could affect the overall mechanical properties of nanolattices especially for the thin 20 nm thick samples. In situ observation in Figure 4.8 clearly demonstrates the full shape-recovery even after the significant amount of deformation (nearly over 70% from the image correlation). Therefore, at room temperature, the experimental results of $Cu_{60}Zr_{40}$ MG nanolattices show the brittle-to-ductile transition between 120 and 60 nm in thickness, and PSR (partial shape recovery)-to-FSR (full shape recovery) transition between 60 and 20 nm in

thickness. Also, at 130 K, the brittle-to-ductile transition does not occur, and only brittle (also, PSR)-to-FSR transition occurs between 60 and 20 nm in thickness. Brittleness of our nanolattices concerns the catastrophic collapse of layers during loading. Thus, it does not necessarily imply that no shape recovery occurred during unloading. During unloading, shape recovery would occur if the unfractured part of nanolattices were elastically strained.

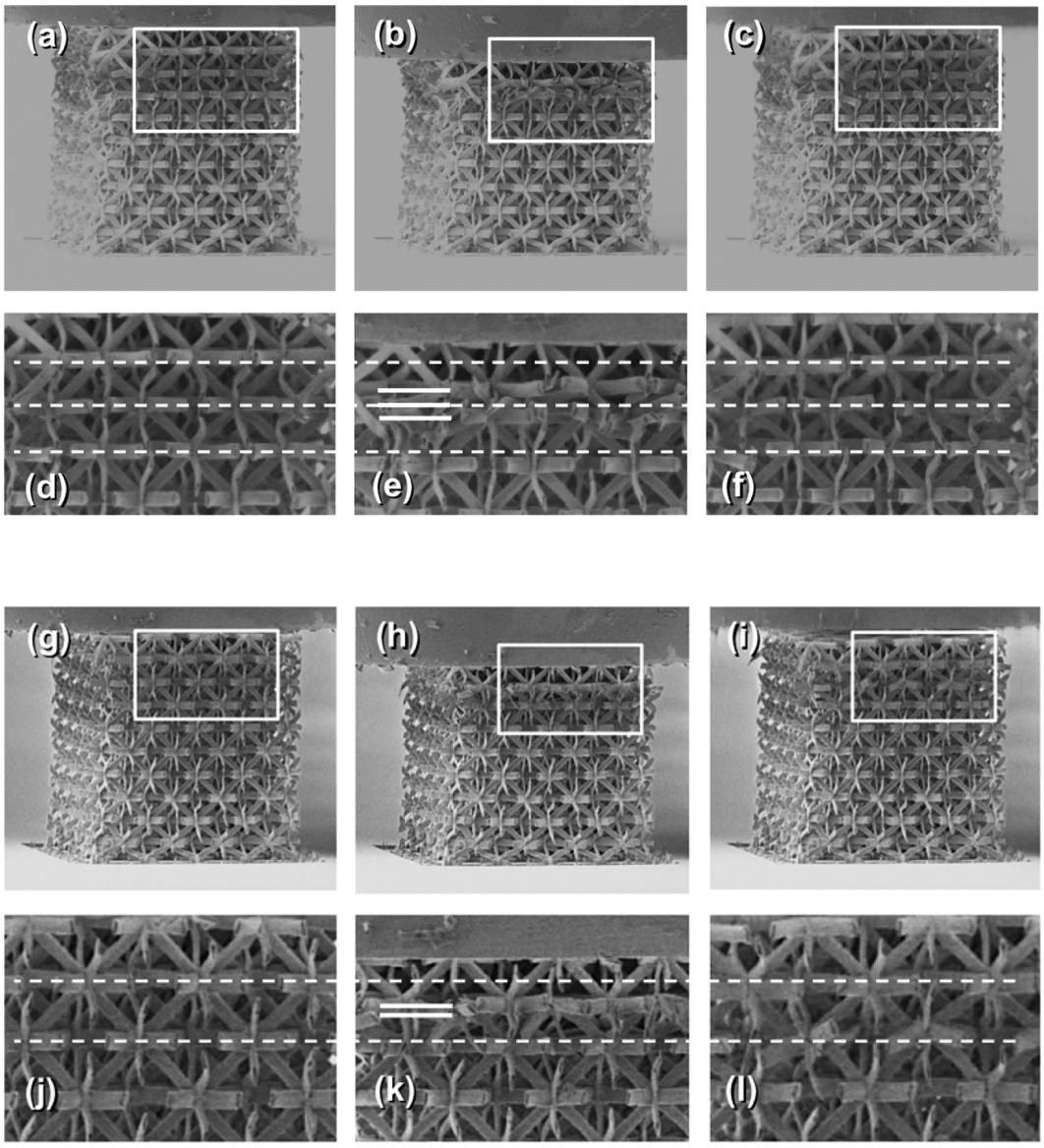

Figure 4.8: Snapshots of *in situ* deformation of MG nanolattices with the wall thicknesses of 20 nm. (a) Hollow-tube octet $Cu_{60}Zr_{40}$ nanolattice and (b) magnified view of hollow lattice members. The inset in b is the HRTEM image of atomic configuration.

To further study the thickness- and temperature-dependence of the MG deformation

at the atomistic level, we performed large-scale molecular dynamics (MD) simulations. Note that the deformation mechanisms are controlled mainly by the shell thickness. Thus, we focus on the mechanical behavior of shell components as the simplest model system.

The atomic interactions within the Cu-Zr metallic glass were modeled using the embedded atom method (EAM) potential parametrized by Mendelev et al.(32) The details of our simulations and sample preparation are provided in the Method section. In our MD simulations, we focus on the compression behavior of the MG samples, which allows us to capture the elastic buckling in addition to the major stress and failure modes experienced by the hollow members.

Figure 4.9 shows the effect of sample aspect ratio on the failure mechanisms of the metallic glass under compression at room temperature (300 K) and cryogenic temperature of 130 K. The dimensions of samples used for these simulations are 120 nm in the z direction (i.e., sample length, L), 5 nm in the y direction, and a varied thickness (w) of 40, 20, and 10 nm in the x direction. These configurations correspond, respectively, to aspect ratios (AR = L/w) of 3, 6, and 12. For the convenience of our discussion, hereafter we call the samples with AR of 3, 6, and 12 as Sample A, Sample B, and Sample C corresponding to the panels a, b, and c of Figure 4.9, respectively. Compression loading was applied in the z direction of these samples with PBCs along the z and y dimensions, while the samples had free surfaces in the x direction. It should be noted that our computational quasi-three-dimensional models mimic the shell components of the experimental nanolattices. The application of PBCs in the z direction captures the long tube geometry, while applying PBCs with zero stress in the y direction reflects the real stress state in the circumferential direction of the tube. Moreover, the existence of free surfaces in the x direction mimics the thickness of the tube. Hence, the selected simulation thicknesses of 10, 20, and 40 nm are comparable with the true thickness of the tube shell components of the nanolattices.

Figure 4.9a1,b1,c1 shows the engineering stress-strain curves at 300 and 130 K for Samples A, B, and C, respectively. Moreover, to understand the deformation and failure mechanisms at the atomic scale, we further analyzed the von-Mises atomic shear strain, ϵ_{vM}, with respect to the unloaded sample. The corresponding snapshots of the atomic deformation process at different values of the applied compression strain, ϵ, and temperatures (130 and 300 K) are presented in the panels (a2, a3), (b2, b3), and (c2, c3) of Figure 4.9 for Samples A, B, and C, respectively. Figure 4.9a2

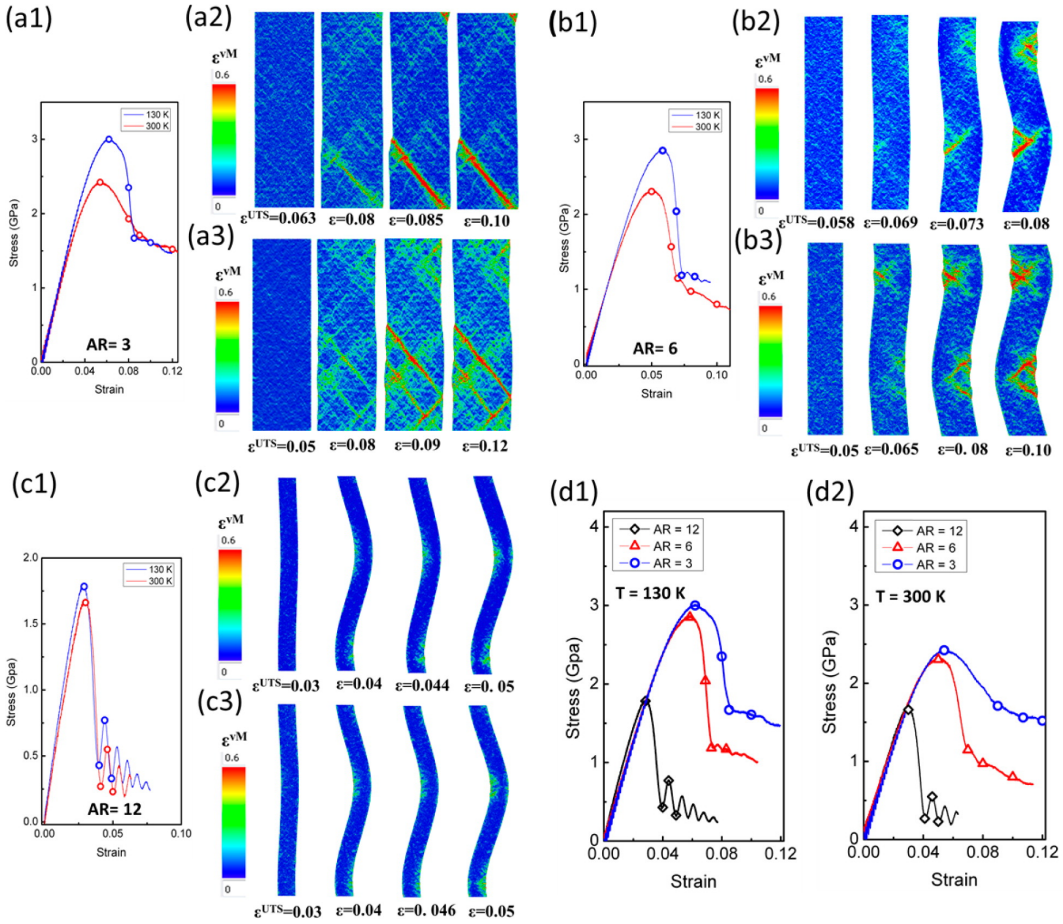

Figure 4.9: MD simulations of nanolattices at various temperatures. (a1) Engineering stress-strain curves for Sample A with aspect ratio (AR = 3) during compression test at 130 and 300 K. (a2, a3) The snapshots of von-Mises atomic strain, ϵ_{vM}, for Sample A at (a2) 130 K and (a3) 300 K and different applied compression strains which are indicated by the hollow circles in (a1). The same information as panel a is presented in panel b and panel c for Sample B (AR = 6) and Sample C (AR = 12), respectively. (d1, d2) Engineering stress-strain curves for Samples A, B, and C during compression test at (d1) 130 K, and (d2) 300 K. For all of these simulations, supplementary movies are provided.

clearly shows that the mechanism of failure in Sample A with low aspect ratio (AR = 3) at the cryogenic temperature is through initiation and propagation of a single shear band (SB) along the principle shear direction (i.e., $\sim 45°$), indicating a brittle shear banding failure mode. From Figure 4.9a3, it can be seen that, by increasing the temperature to 300 K, the failure of the sample is also due to formation of a dominant shear band along the whole width of the sample. Moreover, Figure 4.9a3 demonstrates that, by increasing the temperature, more plastic deformation occurs in the sample, resulting in a smoother stress-strain curve (more ductile) at room

temperature. This observation is in agreement with the experimental results of our 60 nm thick nanolattices showing that the nanoscale metallic glasses at room temperature exhibit some level of ductility before they break through shear banding. According to our MD simulation work on Ni-Al MG nanopillars (chapters 1 & 2), the ductility of MGs at the nanoscale is strongly related to the formation and annihilation of free volume near the free surface.[114] The size effects of ductility may emanate from the higher surface area-to-volume ratio in thinner cylinders, which allows for sample-wide homogeneous-like deformation before significant shear localization can occur. Free volume dynamics is highly temperature-dependent because free volume creation, annihilation, diffusion are thermally activated processes. Thus, an increase in temperature may enhance free volume dynamics near the free surface, leading to more diffuse shear deformation.

Figure 4.9b1 shows the engineering stress-strain curves at 130 and 300 K for Sample B, with intermediate aspect ratio (AR = 6). At a given temperature, a comparison between the peak stress of Sample B and that of Sample A indicates that Sample B fails at a lower stress level than Sample A (for a better comparison, see Figure 4.9d1,d2). From Figure 4.9b2,b3, it can be seen that after the peak stress in Sample B, and before the formation of the complete shear band along the whole width of the sample, the sample exhibits structural instability in the form of buckling. Then, the partially formed shear bands intersect and remain incomplete while the sample further buckles. Comparison of Figure 4.9b2 and b3 indicates that elevating the temperature leads to further development of plastic deformation (more ductility) in the sample and a smoother stress-strain curve at the peak. To summarize, for Sample B (AR = 6), we observe buckling and postbuckling plasticity leading to a ductile failure.

Figure 4.9c1 shows the engineering stress-strain curves for Sample C with high aspect ratio (AR = 12) at 130 and 300 K. It can be seen that decay of the peak stress in Sample B is sharp even at room temperature. The atomistic deformation in Sample C (see Figure 4.9c2,c3) reveals that no shear band (even partially) forms in this sample. At both temperatures, after the peak stress, the sample is still almost in the elastic mode (indicated by deep blue color) while it is undergoing buckling. Another interesting feature of Figure 4.9c1 is the pronounced serrated tail of the curves at both temperatures. Our analysis of the deformation in this case (see the Supporting Information 8 and 9) reveals that this serrated tail is corresponding to a spring-like elastic vibration of the sample during the continuously applied

compressive strain, which indicates the elastic nature of this buckling. To further demonstrate the complete shape recovery, we unloaded Sample C right after its buckling at the applied strain of $\epsilon = 0.032$ and temperature of 130 K. Our simulation shows that the sample completely recovers its original shape upon unloading (the movie is provided online in the SI of this paper).

Figure 4.9d1,d2 shows the stress-strain curves of all three samples at 130 and 300 K, respectively. These figures show that, at both temperatures, a decrease in the sample thickness (i.e., an increase in AR) leads to a decrease in the overall failure strength, which agrees with our experimental findings: the MG nanolattices with thinner walls (higher aspect ratio) fail at lower stresses. According to elastic buckling theory, reducing the sample thickness (i.e., increasing its AR) leads to a reduction in the critical buckling stress, σ_{cr}, and when $\sigma_{cr} < \sigma_y$, where σ_y is the yield strength of the material, the structural instability plays the dominant role in the failure mechanism through elastic buckling at lower stresses than σ_y. In contrast, in a sample with low aspect ratio where $\sigma_{cr} > \sigma_y$, the material's intrinsic strength would play the dominant role in the failure mechanism.

MD simulation is a powerful tool for understanding atomistic phenomena, but analytical approaches are also useful in capturing critical physical mechanisms. In particular, the brittle-to-ductile transition in 60 nm thick nanolattices cannot be captured quantitatively by MD simulation due to its limited time scales, which lead to unfeasibly fast strain rates that typically reduce rate-dependent processes. Here, we would like to discuss the fundamental reasons for two transitions in deformation mode, brittle-to-ductile and plastic-to-elastic transitions in terms of the size effect on the MG plasticity and the elastic instability of hollow tube, respectively. The size effect on the plasticity of MGs has been discussed in literature, where the transition from heterogeneous to homogeneous deformation is interpreted by the analogy of the Griffith theory of crack growth.[111, 112] By assuming uniaxial straining, the critical dimension for the brittle-to-ductile transition in metallic glasses has been suggested to take the form of

$$t_c = \frac{2^{3/2}\Gamma E}{{\sigma_y}^2 A} \tag{4.1}$$

where t_c is the wall thickness, Γ is the shear band energy, E is the Young's modulus, σ_y the yield strength of bulk metallic glass, and A the aspect ratio of sample. For a $Cu_{60}Zr_{40}$ bulk metallic glass, the Young's modulus (E) is known to be 107 GPa and

the yield strength (σ_y) is 2 GPa.(3) To make the model simple, we assume a fixed aspect ratio with different diameters of A ~ 10 from Jang et al.'s work.(14) The shear band energy can be estimated by equating the increase in the internal energy within the shear band to the work done within the shear band volume:(13, 14)

$$\Gamma = \frac{1}{2}\Delta\epsilon\sigma h_s \tag{4.2}$$

where $\Delta\epsilon$ is the strain within the shear band volume (~order of unity), σ is the applied stress level (2 GPa), and hs is the fixed thickness of the shear band (~10 nm) according to computational studies.[130, 131] Note that elastic strain energy may not be completely converted to shear band energy due to the other possible paths of energy dissipation (e.g., heat). This would lead to a smaller shear band energy and critical thickness. Such dissipative effects are not considered here. However, this simple model still captures the essential physics, as similar models have been used successfully to estimate the critical thickness for various MG nanopillars and nanowires.[111, 112, 115] Using these values, eq 2 gives ~10 J/m2 for the shear band energy at room temperature, which is similar to that from Volkert et al. Using eq 1, the critical wall thickness (t_c) for brittle-to-ductile transition in this work becomes ~76 nm, which is within the range for the emergence of the brittle-to-ductile transition between samples with wall thicknesses of 60 and 120 nm observed in this work. Also, this value is similar to that in Jang et al.'s work on Zr-based MG pillars.(14) eq 1 also indicates that the critical transition dimension t_c has an inverse proportionality with σ_y^2. Because the yield strength of bulk $Cu_{60}Zr_{40}$ metallic glass at 130 K is higher than that of the same glass at room temperatures, we can expect a lower transition length for samples at 130 K. Yoon et al. reported a ~ 25% increase in the yield strength of their Cu-based metallic glass at 130 K.(35) A similar relative increase in the yield strength of the $Cu_{60}Zr_{40}$ metallic glass studied here leads to $\sigma_y \sim 2.5$ GPa at 130 K, and eq 1 results in $t_c \approx 40$ nm, assuming negligible change in Young's modulus and shear band energy. This is only a first-order approximation, and it may be necessary to evaluate the temperature-dependence of shear band energy with a more advanced computational technique. Thus, our simple model suggests that the brittle-to-ductile transition does not occur at 130 K within the thickness between 120 and 60 nm thick MG nanolattices because the critical diameter at 130 K, ~40 nm, is not within this range. This result is consistent with our experimental observation.

Samples with thicknesses of 20 nm deformed elastically only, while those whose

wall thicknesses were 60 nm underwent plastic deformation. This suggests that another transition exists at a critical dimension between these two thicknesses: the PSR-to-FSR transition. Schaedler et al. fabricated nanocrystalline Ni hollow microlattices by ultraviolet laser patterning into photomonomer followed by electroless Ni plating.[121] Their microlattices possess an ultralight weight and exhibit almost complete recoverability even with 50% compressive deformation. Rys et al. made Ni-P MG hollow microlattices and showed that their deformation mode depends on the wall thickness of hollow member.[126] Meza et al. suggested two possible buckling modes, Euler and shell buckling, and it is important to clarify which buckling mode is dominant. The Euler buckling and shell buckling condition are given as the following two equations, respectively.[123]

Euler:

$$\left(\frac{a}{L}\right)_{crit} = \frac{3}{\pi}\sqrt{\frac{2\sigma_{fs}}{5E}} \tag{4.3}$$

Shell:

$$\left(\frac{t}{a}\right)_{crit} = \frac{\sigma_{fs}}{E}\sqrt{3(1-\nu^2)} \tag{4.4}$$

where a is the major radius of ellipse cross section (900 nm), L length of tube (10.6 μm), σ_{fs} the fracture strength (2 GPa), E Young's modulus (107 GPa), t is the layer thickness, and ν is Poisson's ratio (0.3). With the given materials parameters, the Euler bucking condition shows $(a/L)_{crit}$ = 0.083. For our nanolattices, (a/L) = 0.09, which is greater than $(a/L)_{crit}$. Thus, for the ideal structure, the beam will be fractured before the Euler buckling condition is met. This is the same situation with that in Meza et al.'s alumina nanolattices. Also, the shell bucking condition shows $(t/rc)_{crit}$ = 0.031. For our nanolattices with 20, 60, and 120 nm in thickness, (t/r_c) = 0.022, 0.066, and 0.133, respectively. Thus, only the 20 nm thick nanolattices satisfy the shell buckling condition, which ensures purely elastic deformation (buckling) followed by the full shape recovery. Both 60 and 120 nm nanolattices do not satisfy Euler nor shell buckling conditions. This result agrees with our experimental observation that both 60 and 120 nm nanolattices do not exhibit elastic instability.

From the shell buckling mode, it is possible to calculate the critical thickness of shell bucking with the given material and geometric parameters. Then, with these data, eq 4 gives the critical thickness of elastic instability, ~27.8 nm at 298 K. Typically, the elastic constant of metals does not vary much between 130 and 298 K. Thus, it is likely that the elastic constants for the metallic glass studied here remain roughly the same between 298 and 130 K. For a yield strength of 2.5 GPa at 130 K, the

critical thickness for elastic buckling is estimated to be ~34.7 nm at 130 K from eq 4. This value is consistent with the experimental observation, which shows elastic buckling and full recovery of the nanolattice for 20 nm wall thickness that is below the critical thicknesses (42-52 nm) at both 298 and 130 K.

Based on our experiments and MD simulations, the deformation mode is strongly correlated with the wall thickness and temperature. It is useful to construct a deformation mechanism map in the 'thickness-temperature space' by considering the temperature effects on Equations 4.1 and 4.4. Our MD simulations demonstrate a linear relation between the absolute temperature and yield strength for our Cu-Zr system. Thus, if we assume $\sigma_y = \alpha T + \beta$ (GPa), we can get $\sigma_y = -(2.98 \times 10^{-3})T + 2.89$ GPa by using our experimentally measured strengths, 2 GPa at 298 K and σ_y = 2.5 GPa at 130 K. Incorporating this temperature relation into Eqs 4.1 and 4.2, the deformation mechanism map can be constructed as seen in Figure 4.10. In this mechanism mapping, the three explored wall thicknesses of 120, 60, and 20 nm at 298 K correspond to brittle, ductile, and FSR deformation modes, respectively. This means that at room temperature, the brittle-to-ductile transition occurs at some thickness between 120 and 60 nm, and the PSR-to-FSR transition occurs at another critical thickness between 60 and 20 nm. At 130 K, both explored wall thicknesses of 120 and 60 nm are located inside of the brittle region, so the deformation mode shifts directly from brittle to FSR deformation, without another transition in between. Therefore, our simple model captures the experimentally observed temperature-dependence of deformation mode, and implies that both the structural and size effects are key physical attributes on the deformation behavior of nanolattice structure.

In conclusion, we fabricated hollow-tube cubic-shaped octet $Cu_{60}Zr_{40}$ metallic glass nanolattices with overall dimensions of 65 μm × 65 μm × 65 μm and studied their mechanical behavior for the three different hollow tube-wall thicknesses of 20, 60, and 120 nm. They exhibit unique transitions in deformation mode with tube-wall thickness and temperature. The brittle-to-ductile transition at room temperature likely stems from the intrinsic material size effect of ductility in nanometer-sized metallic glasses, but this transition does not occur at 130 K since slower thermal processes diminish the effect of the free surface on promoting diffuse shear deformation.[114] For the thinnest (20 nm) wall thickness, elastic shell buckling occurs regardless of temperature because the shell buckling model estimates that 20 nm is much smaller than the critical thickness of transition at both 298 and 130 K. MD simulations

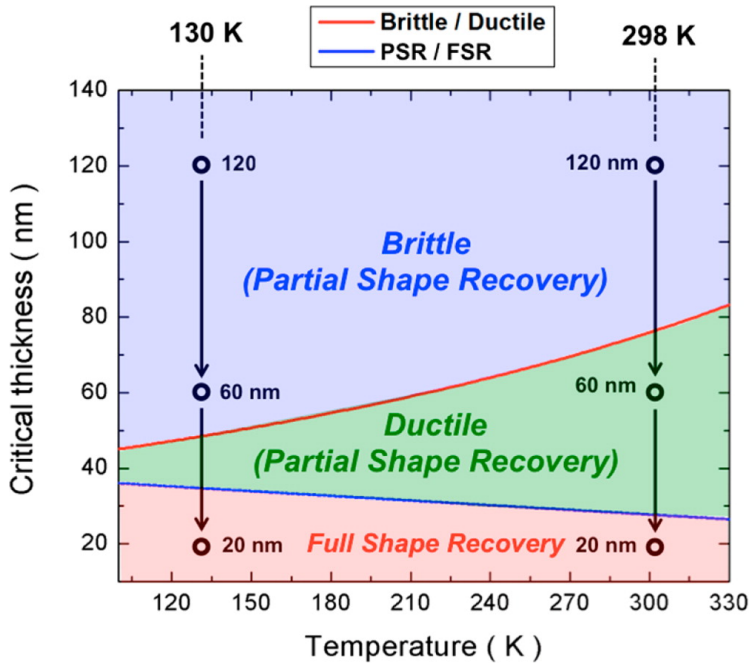

Figure 4.10: Brittle (PSR)-ductile (PSR)-FSR (full shape recovery) deformation map in the temperature-thickness space. The red line indicates the critical thickness between brittle and ductile deformation, and the blue line indicates the critical thickness between plastic and elastic deformation.

also demonstrated that the deformation mode depends on both material dimension and temperature as observed in our experiment. Large aspect ratios induce elastic buckling and shear localization is enhanced at lower temperatures. A map of deformation modes was constructed in the thickness-temperature space by considering the temperature-dependence of critical thickness for both the brittle-to-plastic and the PSR-to-FSR transitions. This map implies that structure, size, and temperature are key physical attributes on the deformation behavior of MG nanolattices, which are critical considerations for the future design of meta-materials.

FROM PROPERTY-TO-STRUCTURE, TO STRUCTURE-TO-PROPERTY

Here we make a shift in our approach to understanding these metallic glasses. In the next couple of chapters, we attempt to characterize the atomic-level structure using Molecular Dynamics simulations and a combination of *in-situ* X-ray tomography and diffraction. With this approach, we propose a model system for understanding the disordered structure, the percolation cluster, a simple disordered system that has many similar characteristics and properties to metallic glasses. We find that the packing efficiency and topology of its atoms are critical for understanding the structural state of a glass. This information, when properly characterized and placed in the proper context, will allow us to take a structure-to-property approach to understanding disordered materials. Eventually we may become as comfortable with disordered materials as we are with ordered ones.

Chapter 5

DIMENSIONALITY OF THE ATOMIC-LEVEL STRUCTURE

Freeze a liquid fast enough, and you get a glass, a material that is structurally similar to the liquid, but incapable of flow. This concept, albeit not well understood,[132, 133] is so ubiquitous that it holds even for metals (3). Unlike most crystalline metals and alloys, metallic glasses earn their name from a lack of long-range atomic order and the absence of typical defects, like dislocations, rendering their microstructure challenging to conceptualize and model. Some studies suggest the existence of short-range order, where solute-centered clusters serve as the building blocks, and medium-range order is characterized by cluster packing.[134–136] While instructive, these short- and medium-range packing schemes inevitably break down over longer coordinates due to spatial incompatibility and do not fully describe the atomic organization within these complex glasses. The incomplete understanding of atomic level structure in glassy materials has made it challenging to capture the physics of their unique response to mechanical deformation. We propose a model that describes a short-range order and encompasses the long-range structural details of metallic glass. The model has considerable implications for understanding glass properties and the origin of the glass transition.[1]

Diffraction experiments characterize the structure of amorphous materials by mapping the atomic neighbor separation distances and statistical density distributions. Dissimilar glasses and liquids commonly possess distinct short- and medium-range order due to variations in chemical bonding, but the atomic structure becomes fluid-like and nearly indistinguishable among different glasses beyond the first few nearest neighbors.[137] The similarity of atomic-level environments in liquids and glasses makes it difficult to understand how glasses get their rigidity. Glass rigidity may be related to the jamming of atoms as density increases.[138] The marked difference between the short-range and long-range configurations in glassy systems sets glasses apart from crystals. Unlike for crystals, simplifying the underlying structure in a glass is problematic because the short- and medium-range order cannot repeat a recognizable pattern. For this reason, no two glasses, produced under the same conditions and with similar diffraction patterns, are identical at the atomic level.

[1]Parts of this chapter are published online at DOI: 10.1126/science.aab1233

The question of how repeatable long-range structures in glasses can emerge from non-repeating atomic clusters remains unanswered.

5.1 Fractal scaling in metallic glasses

Studies suggest fractal properties exist in metallic glasses.[139, 140] Fractal behavior manifests in the relationship between mass and volume. For crystals, this relationship $M(r) \sim r^3$ has a dimensionality (d) of 3. The dimensionality of metallic glasses is closer to ~2.5,[140] and any non-integer d can correspond to a fractal[141]. Many naturally-occurring random fractals have $d \sim 2.5$, including crumbled balls of paper and thin sheets,[142] which are fractals even down to the size of nanoballs of graphene oxide[143]. Fractal concepts may be useful in developing an atomic-level understanding of amorphous materials because they imply underlying order in inherently chaotic and random arrangements. The specific nature of fractals in MGs is not obvious because most mass fractals have macroscopic pores at large r, e.g. crumpled paper, and metallic glasses are monolithic materials. Metallic glasses have packing fractions close to or exceeding that of close-packed crystalline metals.[144] The puzzle of how metallic glasses can simultaneously possess fractal properties and remain fully dense is unresolved.[145] One possible explanation is that the diffraction experiments only probe the short-range dimensionality. We observe a fractal short-range $d < 3$ and a homogenous long-range $d = 3$ for several metallic glasses, showing the presence of a dimensionality crossover at an intermediate length scale.

Previous studies have focused on the principal (first) diffraction peak only, q_1.[139, 140] We extend the analysis beyond the first peak because the information contained in diffraction experiments is spread out in momentum space, and each peak contains information that represents a part of the total structure. We conducted in-situ high pressure x-ray diffraction and full-field nanoscale transmission x-ray microscopy experiments on $\sim$ 40μm-diameter cylindrical samples of $Cu_{46}Zr_{46}Al_5Be_3$ metallic glass (Fig. 5.1A). We made diffraction and sample volume measurements in-situ as a function of hydrostatic pressure in the diamond anvil cell. We relate scattering vector from diffraction peak positions to volume by increasing hydrostatic pressure from $\sim 0 - 20$ GPa (Fig. 5.1B). Using multiple data points improves accuracy for measuring the exponent compared to previous methods.[139] Structural information is sensitive to the magnitude of the scattering vector. We found $d \sim 2.51$ for q_1 to be consistent with previous experiments on other metallic glasses.[139, 140] The value ~2.64 from q_2 measurements was 5% higher than that from q_1 (Fig. 5.1C). To explore the repeatability of this finding, we analyzed data obtained from

a $La_{62}Al_{14}Cu_{11.7}Ag_{2.3}Ni_5Co_5$.[140] First peak data for both systems shows the same exponent of ~2.5 while the q_2 data for the $La_{62}Al_{14}Cu_{11.7}Ag_{2.3}Ni_5Co_5$ shows an exponent of nearly 3 (Fig. 5.1C). This shift is greater than the one in the $Cu_{46}Zr_{46}Al_5Be_3$, and it supports the observation that a change in the dimensionality arises from probing different extents within the atomic structure in momentum space. Extracting structural information from momentum space measurements is difficult because the information is spread out. Real space radial distribution functions (RDF) are needed, where peak positions correspond directly to atomic separations. Background noise and limited range of q restrict the accuracy of Fourier transforms applied to experimental RDFs. Simulations allow for this type of investigation.

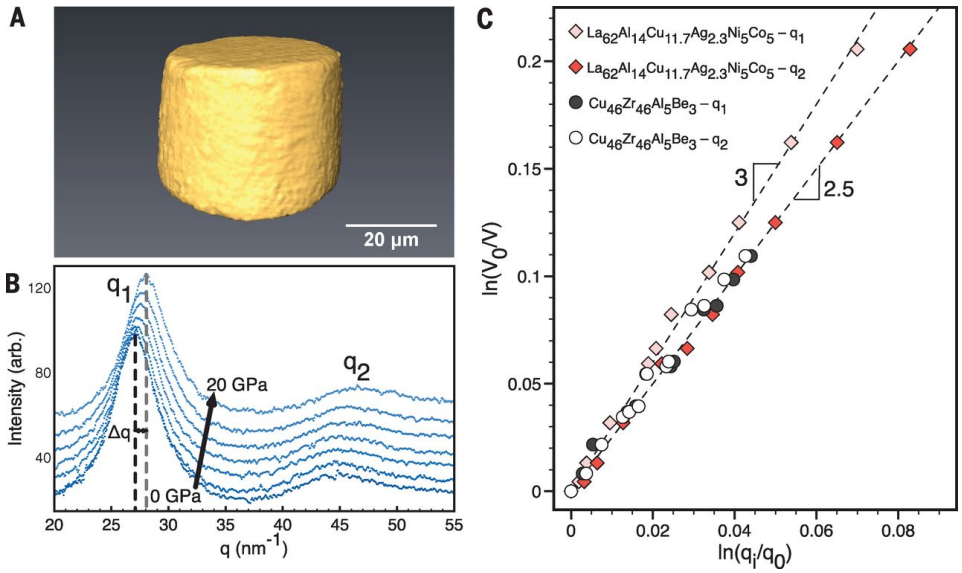

Figure 5.1: *In-situ* diffraction and volume results. (A) Three-dimensional reconstructed sample volumes from in situ transmission x-ray microscopy data at ~0 GPa. (B) In situ x-ray diffraction data with increasing pressure (arb., arbitrary units). (C) Volume scaling with scattering vectors q_1 and q_2 for $Cu_{46}Zr_{46}Al_5Be_3$ and $La_{62}Al_{14}Cu_{11.7}Ag_{2.3}Ni_5Co_5$ metallic glasses.

5.2 Real space estimates of local dimension

Molecular dynamics (MD) simulations can replicate glass structure, but the simulation timescales (ps), are many orders of magnitude shorter than in the experiments. We ensured the system had proper time to relax at each pressure increment to address this issue. We held the loading rate constant at 50 GPa/ns ($5 \times 10^19 Pa/s$), and we allowed the system to relax for ~ 0.1 ns to reach thermodynamic equilibrium at each pressure interval. Higher quench rates in simulations may produce less-relaxed glasses, although their structures often agree well with experiments.[146–148] The

differences in compression rates result in quantitative discrepancies, but the qualitative and phenomenological aspects of the simulations should represent a realistic physical system. We generated $Cu_{46}Zr_{54}$ RDFs using two embedded atom method force fields: Cheng, et al. (FF_1)[147] and Mendelev, et al. (FF_2)[148]. The neighbor separation-volume relationship for Rd peaks $r_1 and r_2$ showed $d \sim 2.54$, similar to the experimental result, but transitions to ~ 3 between $r_2 and r_3$ (Fig. 5.2A). We also simulated $Ni_{80}Al_{20}$, which shows a similar crossover between $r_1 and r_2$ (Fig. 5.2B).[149]

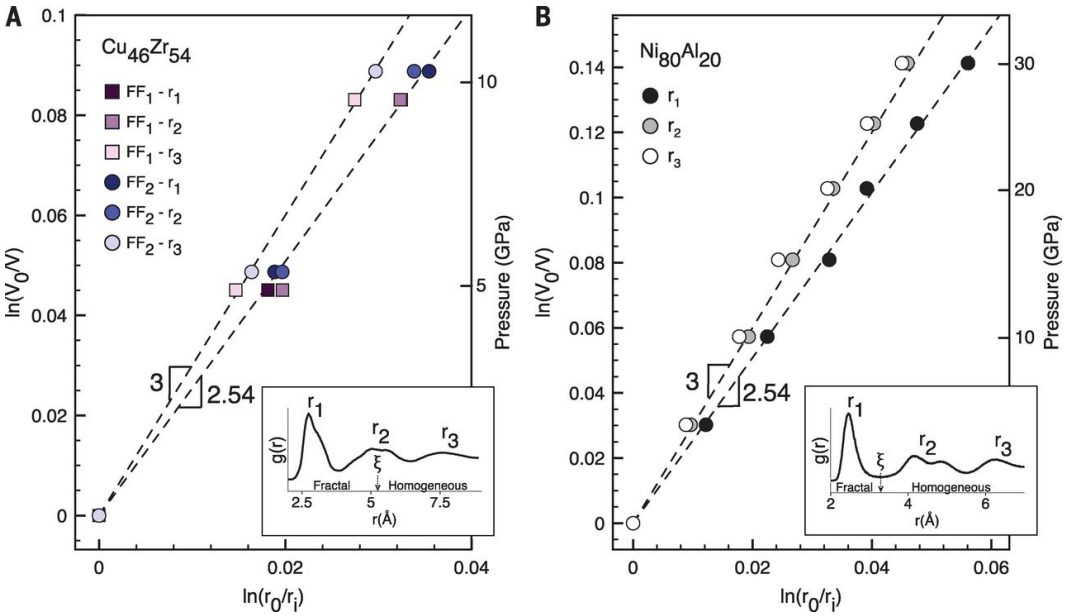

Figure 5.2: Dimensionality crossover in simulations. (A) The Cu_46Zr_54 from FF_1 and FF_2 both exhibit a transition in dimensionality from ~2.5 to 3 between r_2 and r_3. (B) $Cu_{46}Zr_{54}$ exhibits a transition in dimensionality from ~2.5 to 3 between r_1 and r_2. The insets show corresponding Rd curves with the correlation lengths ξ indicated.

5.3 Percolation models to describe dimensional crossover

The percolation cluster[150] is likely the most relevant fractal model to describe the structure of metallic glasses. The cluster represents a disordered system with fractal dimension $d \sim 2.52$ and appears across many physical systems[151, 152]. Percolation models incorporate the probability of occupied (p) and empty ($1 - p$) sites. At low p values the system is not fully connected, e.g. an electrical insulator (Fig. 5.3A). The percolation threshold (p_c) is when a percolating network forms, allowing incipient conduction. Large p systems have many conduction paths (Fig. 5.3B). What sets the percolation model apart is the existence of a correlation length,

ξ, which characterizes the size of the finite clusters at concentrations below and above p_c. The correlation length is defined as the average distance that spans two sites within the same cluster and has units equal to the size of the smallest constituent unit in the model. At $p < p_c$ and $p > p_c$, ξ is finite and the system is only fractal at length scales shorter than the correlation length. On length scales longer than ξ, the structure is homogeneous. This property of percolation clusters may help reconcile the notion that fractals need not exhibit self-similarity across all length scales (Fig. 5.3C).[152]

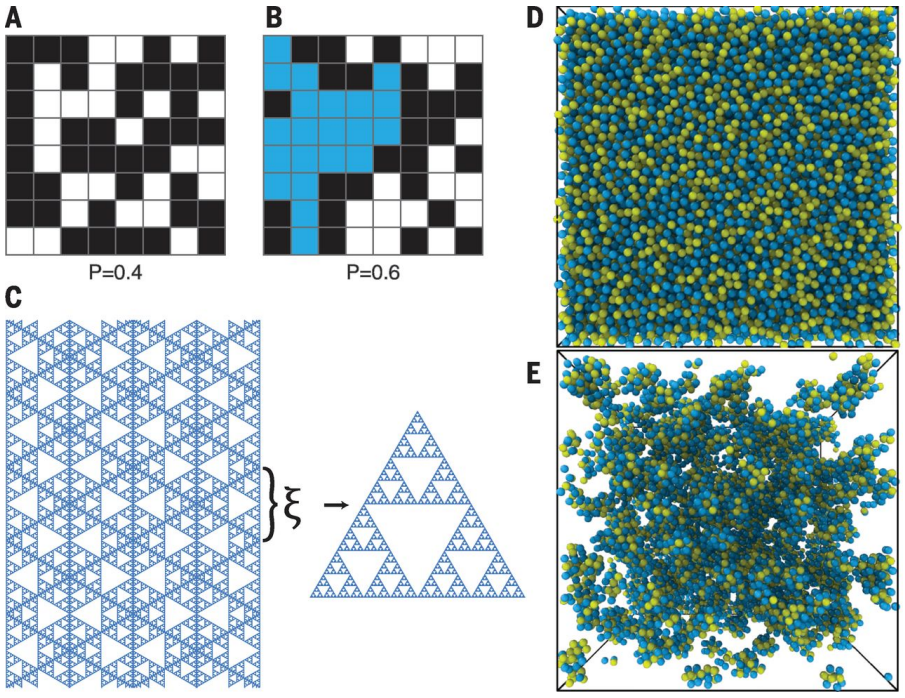

Figure 5.3: Concepts in fractals and percolation. (A and B) Site lattice percolation for $p < p_c$ (A) and $p > p_c$ (B). White squares are "occupied," black squares are "unoccupied," and blue squares are percolating. (C) Illustrative example of a lattice made up of Sierpinski gaskets with correlation length ξ, adopted from [152]. This lattice is fractal over the short range and homogeneous over the long range. (D) MD simulation of the $Cu_{46}Zr_{54}$ system at room temperature with full periodic boundaries (Cu, blue; Zr, yellow). (E) $Cu_{46}Zr_{54}$ with all atoms removed, except for those belonging to icosahedrons.

We use a continuum percolation model where p is analogous to the atomic packing fraction (ϕ) and the percolation threshold is analogous to a critical volume fraction $\phi_c = \phi p_c$.[152, 153] The correlation length is:

$$\xi \propto |\phi - \phi_c|^{-\nu} \tag{5.1}$$

for continuum percolation, where $\nu = 0.8764$.[154]

We estimated ϕ_{CuZr} to be $0.717 - 0.728$, in good agreement with previously reported value[144] using the chemical composition and the atomic radii of the simulated glass.[155] A reasonable model for the packing of a binary metallic glass involves continuum packing of hard spheres, with a p_c of ~ 0.310.[156] We obtain a $\phi_c \approx 0.257$ by averaging the hard sphere value ($\phi_c \sim 0.224 = p_c\phi_{CuZr}$) with an overlapping sphere value ($\phi_c \sim 0.2896$),[157] as atoms in metallic glass are not ideally rigid[158]. The correlation length is nearly equal to 2 for $Cu_{46}Zr_{54}$, $\xi_{CuZr} \sim 1.93 - 1.98$, suggesting the information in the first and second peaks pertains mostly to the Angstrom-sized fractal clusters, while information in the third peak pertains to the homogeneous bulk. This result is consistent with our observations of a crossover in dimensionality between r_2 and r_3 (Fig. 5.2A), and provides evidence for the presence of percolation structure in metallic glasses. The short-range considerations for high local densities favor the formation of Cu-centered clusters, giving rise to a large number of Cu-centered icosahedra in lieu of the close-packed structures in native Cu and Zr (Fig. 5.3D).[145] The atoms with local icosahedral order form a percolating network (Fig. 5.3E).

Equation 5.1 suggests that higher packing fractions bring about shorter correlation lengths. We estimate that the $Cu_{46}Zr_{54}$ has a high packing fraction ϕ_{NiAl} of ~ 0.793, although this could be an overestimation due to the covalent nature of the Al bonding. This gives $\xi_{NiAl} \sim 1.73$, which is much less than 2. Not surprisingly, the result shows a crossover in dimensionality from ~2.54 to ~3 that occurs between r_1 and r_2 (Fig. 5.2B). We can also induce a shift in the crossover for Cu_6Zr_54 from between r_2 and r_3 to between r_1 and r_2 at P > 15 GPa by increasing the packing fraction and bringing ξ_{CuZr} below ~ 1.7.[155] Some of the atoms in amorphous materials undergo local non-affine displacements even in response to purely hydrostatic loads. The fraction of such non-affine atoms is low, $\sim 21.7\%$, and they do not appear to have any effect on the scaling behavior and crossover.[155]

We relate the current model to the glass transition by examining the dimensionality as a function of temperature. We do not observe fractal behavior of $Cu_{46}Zr_{54}$ until 400 K, well below the glass transition temperature of 763 K (Fig. 5.4A). The dimensionality gradually decreases from ~ 3 to ~ 2.54 over this temperature range as the temperature decreases. This behavior suggests an intermediary process like jamming,[138, 159, 160] where the percolating cluster begins to jam at the glass transition. Complete jamming occurs at lower temperatures along with the

emergence of fractal properties, correlating with a loss of ergodicity and consistent with the characteristic kink in the volume-temperature curve during supercooling (Fig. 5.4B). Despite structural similarities, liquids are open to rearrangement in local atomic configurations while in rigid solids these configurations are preserved. Pressure elicits a mostly non-affine response from the liquid and a comparatively affine response from the glass. Applied hydrostatic forces inevitably alter the structure and induce structural relaxation in a liquid, which is unavailable in a glass. This difference is likely the reason for the emergence of fractal properties below T_g in a glass, and lack thereof above T_g in a liquid. Metallic liquids possess packing fractions in excess of our estimated percolation threshold, which implies that their atomic structure is also a percolating cluster that has not yet frozen or jammed.

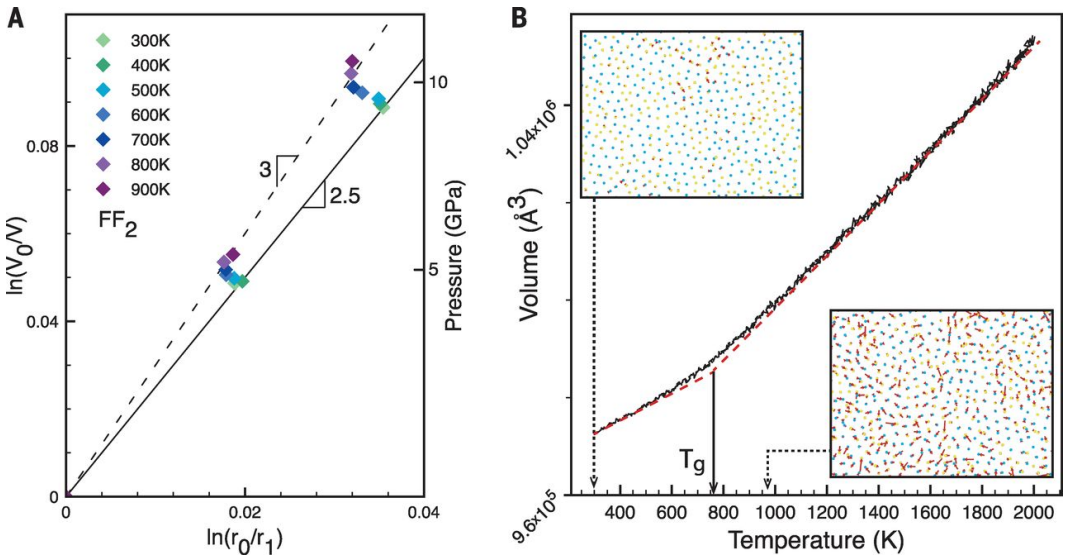

Figure 5.4: Simulated properties during supercooling. (A) Dimensionality from r_1 during supercooling. (B) Volume versus temperature behavior (solid black line), shown with guidelines (red dotted line) and T_g (~763 K, solid black arrow). Inset snapshots show atom vectors (red) generated from reference temperatures ~540 K above the indicated temperatures (dotted black arrows) for a slice 3 Åthick (roughly the nearest-neighbor distance). Dots are atom centers (Cu, blue; Zr, yellow).

5.4 Discussion of implications

A fractal model might be useful in explaining the dynamics of metallic glasses, as concepts from percolation have been applied successfully to other glass formers.[161] The dynamic heterogeneities that emerge in supercool liquids may be related to the spatial distribution of nonpercolating clusters. Estimating the average number of particles in these clusters using $\sim N_{avg} \approx \xi^3$, where $\xi \sim 2$, we get

a value, $\sim$ 8, that is close to experimentally observed values in colloidal glasses, $\sim 3-7$.[162] From the perspective of packing, percolation, and jamming, a correlation between density and T_g[163] is intuitive. If metallic glasses are created from the jamming of a percolating cluster, then glass formation is simplified: one only needs to reach the jamming packing fraction, ϕ_j, before nucleation occurs. This could be accomplished by a combination of hydrostatic pressure and fast cooling rates. The strong correlation of metallic glass yield strength with T_g implies that collective atomic motions dictate both yielding and glass formation[164]. Because denser metallic glasses tend to be better glass formers with higher T_g,[163] the strength enhancement seen in glasses with higher T_g may derive from the size of the clusters, which increases with packing fraction. Higher packing leads to larger jammed clusters, which present more substantial barriers to the initiation of collective atomic motions that lead to catastrophic shear banding. The movement of these finite, nonpercolating clusters may also be related to shear transformation zones, which are collective rearrangements of atoms during deformation of metallic glasses.[165] This is supported by the observation that typical zone sizes, $\sim 10-20$ atoms[166–168], are consistent with cluster sizes, $\sim$ 8 atoms. The continuum percolation model illustrates how structure and rigidity may organize in the absence of ordering; atoms percolate in the liquid, and the percolating cluster 'freezes' (or jams) into a glass.

Chapter 6

COMPARISON OF STRUCTURAL DIMENSIONALITY IN LIQUIDS AND GLASSES

The viscosities and relaxation times of glasses and liquids across the glass transition temperature (T_g) are separated by many orders of magnitude.[169] This large increase in viscosity over a short temperature range is not accompanied by significant changes in the long-range atomic structure, which remains amorphous. Metallic glasses are locally more ordered in the short- and medium-range than their liquid counterparts,[170, 171] but this ordering plays an ambiguous role in the glass transition[172]. A structural model that captures both liquids and glasses is useful for understanding the amorphous structure and the subtle changes, if any, that occur across T_g and their potential connection to the glass transition phenomenon.[1]

One way to characterize the structure is by measuring the local dimension, d, which describes how, on average, the mass of atoms within a spherical section of material with radius r scales, $M(r) \propto r^d$.[173] In relating the positions of the first sharp X-ray diffraction peaks (q_1) to sample volume (V), several groups have reported a scaling relationship in metallic glasses, with exponent, d~2.31-2.5, which deviates from the $d = 3$ expected under the assumption that $q_1 \propto 1/a$, where a is the interatomic spacing.[174–176] Recent experiments on electrostatically levitated metallic liquids also show a non-cubic power law exponent of d~2.28.[177] These power law exponents are related to the local dimension of the atomic structure, and the observations of an exponent/dimension less than 3 have led to suggestions of an underlying fractal structure in metallic glasses.[174, 176] The long-range scaling relationship in metallic glass structure is not fractal over all length scales because no macroscopic pores or voids are present in their microstructure, and such pores are a defining characteristic of fractals that maintain their scaling relationships over all length scales (e.g. the Sierpinski triangle).

To help resolve these issues Chen et al. proposed that metallic glasses at the atomic-level can be described using percolation,[176] a model that captures the interconnectivity of sites on a lattice or spheres in a continuum (See previous chapter).[173]

[1] Some of this chapter contains material that is on arXiv:1601.02057 as well as material that is under review. Some or all of the material may be change/edited for publication. The data should be considered preliminary.

Three-dimensional percolation models, such as hard sphere and overlapping sphere continuum models, exhibit a fractal dimension of d~2.52 at lengths below a correlation length, ξ, and a crossover to a dimension d~3 above ξ, where ξ is roughly the diameter/length of finite, non-percolating clusters.[173] These crossovers have a morphology that is similar to what is shown in Figure 6.1a. Using molecular dynamics (MD) simulations, Chen et al. found that two distinct metallic glasses have short-range dimensions of d~2.5 below ξ ~2 atomic diameters and a dimension of 3 occurs over longer lengths. This suggested that metallic glasses are structurally similar to a continuum percolation (i.e. random coalescence) of spherical particles.[176] This crossover at ξ may explain the anomalous non-cubic scaling exponents in q_1 vs. V observed experimentally in macroscopically homogeneous and fully dense metallic glasses and liquids.[174–177] Such a connection between percolation structure and glasses has also been suggested by Orbach, who applied percolation theory to describe high frequency (short length) vibrational states in glassy systems and also suggested that amorphous materials may exhibit fractal properties at short length scales.[178]

The question remains whether liquids exhibit a crossover in dimension from $d < 3$ to $d = 3$. Percolation structure has been studied in hard spheres,[179, 180] overlapping spheres,[181, 182] and recently metallic glasses,[176] suggesting a likely connection to metallic liquids, which share structural similarities with both metallic glasses and hard sphere systems[183]. One previous method to measure dimension utilized hydrostatic pressures to induce peak shifts in radial distribution functions (RDF) that were compared to corresponding volume changes.[176] However, this hydrostatic pressure-induced Rd peak shift method has some downsides: it is not well suited for studying liquids, in which atoms rearrange and exchange neighbors readily under pressure; The correlation lengths, ξ, can only be inferred based on the scaling of various peaks; Moreover, the broadness of the Rd peaks leads to results that are sensitive to the specific method of generating and measuring the RDF.[184] To overcome these issues, we chose here to integrate the RDFs to obtain cumulative coordination numbers (CN). This integral method calculates the local dimension of the structure without the need for applying hydrostatic pressures or measuring small shifts in broad amorphous peak positions, which are methods that we used previously8. With this CN analysis, we observe a crossover in dimension from $d = 2.55 \pm 0.06$ in metallic liquids and $d = 2.71 \pm 0.04$ in metallic glasses, to $d = 3$ for the second coordination shell and beyond, suggesting that ξ ~3 atomic diameters.

6.1 Dimension and crossover

One measure of dimension comes from the scaling of extensive properties with size such as mass, i.e. $M(r) \propto r^d$, where M(r) is the mass contained in a sphere of radius r. M(r) is calculated as an average over the entire system by choosing different atoms as the center of the sphere.[173] In our analysis, we used the value CN+1 to represent the average number of atoms within a sphere of radius r (1 added to account for the center atom), an extensive property that is proportional to average mass. The scaling relationship for a percolation structure above the percolation threshold, ϕ_c, exhibits a crossover in dimension from d~2.52 to d~3 at ξ, where $\xi \propto (\phi - \phi_c)^{-\nu}$.5 The parameter definitions are: ϕ is the packing fraction, ν = 0.8764 is the critical exponent for the correlation length,[185] and ϕ_c is the percolation threshold in 3-dimensional continuum percolation.[173] The expected crossover point for several of the metallic systems studied here has been estimated to be ξ~2.8 This value represents the average size of clusters in units of atomic diameters, and suggests that the crossover occurs after the first atomic coordination shell. To avoid inaccuracies that may arise from determining precise peak shifts in broad amorphous peaks, we obtain the dimension of each atomic structure by measuring the slope of ln(CN+1) versus ln(r) for $Cu_{46}Zr_{54}$, $Ni_{80}Al_{20}$, $Ni_{33.3}Zr_{66.7}$, and $Pd_{82}Si_{18}$ metallic liquids and glasses. We find that a crossover from $d < 3$ to $d = 3$ occurs in all cases beyond the first to second coordination shell. We compare these results to those for pure Cu in liquid, glass, and crystalline phases.

Metallic glasses

We measure d by performing a linear fit between the radius of the center atom, r_{avg}, and the outer radius of the first coordination shell, r_{1s}. The r_{avg} is defined as the average radii of the atoms in the binary systems (i.e. for $Cu_{46}Zr_{54}$, $r_{avg} = 0.46r_{Cu} + 0.54r_{Zr}$). There is on average one atom (i.e. the center atom) within this radius, making it an appropriate first point in the analysis of the dimension. Using this approach, we establish the following estimates of dimensions: $d = 2.68$ for $Ni_{80}Al_{20}$, $d = 2.73$ for $Ni_{33.3}Zr_{66.7}$, $d = 2.66$ for $Pd_{82}Si_{18}$, and $d = 2.74$ or 2.73 for $Cu_{46}Zr_{54}$ using FF_1[186] or FF_2[187], respectively (Figure 6.2), all at 300 K. The average dimension for metallic glasses of $d = 2.71 \pm 0.04$ is ~0.19 higher than what would be expected from percolation theory, where d~2.52,5 and is higher than previous measurements of ~2.3-2.56, 7 (diffraction experiments) and ~2.58 (molecular dynamics with hydrostatic pressure). In the region between the center atom and first coordination shell, r_{avg}-r_{1s}, CN rises sharply due to the discrete

nature of the atom counting procedure. A continuous measure of the CN that allows for fractions of atoms to be counted might give a smooth, filled-in curve between the center atom and first coordination shell and a more accurate estimate of short-range dimension (see Section C). Between the outer radii of the first and second coordination shells, r_{1s}-r_{2s}, the dimension crosses over to 3 for all cases, suggesting that these metallic glasses have a correlation length of around $\xi \sim 3$ atom diameters, which is one diameter higher than previous estimates.[176] Within the first to second coordination shell, free volume arising from packing inefficiencies contributes to a reduced dimensionality in the structure. This reduced/fractal dimension cannot proliferate to greater lengths because the free volume necessarily remains smaller than the volume occupied by atoms, whose relative positions are dictated by long-range attraction and low kinetic energy. At longer length scales, where free volume is less significant and the atom clusters appear closely packed, we find that the dimension of the structure is 3.

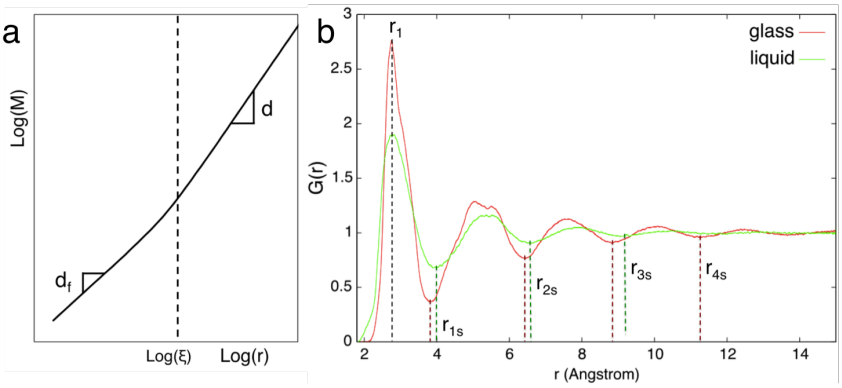

Figure 6.1: a) Diagram of expected crossover in log-log plot of mass versus radius. Short-range fractal dimension d crosses over to long-range dimension d at the correlation length ξ. b) Radial distribution functions for $Cu_{46}Zr_{54}$ (FF_2) in the glass and liquid phase. Dashed lines indicate positions for the first peak, r_1, and coordination shells, r_{is}.

Metallic liquids

Applying the same method to metallic liquids, we measure d = 2.57 for $Cu_{46}Zr_{54}$ FF_1 at 2500 K, d = 2.55 for FF_2 at 2000 K, d = 2.48 for $Ni_{80}Al_{20}$ at 3000 K, d = 2.64 for $Ni_{33.3}Zr_{66.7}$ at 2500 K, and d = 2.53 for $Pd_{82}Si_{18}$ at 2000 K (Figure 6.3). These estimates are weakly dependent on temperature, as the position of r_{1s} changes due to thermal expansion. The average value of $d = 2.55 \pm 0.06$ is in line with the expected value of ~2.52 from percolation theory,[173] and is roughly ~0.1 lower than the average value in our metallic glasses. This order may be related

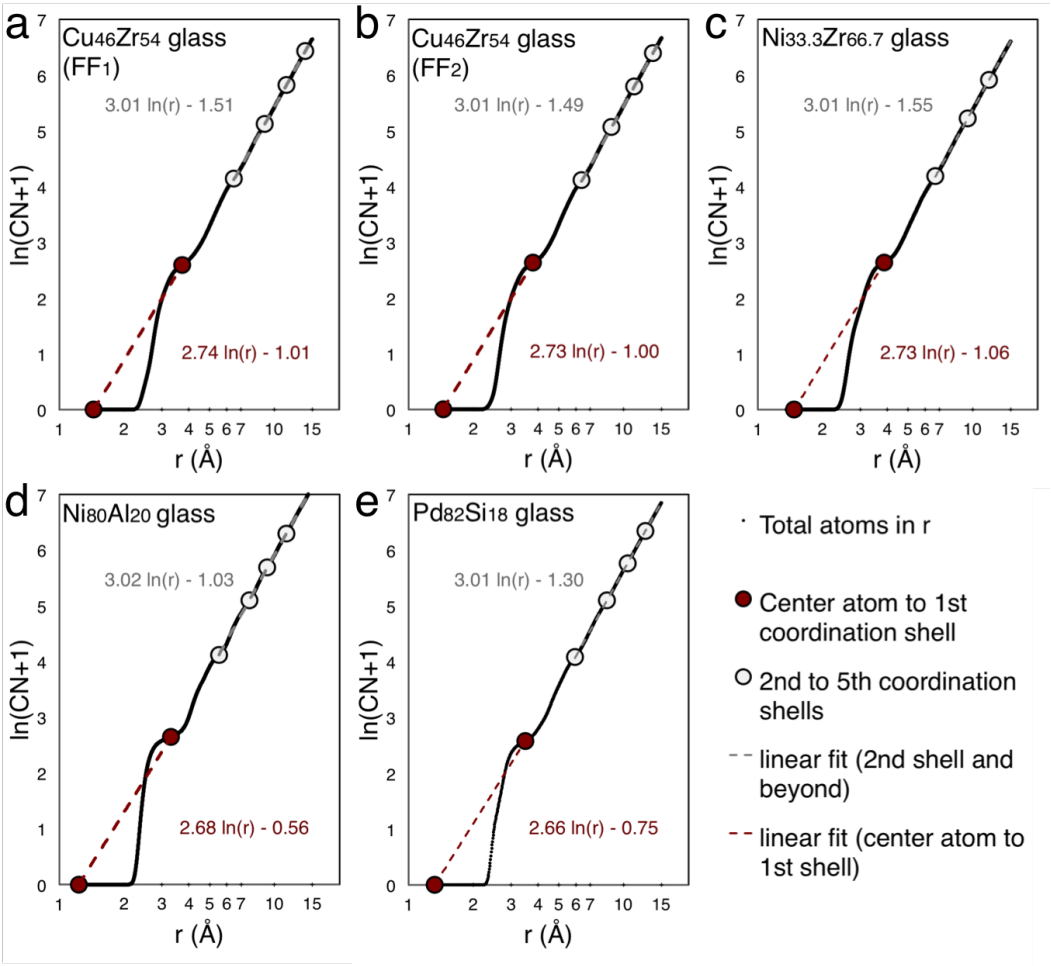

Figure 6.2: Log-log plots of total atom number (CN+1) versus radius, r, showing local dimension in metallic glasses of $Cu_{46}Zr_{54}$ a) FF_1, b) FF_2, c) $Ni_{80}Al_{20}$, d) $Ni_{33.3}Zr_{66.7}$, and e) $Pd_{82}Si_{18}$. Short-range dimension, $d = 2.71 \pm 0.04$, is measured through a linear fit between the radius of the center atom and the outer radius of the first coordination shell. Long-range dimension $d = 3$ is measured from a linear fit of points beyond the outer radius of the second coordination shell.

to the formation of dense clusters, such as icosahedra, which reduce local free volume.[171, 188, 189] A crossover in dimension from $d < 3$ to $d = 3$ occurs in the same region as in the metallic glasses, which indicates that the liquids may also have percolation structures with a correlation length around $\xi \sim 2$ atomic diameters, in agreement with previous suggestions.8 The correlation length is inversely related to the atomic packing fraction, and more loosely packed liquid structures may exhibit longer crossover lengths. Metallic liquids are dense, possessing packing fractions of around $\phi \sim 0.67$ (FF_2 at 2000 K), a value that is only ~8% lower than their glassy counterparts ($\phi \sim 0.73$ for FF_2 glass at 300 K). To observe structures with $\xi \sim 3$

diameters or longer, we estimate that we would need to study liquids and glasses with packing fractions in the neighborhood of ϕ~0.5, which is not feasible for our metallic systems, as a first-order phase transition to the gaseous phase would likely precede such a low packing fraction in the liquid phase.

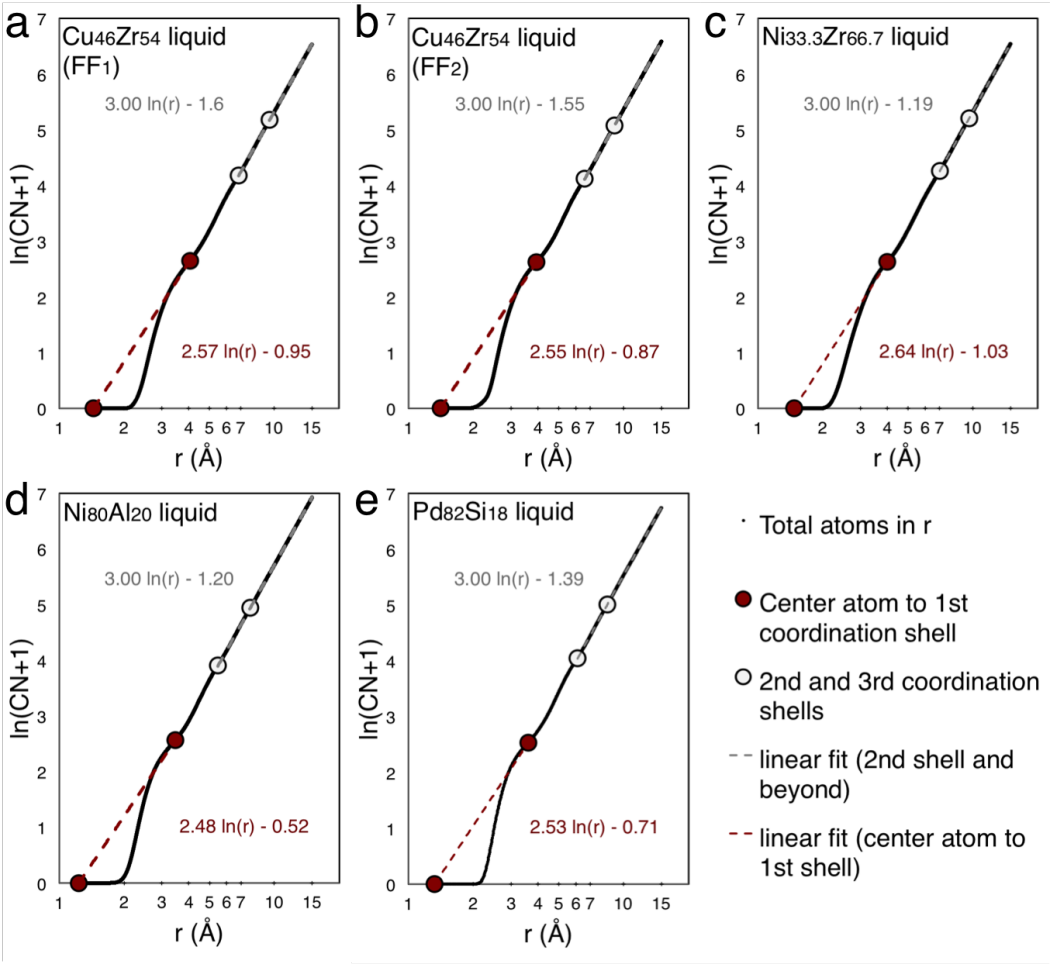

Figure 6.3: Log-log plots of total atom number (CN+1) versus radius, r, showing dimensions *d* for metallic liquids of $Cu_{46}Zr_{54}$ a) FF_1 at 2500 K, b) FF_2 at 2000 K, c) $Ni_{80}Al_{20}$ at 3000 K, d) $Ni_{33.3}Zr_{66.7}$ at 2500 K, and e) $Pd_{82}Si_{18}$ at 2000 K. Fractal dimension *d* is measured through linear fit between the radius of the center atom and the outer radius of the first coordination shell. Long-range dimension *d* is measured from a linear fit of points beyond the outer radius of the second coordination shell.

6.2 Comparison to Copper and grid analysis

We compare our results to those for crystalline Cu at 300 K, which has a dimension of 2.93 between the center atom and the minimum after the first peak (measured at the midpoint between the first and second peak). Beyond the first peak, the dimension

is ∼3 (Figure 6.4). We expect the crystal dimension to be exactly 3 owing to its close-packed cubic structure; our observed deviation suggests that our short-range measurement of the dimension is not precise, yielding a value of 2.93. This error may stem from the discrete nature of the atom counting process.

Comparison of the crystalline, glassy, and liquid phases of Cu shows that the major contribution to fractal dimensionality in the liquid and glassy phases is the short-range structure, which is locally more open. The overall coordination number curve is shifted toward higher radii for the liquid phase, which reduces the short-range dimension. The short-range structure in the glass phase appears denser and more ordered compared to the liquid - the coordination number rises more steeply in the first shell, increasing d towards a close-packed, crystalline value.

The discrete nature of our atom-counting procedure introduces error into the estimates for local dimension and makes the observation of reduced short-range dimension in these glassy and liquid structures delicate, as the fitting is performed over only two points. These issues motivate a method to count the atoms continuously by modeling them as spheres that occupy a volume based on their atomic radii. For this purpose, we introduced a grid to our Cu system with 0.3 Åspacing. This grid occupies the volume of each atom with grid points of 0.3 Åresolution. To perform the atom counting, we take the partial RDFs of each atom with respect to the grids and normalize the sum by the number of grids per atom.

6.3 Discussion and summary

We find that the cumulative CN analysis shows a crossover in dimension for both metallic glasses and liquids. We observe that the short-range dimension is less than 3, d ∼2.55-2.76 for both liquids and glasses. The long-range dimension crosses over to d = 3 beyond the second coordination shell, which suggests that the underlying structure in these metallic liquids and glasses may be related to percolation, a model that exhibits similar values of short-range fractal dimension, d ∼2.52, and also has a crossover.

The glass transition may be related to the densification/ordering that occurs in the local glass structure, but the connection is not clear. Previous analyses comparing amorphous and crystalline structures have emphasized that radii ratios of ∼0.6-0.95 in binary systems favors formation of amorphous phases,[190] and local icosahedral structure in the first shell plays an important role in driving glass formation for Cu-Zr-Al metallic glasses.[186, 191] In our analysis, we observe an increase in

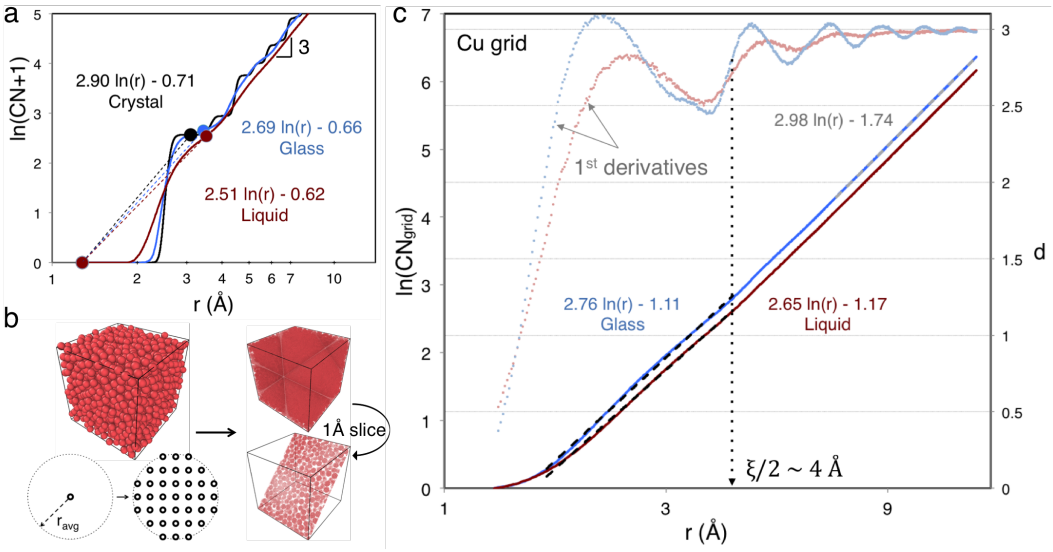

Figure 6.4: Comparison of crossovers in pure Cu systems using discrete and continuous counting methods. a) d~2.90 in Cu crystal, d~2.69 in Cu glass, and d~2.51 in Cu liquid below ξ counted by atom center positions. b) Schematic of the grid procedure. Cu atoms in the simulation box (left) are replaced by effective grid points representing their physical volume. Grid points capture the overall atomic structure (see 1 Åslice, right) b) Crossovers in dimension from d~2.65 and d~2.76 to d~3 for Cu liquid and glass, respectively, using a grid method for continuous counting. Here CN_{grid} is the normalized coordination number based on counting grids within each atom. Inset: 1^{st} derivative of $\ln(CN_{grid})$ versus r showing a distinct crossover near ξ~8Å.

d from ~2.55-2.65 to ~2.71-2.76 from the liquid to glass phases, suggesting that some ordering occurs across the glass transition in these metallic alloys and metals. This ordering can be seen more clearly in the grid analysis of Cu liquid and glass structures (Figure 6.4c). The two main observations from this analysis are: 1) the short-range dimension (slope of the $\ln(CN_{grid})$ vs. r plot from ~1.5 Åto ~4 Å) is $d_{Cuglass} \approx 2.76$ for the Cu glass, ~0.11 higher than that of the liquid phase, which has $d_{Culiquid} \approx 2.65$, and 2) 1^{st} derivative curves of the $\ln(CN_{grid})$ vs. r shows the development of ordering: the first peak is sharper, reaching a slope of around 3, indicating ordering in the first nearest neighbors, and a shoulder appears near the first minimum. Absolute slope changes in d of 0.11-0.16 across the glass transition are small, representing only a ~4-6% increase. However, we should keep in mind that the values for d are constrained to be from 2 to 3, as these structures occupy 3-dimensional space. With this in mind, the relative changes in slopes are actually closer to ~20-30%.

The liquid-glass transition appears to be a universal phenomenon in that any liquid can vitrify with sufficiently fast cooling.[172] Diverging relaxation time and viscosity can happen with or without accompanying structural changes. In these metallic systems, the structural changes that appear across the glass transition may be unique ? other common glasses such as covalent network glasses or molecular glasses have not yet been studied in this way, although the methods presented here can be extended to study those systems. Nonetheless, the structural effects observed in this study on metallic glasses may be instructive for a more general understanding of the liquid-glass transition. Our observations in these metallic glasses are directly related to the isotropic nature of their metallic bonds as well as a lack of molecular structures, and they should be placed within this context. In network glasses like silicates or chalcogenides, the directionality and nature of their bonds dictate their structures, so a different context must be considered. For example, oxide glasses with good glass forming ability possess similar structural characteristics pertaining to the nature of their oxygen bonds, according to Zachariasen?s rules based on empirical observations, which provide a heuristic explanation for why certain oxides like SiO2 and GeO2 are great glass formers and MgO and Na2O are not. Because glasses have vastly different chemical bonding (e.g. silicates?covalent, KNO3-Ca(NO3)2?ionic, ortho-terphenyl?van der Waals, glycerol?hydrogen, and CuZr?metallic), it is unlikely that the structural changes (or lack thereof) across the glass transition would be the same for all of these classes of systems. The unifying theme for these disparate systems is the arrest in molecular motion near T_g, which may occur via geometric constraints, but such constraints are subject to chemical bonding considerations.

In our metallic systems, the glass transition is accompanied by ordering/densification, increasing the local dimension of glasses over their liquid counterparts. The short-range dimension in our metallic glasses, d ~2.71-2.76, in contrast to our metallic liquids, deviates considerably from percolation models, where the fractal dimension is d ~2.52. In simple percolation models, the constituent units occupy lattice sites or are allowed to overlap one another[173] such that no limit exists for the site occupancy probability or volume fraction of overlapped spheres. In real systems and hard sphere percolation models, the constituent spherical particles (e.g. metallic atoms) have excluded volume. A fundamental limit exists in the *random* close packing fraction of hard spheres, which is ~0.637 for monodisperse spheres,[192] and ~0.64-0.83 for bi-disperse spheres, depending on their radii ratios and compositions.[193] Stable binary metallic glasses have high packing fractions: ~0.73

for our $Cu_{46}Zr_{54}$ (FF_2) and above ~0.7 for other binary alloys.[194] The densification/ordering that occurs in these systems at the atomic level may be due to the frustration and jamming of the atoms, whose packing approaches and exceeds the packing fractions allowed by the random close packing of hard spheres, arresting molecular motion. A similar idea has been explored in granular materials; Xia, et al. found that polytetrahedra serve as structural elements to glassy order in hard-sphere particle glasses, forming a globally jammed fractal structure.[**hardsphereglass**] The mechanism for geometrical constraint in our systems may be similar to ideas in jamming or rigidity percolation.[195, 196]

We find that the cumulative CN analysis shows a crossover in dimension for both metallic glasses and liquids. We observe that the short-range dimension is less than 3, d ~2.55-2.71 for both liquids and glasses. The long-range dimension, d, crosses over to 3 beyond the first coordination shell, which suggests that the underlying structures in these metallic liquids and glasses show parallels to percolation models that exhibit similar values of short-range fractal dimension, d ~2.52, with a similar crossover.

Chapter 7

DISCUSSION AND COMMENTS ON THE RESULTS AND FUTURE DIRECTIONS

We determined that the size-effect of emergent ductility in metallic glass nanowires comes from the increased surface-area-to-volume ratio in these samples. The free surfaces provide an additional pathway for the samples to relax their strain energy during deformation, which prolongs and delays inevitable failure via shear banding at room temperatures. This is an *intrinsic* mechanism for metallic glasses to have tensile ductility at room temperatures. The essential observation is that free surface atoms may more readily activate shear transformation zones and cooperatively shear. Somewhat equivalent mechanisms occur at higher temperatures, where the activation barriers for shear is lowered, and in metallic glasses with more free volume (such as sputtered metallic glasses), where the structure is less relaxed and has higher energy to overcome activation barriers. A take-home message of these nano-tensile experiments is that metallic glasses have properties that are extremely sensitive to their fabrication histories. While most observations of the brittle-to-ductile transition have occurred in ~100 nm samples, this is more of a coincidence that resulted from the similarities in the effective cooling rates the samples had been prepared under. Nano-moulded wires of metallic glass tend not to be ductile, and FIB-carved wires tend to be much more ductile. Electroplated wires fall somewhere in-between, and these differences can be explained in the context of their atomic-level structures, which are dictated by fabrication histories. These different sets of samples behave very differently in their mechanical response at these small scales, but their atomic-level structures appear nearly identical to us. For two identically-composed glasses, density differences should capture the structural dissimilarities. However, for two differently-composed glasses, density is no longer a useful comparison. For this reason, we explored models that utilize packing fraction, ϕ, as a parameter for describing these metallic glasses.

In our work on the so-called fractal medium-range structures proposed by Dong Ma, et al.[139] in metallic glasses, we found that the origin of the less-than-3 scaling observed in X-ray experiments is the short-range atomic structure, which is riddled with free volume of varying sizes. This distribution in free volume size contributes to an overall reduced dimension in these samples. However, this short-

range dimension is short-lived, only existing over ~8 Åor a few atomic diameters. Interestingly, this crossover in dimension from d~2.5-2.7 in these glassy and liquid structures to a dimension of $d = 3$ suggests some similarities to percolation clusters, which exhibit the same kind of crossovers. If we think about metallic glasses as semi-hard spheres percolating in a continuum, the structural properties that we probe using X-rays begins to make a lot more sense. One might wonder how something that is supposedly "fractal" may only exhibit fractal scaling over such a short range. Indeed, the self-similarity requirement for fractals may not be strictly satisfied by metallic glasses, which do not appear to have repeating scale-independent patterns. However, in the analogy to percolation clusters, the self-similarity comes from the clusters themselves, which are self-similar in percolation models. In metallic glasses, the self-similarity may not observed because the packing fraction is large ~0.7, creating loose clusters that are small, only on average containing ~10 atoms, which is incidentally also the average size of STZs.

It is not clear at this point whether the percolation model for metallic glasses will be a fruitful way to think about their structure. Right now, the link between the two is the dimensional crossover from $d < 3$ to $d = 3$ at a correlation length ξ that seems to fall in agreement with expected values from percolation theory. Another issue with this potential connection between percolation clusters and metallic glasses is the practical use of this model. While it is potentially exciting to have a model capable of encapsulating the atomic-level details in an amorphous material, the useful information that the model provides will ultimately determine whether it is a fruitful way to think about these materials. Currently, percolation theory can be used to quantify the distribution of clusters sizes in the system. Orbach has also used percolation to explain the high frequency (short wavelength) vibrational details in glasses.[161] I think this is just the beginning in what will be a shift in how we approach disordered materials. The missing piece to the puzzle is how we can capture and understand the topology of the way in which the atoms are interconnected. Crystals have a trivial topology (periodic in xyz directions), but amorphous materials, granular materials, colloids, and soft matter systems all tend to have apparently very complex, disordered topologies. However, there also appears to be some underlying order to the chaos. Crumple up a piece of paper, and you have just made a fractal object with a unique configuration of folds and creases that has never before existed in the history of the universe! This ball of crumpled paper, while unique, is just like any other ball of crumpled paper in overall shape and properties. Likewise, if we look at a satellite image of a river (also a fractal), we

can be convinced that what we are looking at is a naturally-formed river no matter if the picture was taken over Earth or Mars. Disorder is complex for us because our brains are used to thinking linearly. If we can grasp the underlying order within disorder, we will gain a new level of understanding and engineering control over these ubiquitous yet intractable materials.

BIBLIOGRAPHY

(1) Duwez, P.; Willens, R. H.; Klement, W. *Journal of Applied Physics* **1960**, *31*, 1136–1137.

(2) Schuh, C. A.; Hufnagel, T. C.; Ramamurty, U. *Acta Materialia* **2007**, *55*, 4067–4109.

(3) Hofmann, D. C.; Suh, J. Y.; Wiest, A.; Duan, G.; Lind, M. L.; Demetriou, M. D.; Johnson, W. L. *Nature* **2008**, *451*, 1085–U3.

(4) Kim, J. Y.; Jang, D. C.; Greer, J. R. *Advanced Functional Materials* **2011**, *21*, 4550–4554.

(5) Qiu, S. B.; Gong, P.; Yao, K. F. *Chinese Science Bulletin* **2011**, *56*, 3942–3947.

(6) Chen, C. Q.; Pei, Y. T.; De Hosson, J. T. M. *Acta Materialia* **2010**, *58*, 189–200.

(7) Jang, D. C.; Gross, C. T.; Greer, J. R. *International Journal of Plasticity* **2011**, *27*, 858–867.

(8) Volkert, C. A.; Donohue, A.; Spaepen, F. *Journal of Applied Physics* **2008**, *103*.

(9) Guo, H.; Yan, P. F.; Wang, Y. B.; Tan, J.; Zhang, Z. F.; Sui, M. L.; Ma, E. *Nature Materials* **2007**, *6*, 735–739.

(10) Jang, D. C.; Greer, J. R. *Nature Materials* **2010**, *9*, 215–219.

(11) Schuster, B. E.; Wei, Q.; Hufnagel, T. C.; Ramesh, K. T. *Acta Materialia* **2008**, *56*, 5091–5100.

(12) Wu, X. L.; Guo, Y. Z.; Wei, Q.; Wang, W. H. *Acta Materialia* **2009**, *57*, 3562–3571.

(13) Dubach, A.; Raghavan, R.; Loffler, J. F.; Michler, J.; Ramamurty, U. *Scripta Materialia* **2009**, *60*, 567–570.

(14) Magagnosc, D. J.; Ehrbar, R.; Kumar, G.; He, M. R.; Schroers, J.; Gianola, J. *Scientific Reports* **2013**, *3*, 6.

(15) Myers, M. T.; Charnvanichborikarn, S.; Wei, C. C.; Luo, Z. P.; Xie, G. Q.; Kucheyev, S. O.; Lucca, D. A.; Shao, L. *Scripta Materialia* **2012**, *67*, 887–890.

(16) Fu, E. G.; Carter, J.; Martin, M.; Xie, G. Q.; Zhang, X.; Wang, Y. Q.; Littleton, R.; McDeavitt, S.; Shao, L. *Nuclear Instruments & Methods in Physics Research Section B-Beam Interactions with Materials and Atoms* **2010**, *268*, 545–549.

(17) Carter, J.; Fu, E. G.; Martin, M.; Xie, G. Q.; Zhang, X.; Wang, Y. Q.; Wijesundera, D.; Wang, X. M.; Chu, W. K.; McDeavitt, S. M.; Shao, L. *Nuclear Instruments & Methods in Physics Research Section B-Beam Interactions with Materials and Atoms* **2009**, *267*, 2827–2831.

(18) Xiao, Q.; Huang, L.; Shi, Y. *Journal of Applied Physics* **2012**, *113*, 083514.

(19) Kumar, G.; Tang, H. X.; Schroers, J. *Nature* **2009**, *457*, 868–872.

(20) Usuzaka, N.; Yamaguchi, H.; Watanabe, T. *Materials Science and Engineering* **1988**, *99*, 105–108.

(21) Hata, S.; Sato, K.; Shimokohbe, A. *Device and Process Technologies for Mems and Microelectronics* **1999**, *3892*, 97–108.

(22) Cheng, Y.; Ding, J.; Ma, E. *Materials Research Letters* **2013**, *1*, 3–12.

(23) Shen, Y. F.; Liu, W. N.; Sun, X.; Xue, W. Y.; Wang, Y. D.; Zuo, L.; Liaw, P. K. *Metallurgical and Materials Transactions a-Physical Metallurgy and Materials Science* **2012**, *43A*, 1610–1620.

(24) Landau, P.; Q., G.; K., H.; R., G. J. *Advanced Functional Materials* **2013**, *23*, 1281–1288.

(25) Gu, X.; Loynachan, C. N.; Wu, Z. X.; Zhang, Y. W.; Srolovitz, D. J.; Greer, J. R. *Nano Letters* **2012**, *12*, 6385–6392.

(26) Greer, J. R.; De Hosson, J. T. M. *Prog Mater Sci* **2011**, *56*, 654–724.

(27) Chang, S. Y.; Lee, Y. S.; Hsiao, H. L.; Chang, T. K. *Metall Mater Trans A* **2006**, *37A*, 2939–2945.

(28) Argon, A. S.; Kuo, H. Y. *Materials Science and Engineering* **1979**, *39*, 101–109.

(29) Falk, M. L.; Langer, J. S. *Physical Review E* **1998**, *57*, 7192–7205.

(30) Harmon, J. S.; Demetriou, M. D.; Johnson, W. L.; Samwer, K. *Physical Review Letters* **2007**, *99*.

(31) Spaepen, F. *Acta Metallurgica* **1977**, *25*, 407–415.

(32) Wu, Z. X.; Zhang, Y. W.; Jhon, M. H.; Gao, H. J.; Srolovitz, D. J. *Nano Letters* **2012**, *12*, 910–914.

(33) Plimpton, S. *Journal of Computational Physics* **1995**, *117*, Qk448 Times Cited:4432 Cited References Count:56, 1–19.

(34) Pun, G. P. P.; Mishin, Y. *Philosophical Magazine* **2009**, *89*, 528XV Times Cited:12 Cited References Count:81, 3245–3267.

(35) Shi, Y. F. *Applied Physics Letters* **2010**, *96*.

(36) Thamburaja, P. *Journal of the Mechanics and Physics of Solids* **2011**, *59*, 1552–1575.

(37) Zhang, Z. F.; Eckert, J.; Schultz, L. *Acta Materialia* **2003**, *51*, 648EY Times Cited:413 Cited References Count:30, 1167–1179.

(38) Chen, C. Q.; Pei, Y. T.; Kuzmin, O.; Zhang, Z. F.; Ma, E.; De Hosson, J. T. M. *Physical Review B* **2011**, *83*, 800BU Times Cited:13 Cited References Count:19.

(39) Kuzmin, O. V.; Pei, Y. T.; De Hosson, J. T. M. *Applied Physics Letters* **2011**, *98*, 777XQ Times Cited:5 Cited References Count:22.

(40) Raghavan, R.; Boopathy, K.; Ghisleni, R.; Pouchon, M. A.; Ramamurty, U.; Michler, J. *Scripta Materialia* **2010**, *62*, 462–465.

(41) Raghavan, R.; Kombaiah, B.; Dobeli, M.; Erni, R.; Ramamurty, U.; Michler, J. *Materials Science and Engineering a-Structural Materials Properties Microstructure and Processing* **2012**, *532*, 407–413.

(42) Liu, Y. H.; Zhao, F.; Li, Y. L.; Chen, M. W. *Journal of Applied Physics* **2012**, *112*.

(43) Jang, D. C.; Greer, J. R. *Nature Materials* **2010**, *9*, 557WN Times Cited:106 Cited References Count:30, 215–219.

(44) Chen, D. Z.; Jang, D.; Guan, K. M.; An, Q.; Goddard W. A., 3.; Greer, J. R. *Nano Lett* **2013**, *13*, Chen, D Z Jang, D Guan, K M An, Q Goddard, W A 3rd Greer, J R eng Research Support, U.S. Gov't, Non-P.H.S. 2013/08/28 06:00 Nano Lett. 2013 Sep 11;13(9):4462-8. doi: 10.1021/nl402384r. Epub 2013 Aug 30., 4462–8.

(45) Guo, H.; Yan, P. F.; Wang, Y. B.; Tan, J.; Zhang, Z. F.; Sui, M. L.; Ma, E. *Nature Materials* **2007**, *6*, 216GO Times Cited:160 Cited References Count:34, 735–739.

(46) Tian, L.; Shan, Z. W.; Ma, E. *Acta Materialia* **2013**, *61*, 180NH Times Cited:10 Cited References Count:37, 4823–4830.

(47) Magagnosc, D. J.; Ehrbar, R.; Kumar, G.; He, M. R.; Schroers, J.; Gianola, D. S. *Scientific Reports* **2013**, *3*, 075KW Times Cited:3 Cited References Count:41.

(48) Falk, M. L. *Physical Review B* **1999**, *60*, 239PD Times Cited:117 Cited References Count:38, 7062–7070.

(49) Lund, A. C.; Schuh, C. A. *Acta Materialia* **2003**, *51*, 735NH Times Cited:111 Cited References Count:58, 5399–5411.

(50) Delogu, F. *Physical Review Letters* **2008**, *100*, 320JW Times Cited:30 Cited References Count:35.

(51) Ju, J. D.; Jang, D.; Nwankpa, A.; Atzmon, M. *Journal of Applied Physics* **2011**, *109*, 735BH Times Cited:11 Cited References Count:45.

(52) Choi, I. C.; Zhao, Y.; Yoo, B. G.; Kim, Y. J.; Suh, J. Y.; Ramamurty, U.; Jang, J. I. *Scripta Materialia* **2012**, *66*, 936WY Times Cited:6 Cited References Count:23, 923–926.

(53) Argon, A. S. *Acta Metallurgica* **1979**, *27*, Gg809 Times Cited:1093 Cited References Count:36, 47–58.

(54) Falk, M. L.; Langer, J. S. *Physical Review E* **1998**, *57*, Zu947 Times Cited:556 Cited References Count:47, 7192–7205.

(55) Schuh, C. A.; Hufnagel, T. C.; Ramamurty, U. *Acta Materialia* **2007**, *55*, 4067–4109.

(56) Lu, J.; Ravichandran, G.; Johnson, W. L. *Acta Materialia* **2003**, *51*, 701VH Times Cited:327 Cited References Count:45, 3429–3443.

(57) Spaepen, F. *Acta Metallurgica* **1977**, *25*, Df425 Times Cited:1337 Cited References Count:33, 407–415.

(58) Megusar, J.; Argon, A. S.; Grant, N. J. *Materials Science and Engineering* **1979**, *38*, Gu144 Times Cited:59 Cited References Count:19, 63–72.

(59) Volkert, C. A.; Donohue, A.; Spaepen, F. *Journal of Applied Physics* **2008**, *103*, 295DW Times Cited:110 Cited References Count:37.

(60) Greer, J. R.; Nix, W. D. *Physical Review B* **2006**, *73*, 058XC Times Cited:268 Cited References Count:24.

(61) Hofmann, D. C.; Suh, J. Y.; Wiest, A.; Duan, G.; Lind, M. L.; Demetriou, M. D.; Johnson, W. L. *Nature* **2008**, *451*, 266RB Times Cited:347 Cited References Count:29, 1085–U3.

(62) Sarac, B.; Schroers, J. *Nature Communications* **2013**, *4*, 208XR Times Cited:1 Cited References Count:43.

(63) Polman, A.; Atwater, H. A. *Nature Materials* **2012**, *11*, 174–177.

(64) Boukai, A. I.; Bunimovich, Y.; Tahir-Kheli, J.; Yu, J. K.; Goddard, W. A.; Heath, J. R. *Nature* **2008**, *451*, 168–171.

(65) Huang, Y.; Duan, X. F.; Cui, Y.; Lauhon, L. J.; Kim, K. H.; Lieber, C. M. *Science* **2001**, *294*, 1313–1317.

(66) Cui, Y.; Lieber, C. M. *Science* **2001**, *291*, 851–853.

(67) Bruchez, M.; Moronne, M.; Gin, P.; Weiss, S.; Alivisatos, A. P. *Science* **1998**, *281*, 2013–2016.

(68) Hao, S. J. et al. *Science* **2013**, *339*, 1191–1194.

(69) Schaedler, T. A.; Jacobsen, A. J.; Torrents, A.; Sorensen, A. E.; Lian, J.; Greer, J. R.; Valdevit, L.; Carter, W. B. *Science* **2011**, *334*, 962–965.

(70) Uchic, M. D.; Dimiduk, D. M.; Florando, J. N.; Nix, W. D. *Science* **2004**, *305*, 986–989.

(71) Greer, J. R.; De Hosson, J. T. M. *Prog. Mater. Sci.* **2011**, *56*, 654–724.

(72) Chan, C. K.; Peng, H. L.; Liu, G.; McIlwrath, K.; Zhang, X. F.; Huggins, R. A.; Cui, Y. *Nature Nanotechnology* **2008**, *3*, 31–35.

(73) Jang, D. C.; Greer, J. R. *Nature Materials* **2010**, *9*, 215–219.

(74) Beaber, A. R.; Nowak, J. D.; Ugurlu, O.; Mook, W. M.; Girshick, S. L.; Ballarini, R.; Gerberich, W. W. *Philosophical Magazine* **2011**, *91*, 1179–1189.

(75) Meyers, M. A.; McKittrick, J.; Chen, P. Y. *Science* **2013**, *339*, 773–779.

(76) Gu, X. W.; Jafary-Zadeh, M.; Chen, D. Z.; Wu, Z.; Zhang, Y.-W.; Srolovitz, D. J.; Greer, J. R. *Nano Letters* **2014**, *14*, PMID: 25198652, 5858–5864.

(77) Chen, D. Z.; Jang, D.; Guan, K. M.; An, Q.; Goddard W. A., 3.; Greer, J. R. *Nano Letters* **2013**, *13*, 4462–4468.

(78) Magagnosc, D. J.; Ehrbar, R.; Kumar, G.; He, M. R.; Schroers, J.; Gianola, D. S. *Scientific Reports* **2013**, *3*, 1–6.

(79) Hofmann, D. C.; Suh, J. Y.; Wiest, A.; Duan, G.; Lind, M. L.; Demetriou, M. D.; Johnson, W. L. *Nature* **2008**, *451*, 1083–1085.

(80) Ritchie, R. O. *Nature Materials* **2011**, *10*, 817–822.

(81) Schuh, C. A.; Hufnagel, T. C.; Ramamurty, U. *Acta Materialia* **2007**, *55*, 4067–4109.

(82) Qu, R. T.; Calin, M.; Eckert, J.; Zhang, Z. F. *Scripta Materialia* **2012**, *66*, 733–736.

(83) Sha, Z. D.; Pei, Q. X.; Sorkin, V.; Branicio, P. S.; Zhang, Y. W.; Gao, H. J. *Appl. Phys. Lett.* **2013**, *103*, 081903.

(84) Gao, H. J.; Ji, B. H.; Jager, I. L.; Arzt, E.; Fratzl, P. *PNAS* **2003**, *100*, 5597–5600.

(85) Gao, H. J.; Chen, S. H. *J. Appl. Mech.-Trans. ASME* **2005**, *72*, 732–737.

(86) Gu, X. W.; Wu, Z. X.; Zhang, Y. W.; Srolovitz, D. J.; Greer, J. R. *Nano Letters* **2013**, *13*, 5703–5709.

(87) Kumar, S.; Haque, M. A.; Gao, H. *Appl. Phys. Lett.* **2009**, *94*, 253104.

(88) Zhang, T.; Li, X. Y.; Kadkhodaei, S.; Gao, H. J. *Nano Letters* **2012**, *12*, 4605–4610.

(89) Burek, M. J.; Greer, J. R. *Nano Letters* **2010**, *10*, 69–76.

(90) Kim, J. Y.; Jang, D. C.; Greer, J. R. *Scripta Materialia* **2009**, *61*, 300–303.

(91) Volkert, C. A.; Donohue, A.; Spaepen, F. J. *J. Appl. Phys.* **2008**, *103*, 083539.

(92) Ackland, G.; Mendelev, M.; Srolovitz, D.; Han, S.; Barashev, A. *J. Phys.: Condens. Matter* **2004**, *16*, S2629.

(93) Plimpton, S. *J. Comput. Phys.* **1995**, *117*, 1–19.

(94) Shimizu, F.; Ogata, S.; Li, J. *J. Mater. T.* **2007**, *48*, 2923–2927.

(95) Stukowski, A. *Modell. Simula. Mater. Sci. Eng.* **2010**, *18*, 015012.

(96) Murali, P.; Guo, T. F.; Zhang, Y. W.; Narasimhan, R.; Li, Y.; Gao, H. J. *Phys. Rev. Lett.* **2011**, *107*, 215501.

(97) Needleman, A. *J. Appl. Mech.-Trans. ASME* **1987**, *54*, 525–531.

(98) Seppala, E. T.; Belak, J.; Rudd, R. E. *Phys. Rev. B* **2004**, *69*, 134101.

(99) Klement, W.; Willens, R. H.; Duwez, P. *Nature* **1960**, *187*, 869–870.

(100) Johnson, W. L. *Prog. Mater. Sci.* **1986**, *30*, 81–134.

(101) Inoue, A. *Acta Materialia* **2000**, *48*, 279–306.

(102) Schuh, C. A.; Hufnagel, T. C.; Ramamurty, U. *Acta Materialia* **2007**, *55*, 4067–4109.

(103) Wang, W. H.; Dong, C.; Shek, C. H. *Mater. Sci. Eng. R Rep.* **2004**, *44*, 45–89.

(104) Lee, S.-W.; Huh, M.-Y.; Fleury, E.; Lee, J.-C. *Acta Materialia* **2006**, *54*, 349–355.

(105) Hofmann, D. C.; Suh, J.-Y.; Wiest, A.; Duan, G.; Lind, M.-L.; Demetriou, M. D.; Johnson, W. L. *Nature* **2008**, *451*, 1085–1089.

(106) Hofmann, D. C.; Suh, J.-Y.; Wiest, A.; Lind, M.-L.; Demetriou, M. D.; Johnson, W. L. *PNAS* **2008**, *105*, 20136–20140.

(107) Qiao, J. W.; Wang, S.; Zhang, Y.; Liaw, P. K.; Chen, G. L. *Appl. Phys. Lett.* **2009**, *94*, 151905.

(108) Uchic, M. D.; Dimiduk, D. M.; Shade, P. A. *Annu. Rev. Matter. Res.* **2009**, *39*, 361–386.

(109) Kraft, O.; Gruber, P. A.; Monig, R.; Weygand, D. *Annu. Rev. Matter. Res.* **2010**, *40*, 293–317.

(110) Greer, J. R.; De Hosson, J. T. M. *Prog. Mater. Sci.* **2011**, *56*, 654–724.

(111) Volkert, C. A.; Donohue, A.; Spaepen, F. *J. Appl. Phys.* **2008**, *103*, 083539.

(112) Jang, D.; Greer, J. R. *Nature Materials* **2010**, *9*, 215–219.

(113) Chen, D. Z.; Jang, D.; Guan, K. M.; An, Q.; Goddard, W. A.; Greer, J. R. *Nano Letters* **2013**, *13*, 4462–4468.

(114) Chen, D. Z.; Gu, X. W.; An, Q.; Goddard, W. A.; Greer, J. R. *Appl. Phys. Lett.* **2015**, *106*, 061903.

(115) Magagnosc, D. J.; Ehrbar, R.; Kumar, G.; He, M. R.; Schroers, J.; Gianola, D. S. *Sci. Rep.* **2013**, *3*, 1–6.

(116) Magagnosc, D. J.; Kumar, G.; Schroers, J.; Felfer, P.; Cairney, J. M.; Gianola, D. S. *Acta Materialia* **2014**, *74*, 165–182.

(117) Jung, P.; Ullmaier, H. *J. Nucl. Mater.* **1990**, *174*, 253–263.

(118) Victoria, M.; Baluc, N.; Bailat, C.; Dai, Y.; Luppo, M.; Schaublin, R.; Singh, B. *J. Nucl. Mater.* **2000**, *276*, 114–112.

(119) Odette, G. R.; Lucas, G. E. *JOM* **2001**, *53*, 18–22.

(120) Trinkaus, H.; Singh, B. *Proc. Second IEA Fusion Mater. Agreem. Workshop Model. Exp. Valid.* **2003**, *323*, 229–242.

(121) Schaedler, T. A.; Jacobsen, A. J.; Torrents, A.; Sorensen, A. E.; Lian, J.; Greer, J. R.; Valdevit, L.; Carter, W. B. *Science* **2011**, *334*, 962–965.

(122) Jang, D.; Meza, L. R.; Greer, F.; Greer, J. R. *Nature Materials* **2013**, *12*, 893–898.

(123) Meza, L. R.; Das, S.; Greer, J. R. *Science* **2014**, *345*, 1322–1326.

(124) Meza, L.; Greer, J. *J. Mater. Sci.* **2014**, *49*, 2496–2508.

(125) Montemayor, L. C.; Meza, L. R.; Greer, J. R. *Adv. Eng. Mater.* **2014**, *16*, 184–189.

(126) Rys, J.; Valdevit, L.; Schaedler, T. A.; Jacobsen, A. J.; Carter, W. B.; Greer, J. R. *Adv. Eng. Mater.* **2014**, *16*, 889–896.

(127) Kim, J.-Y.; Jang, D.; Greer, J. R. *Adv. Funct. Mater.* **2011**, *21*, 4550–4554.

(128) Lee, S.-W.; Meza, L.; Greer, J. R. *Appl. Phys. Lett.* **2013**, *103*.

(129) Lee, S.-W.; Cheng, Y.; Ryu, I.; Greer, J. *Sci. China Technol. Sci.* **2014**, *57*, 652–662.

(130) Li, Q.-K.; Li, M. *Appl. Phys. Lett.* **2006**, *88*, 241903.

(131) Bailey, N. P.; Schiotz, J.; Jacobsen, K. W. *Phys. Rev. B* **2006**, *73*, 064108.

(132) Angell, C. A. *Science* **1995**, *267*, 1924–1935.

(133) Debenedetti, P. G.; Stillinger, F. H. *Nature* **2001**, *410*, 259–267.

(134) Miracle, D. B. *Nature Materials* **2004**, *3*, 697–702.

(135) Sheng, H. W.; Luo, W. K.; Alamgir, F. M.; Bai, J. M.; Ma, E. *Nature* **2006**, *439*, 419–425.

(136) Hirata, A.; Guan, P. F.; Fujita, T.; Hirotsu, Y.; Inoue, A.; Yavari, A. R.; Sakurai, T.; Chen, M. W. *Nature Materials* **2011**, *10*, 28–33.

(137) Sietsma, J.; Thijsse, B. J. *Journal of Non-Crystalline Solids* **1991**, *135*, 146–154.

(138) Keys, A. S.; Abate, A. R.; Glotzer, S. C.; Durian, D. J. *Nature Physics* **2007**, *3*, 260–264.

(139) Ma, D.; Stoica, A. D.; Wang, X. L. *Nature Materials* **2009**, *8*, 30–34.

(140) Zeng, Q. S.; Kono, Y.; Lin, Y.; Zeng, Z. D.; Wang, J. Y.; Sinogeikin, S. V.; Park, C.; Meng, Y.; Yang, W. G.; Mao, H. K.; Mao, W. L. *Physical Review Letters* **2014**, *112*.

(141) Mandelbrot, B. B., *The fractal geometry of nature*, Updated and augmented.; W.H. Freeman: New York, 1983.

(142) Tallinen, T.; Astrom, J. A.; Timonen, J. *Nature Materials* **2009**, *8*, 25–29.

(143) Ma, X. F.; Zachariah, M. R.; Zangmeister, C. D. *Nano Letters* **2012**, *12*, 486–489.

(144) Miracle, D. B. *Acta Materialia* **2013**, *61*, 3157–3171.

(145) Cheng, Y. Q.; Ma, E. *Progress in Materials Science* **2011**, *56*, 379–473.

(146) Duan, G.; Xu, D. H.; Zhang, Q.; Zhang, G. Y.; Cagin, T.; Johnson, W. L.; Goddard, W. A. *Physical Review B* **2005**, *71*.

(147) Cheng, Y. Q.; Ma, E.; Sheng, H. W. *Physical Review Letters* **2009**, *102*.

(148) Mendelev, M. I.; Kramer, M. J.; Ott, R. T.; Sordelet, D. J.; Yagodin, D.; Popel, P. *Philosophical Magazine* **2009**, *89*, 967–987.

(149) Pun, G. P. P.; Mishin, Y. *Philosophical Magazine* **2009**, *89*, 3245–3267.

(150) Shante, V. K. S.; Kirkpatr.S *Advances in Physics* **1971**, *20*, 325–&.

(151) Sahimi, M., *Applications of Percolation Theory*; Taylor & Francis Ltd: Bristol, PA USA, 1994.

(152) Bunde, A.; Havlin, S., *Fractals and disordered systems*; Springer-Verlag New York, Inc.: New York, NY, USA, 1991.

(153) Scher, H.; Zallen, R. *Journal of Chemical Physics* **1970**, *53*, 3759–&.

(154) Wang, J. F.; Zhou, Z. Z.; Zhang, W.; Garoni, T. M.; Deng, Y. J. *Physical Review E* **2013**, *87*.

(155) .

(156) Powell, M. J. *Physical Review B* **1979**, *20*, 4194–4198.

(157) Lorenz, C. D.; Ziff, R. M. *Journal of Chemical Physics* **2001**, *114*, 3659–3661.

(158) Clarke, A. S.; Wiley, J. D. *Physical Review B* **1987**, *35*, 7350–7356.

(159) Liu, A. J.; Nagel, S. R. *Nature* **1998**, *396*, 21–22.

(160) Trappe, V.; Prasad, V.; Cipelletti, L.; Segre, P. N.; Weitz, D. A. *Nature* **2001**, *411*, 772–775.

(161) Orbach, R. *Science* **1986**, *231*, 814–819.

(162) Weeks, E. R.; Crocker, J. C.; Levitt, A. C.; Schofield, A.; Weitz, D. A. *Science* **2000**, *287*, 627–631.

(163) Li, Y.; Guo, Q.; Kalb, J. A.; Thompson, C. V. *Science* **2008**, *322*, 1816–1819.

(164) Yang, B.; Liu, C. T.; Nieh, T. G. *Applied Physics Letters* **2006**, *88*.

(165) Falk, M. L.; Langer, J. S. *Physical Review E* **1998**, *57*, 7192–7205.

(166) Falk, M. L. *Physical Review B* **1999**, *60*, 7062–7070.

(167) Lund, A. C.; Schuh, C. A. *Acta Materialia* **2003**, *51*, 5399–5411.

(168) Delogu, F. *Physical Review Letters* **2008**, *100*.

(169) Angell, C. A. *Science* **1995**, *267*, 1924–1935.

(170) Sheng, H. W.; Luo, W. K.; Alamgir, F. M.; Bai, J. M.; Ma, E. *Nature* **2006**, *439*, 419–425.

(171) Cheng, Y. Q.; Ma, E. *Progress in Materials Science* **2011**, *56*, 379–473.

(172) Debenedetti, P. G.; Stillinger, F. H. *Nature* **2001**, *410*, 259–267.

(173) Bunde, A.; Havlin, S., *Fractals and disordered systems*; Springer-Verlag New York, Inc.: New York, NY, USA, 1991.

(174) Ma, D.; Stoica, A. D.; Wang, X. L. *Nature Materials* **2009**, *8*, 30–34.

(175) Zeng, Q. S.; Kono, Y.; Lin, Y.; Zeng, Z. D.; Wang, J. Y.; Sinogeikin, S. V.; Park, C.; Meng, Y.; Yang, W. G.; Mao, H. K.; Mao, W. L. *Physical Review Letters* **2014**, *112*.

(176) Chen, D. Z.; Shi, C. Y.; An, Q.; Zeng, Q. S.; Mao, W. L.; Goddard, W. A.; Greer, J. R. *Science* **2015**, *349*, 1306–1310.

(177) Gangopadhyay, A. K.; Blodgett, M. E.; Johnson, M. L.; Vogt, A. J.; Mauro, N. A.; Kelton, K. F. *Applied Physics Letters* **2014**, *104*.

(178) Orbach, R. *Science* **1986**, *231*, 814–819.

(179) Powell, M. J. *Physical Review B* **1979**, *20*, 4194–4198.

(180) Frith, W. J.; Buscall, R. *Journal of Chemical Physics* **1991**, *95*, 5983–5989.

(181) Rintoul, M. D. *Physical Review E* **2000**, *62*, 68–72.

(182) Lorenz, C. D.; Ziff, R. M. *Journal of Chemical Physics* **2001**, *114*, 3659–3661.

(183) Bernal, J. D. *Nature* **1960**, *185*, 68–70.

(184) , making the overall fit for df particularly sensitive to the position of the initial peak at 0 GPa. In the previous analysis, a change in initial peak position of ~0.01 Åcan shift the exponent for d by ~0.2. In our current analysis using cumulative CN, a ~0.01 Åchange in r_{avg} or r_{1s} would result in a ~0.02 shift in the estimate for d. With our new analysis, the previous estimates of d~2.5 for $Cu_{46}Zr_{54}$ FF_1 and FF_2 and Ni_4Al now become d~2.74, 2.73, 2.68, respectively.

(185) Wang, J. F.; Zhou, Z. Z.; Zhang, W.; Garoni, T. M.; Deng, Y. J. *Physical Review E* **2013**, *87*.

(186) Cheng, Y. Q.; Ma, E.; Sheng, H. W. *Physical Review Letters* **2009**, *102*.

(187) Mendelev, M. I.; Kramer, M. J.; Ott, R. T.; Sordelet, D. J.; Yagodin, D.; Popel, P. *Philosophical Magazine* **2009**, *89*, 967–987.

(188) Steinhardt, P. J.; Nelson, D. R.; Ronchetti, M. *Physical Review B* **1983**, *28*, 784–805.

(189) Soklaski, R.; Tran, V.; Nussinov, Z.; Kelton, K. F.; Yang, L. *arXiv:1502.01739* **2015**.

(190) Lee, H. J.; Cagin, T.; Johnson, W. L.; Goddard, W. A. *Journal of Chemical Physics* **2003**, *119*, 9858–9870.

(191) An, Q.; Samwer, K.; Goddard, W. A.; Johnson, W. L.; Jaramillo-Botero, A.; Garret, G.; Demetriou, M. D. *Journal of Physical Chemistry Letters* **2012**, *3*, 3143–3148.

(192) Scott, G. D.; Kilgour, D. M. *Journal of Physics D-Applied Physics* **1969**, *2*, 863–.

(193) Farr, R. S.; Groot, R. D. *Journal of Chemical Physics* **2009**, *131*.

(194) Miracle, D. B. *Acta Materialia* **2013**, *61*, 3157–3171.

(195) Torquato, S.; Stillinger, F. H. *Journal of Physical Chemistry B* **2001**, *105*, 11849–11853.

(196) Trappe, V.; Prasad, V.; Cipelletti, L.; Segre, P. N.; Weitz, D. A. *Nature* **2001**, *411*, 772–775.

Appendix A

METHODS AND SUPPORTING INFORMATION

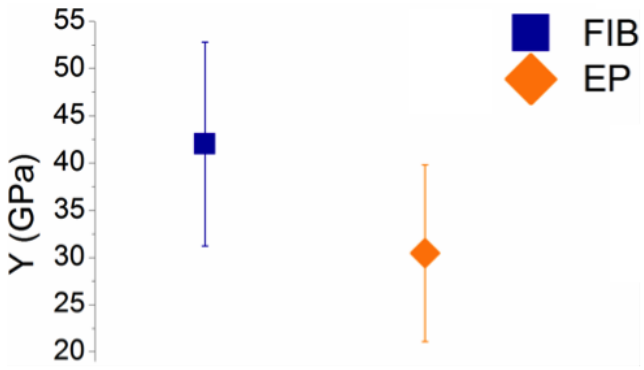

Figure A.1: Average Young's moduli for FIB and EP samples across ten independent specimens. Five samples of each type were tested. EP samples show a slightly lower modulus, but it is within one standard deviation.

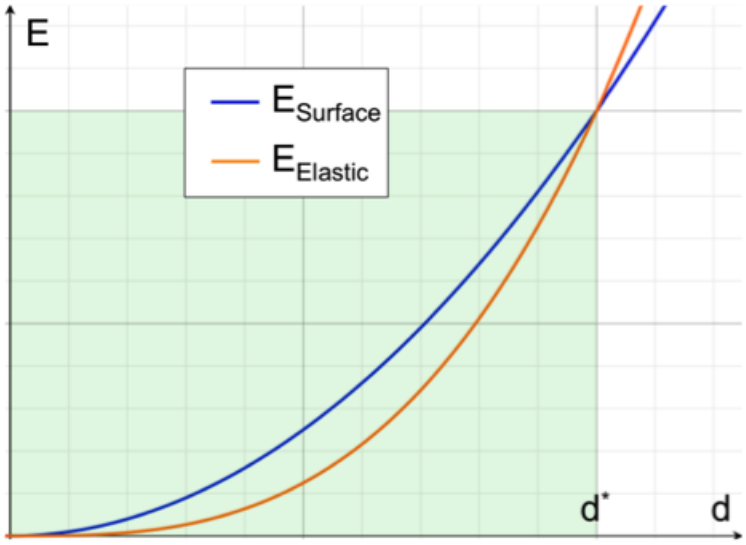

Figure A.2: Graph depicting the d^2 versus d^3 scaling argument for surface energy. $E_{Surface}$ and total stored elastic energy, $E_{Elastic}$. At diameters lower than d^* (opaque green region), the energy required for a crack/fracture to initiate at the surface ($E_{Surface}$) dominates, and shear banding is suppressed. Altering the surface state increases the gap between $E_{Surface}$ and $E_{Elastic}$, further suppressing catastrophic failure.

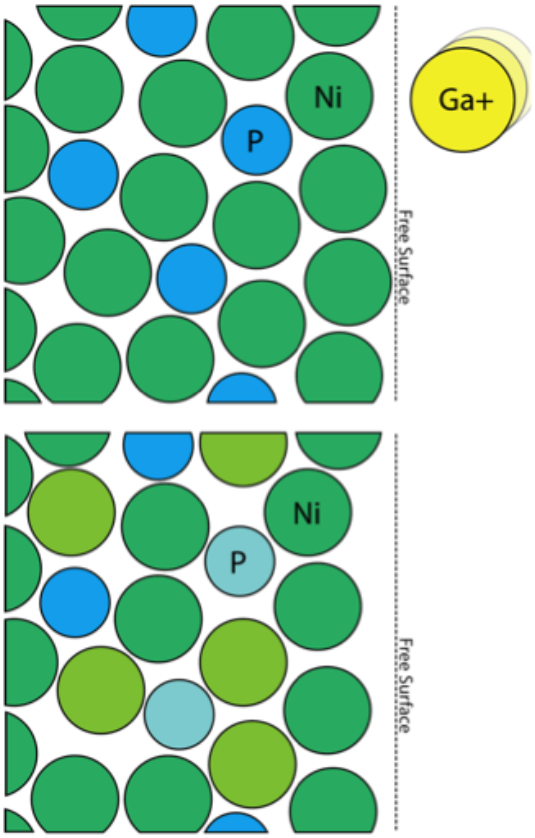

Figure A.3: Diagram for the generation of high potential energy atoms from ion irradiation. Top: as-cast configuration of NiP MG atoms, with the free surface to the right of the depicted atoms (not shown). Ga ions impinge upon the free surface from the right. Bottom: atoms rearrange after collision, resulting in high potential energy atoms - shown in light green for Ni and light blue for P. The free volume in the vicinity of these atoms is notably higher, creating an easy path for them to take in response to elastic energy input.

Bath composition (g/L)	Temperature (°C)	DC current density (mA/cm^2)	Anode
Nickel sulfamate: 90, Boric acid: 40, Nickel chloride: 3, Sodium dodecyl sulfate: 0.4, phosphorous acid: 40	50	80	Nickel plate

Table A.1: Electroplating conditions employed for plating both our Ni-P film (FIB) and templated (EP) specimen.

A.1 Supporting methods

Synthesis

Electroplated (EP) samples were fabricated following a template pattern transfer procedure described in.[1] In this methodology, a thin layer of Au (~100 nm) is

first evaporated onto a silicon wafer coated with a 30nm-thick Ti layer without breaking the vacuum. The ~700nm-thick PMMA is then spin-coated onto this seed layer, patterned using e-beam lithography, and developed to reveal vertical through-holes with the desired diameters. The electroplating is performed by providing a constant current between the anode (Ni foil) and the cathode (prepared template and Au dummy chip), and tension samples are made by overplating the metallic glass above the PMMA surface. Tables 2.1 & 2.2 provides details on the specific Ni-P electroplating conditions. More details about this fabrication method for other metallic nano structures can be found in ref. [1]. In addition to such templated electroplating, a blanket ~2μm-thick Ni-P film was electroplated directly onto the seed layer as a separate Si chip. This film had virtually identical composition to the nano-pillars (Table A.1 and Figure 2.2f). Tensile samples with ~100-nm and 500-nm diameters and ~650-nm and 2-μm gauge lengths were then fabricated from an electroplated NiP film using an FEI Nova 200 Nanolab focused ion beam with a final etching condition of 30kV/10pA (Figure 2.3). Great care was taken when carving the heads of the tension samples to minimize bending during nano-mechanical testing.

Tensile testing

A custom-made in situ SEM, SEMentor (SEM + nanoindenter), was used to conduct the nanomechanical tension tests.A.2 The nanoindentor arm is fitted with a diamond Berkovich tip that was carefully milled with FIB into the shape and dimensions of a tensile grip, as seen partially in Figures 2.3 & 3.3. All of the experiments were carried out at a constant nominal displacement rate (0.5-8 nms^{-1}) using a feedback algorithm, which results in a global strain rate of 1.0e-3s^{-1}. The raw load-displacement data were recorded after isolating the specimen-only response from the load frame, support spring, and substrate compliances. Engineering stress and strain values were then calculated from load-displacement data using the sample diameters measured from SEM images.

Molecular dynamics: nanowires

We started with a Ni_3Al crystal with a total of 4000 atoms and melted the system at 3000 K. Then 5% of the Al atoms were replaced by Ni atoms to form a $Cu_{46}Zr_{54}$ liquid. Periodic boundary conditions were applied in all three directions of the simulation box to eliminate surface effects. Equations of motion were solved using the velocity Verlet algorithm with a time step of 1 femtosecond. The dynamics were carried out with an NPT ensemble (constant particles, pressure, and temperature)

using a Nose-Hoover thermostat (time constant of 0.1 picosecond) and barostat (time constant of 1 picosecond).

In addition to the steps mentioned in the main text of the paper, periodic boundary conditions were applied only along the cylinder axis during quenching. Additionally, the length of the cylinder was fixed during this step as well. The irradiation step was performed using an NVE ensemble (constant particles, volume, and energy) for 200 picoseconds until the potential energy of the system stabilized. After this the irradiated pillars were immediately quenched to room temperature and relaxed using an NVT ensemble (constant particles, volume, and temperature) for 500 picoseconds. To avoid an unphysical attraction in this high-energy collision process, we applied a truncated and shifted Leonard-Jones pairwise interaction to the original EAM potential in the repulsive region. The form and parameters of the LJ potential are identical to that of Xiao, et al.[2] Uniaxial tension was conducted by rescaling the simulation box along the loading direction. The atomic stresses were obtained from the atomic virial[3] to extract the total stresses of the nanopillars.

The simulated irradiation fluence value of 0.0625/nm^2 was obtained from a back-of-the-envelope calculation using experimental FIB conditions on the FEI Nova 200 NanoLab DualBeamTM SEM/FIB. The dwell time for the beam was 1 µs, and the spot size was 2 nm^2. From these two parameters, we can use eq. A.1 to estimate the number of scans per milling session, given the user-specified FIB pattern area and a correction to the scan area for the 50% overlap in beam spot in both the x and y directions. From this estimate of the number of scans per session, we can use eq. A.2 to obtain the ion fluence by applying the number of ions per second needed to achieve an ion current of 10 pA, which results in a value of ~0.0625/nm^2.

$$N_{scans} = \frac{t_{final}}{\left(\frac{A_{FIB}}{A_{spot}} \times 2t_{dwell}\right)} \tag{A.1}$$

The factor 2 corresponds to a correction to the scan area for the 50% overlap in the beam spot for the x and y directions. A_{spot} is the spot size, A_{FIB} is the total pattern area, t_{final} is the final exposure time, and t_{dwell} is the total dwell time.

$$\phi = \frac{I_{ion} \times t_{sample}}{-e} \times \frac{N_{scans}}{10A_{FIB-affected}} \tag{A.2}$$

The factor 10 corresponds to a rough correction for the glancing angle of incidence for the incoming ion beam. I_{ion} is the ion current, t_{sample} is the FIB exposure time on

the sample surface, e is the electron charge, and $A_{FIB-affected}$ is the cross-sectional area of the FIB-affected zone on the sample surface.

Sample prep. for *in-situ* DAC

~40μm-diameter cylindrical samples of as-cast Cu46Zr46Al5Be3 metallic glass were carved from a millimeter-diameter rod using the Focused Ion Beam (FIB) in an FEI Nova 200 DualBeam system. A slice was cut into the cross-section of the rod, and then a top-down circular mill was performed to obtain the cylindrical shape. The sample was extracted from its as-milled hole with the aid of an optical microscope.

X-ray diffraction and tomography

Angle-dispersive X-ray diffraction were performed at beamline 16BM-D of the Advanced Photon Source (APS), Argonne National Laboratory (ANL) with a wavelength of 0.309846 Å. The sample was loaded into a 150 μm hole in a stainless steel gasket and compressed by diamonds anvils with 300 μm culets. Helium was used as the pressure-transmitting medium to guarantee hydrostatic pressure conditions. Loading was performed at the GeoSoilEnviroCARS of APS, ANL. X-ray images of the sample were collected using a full field TXM installed at beam line 6-2 of the Stanford Synchrotron Radiation Lightsource (SSRL), SLAC National Accelerator Laboratory. The sample was cut into a cylinder with a smooth surface using the FIB and then loaded along with a ruby ball as pressure calibrant into a 120-μm diameter sample chamber in an X-ray transparent beryllium (Be) gasket with cubic BN/epoxy insert. Silicone oil was used as the pressure-transmitting medium. The sample was compressed between a pair of 400 μm culet diamond anvils in a cross diamond anvil cell (X-DAC) with a viewing angle of 152°. The incident x-ray cone beam was fixed at 9240 eV, which is above the Cu K absorption edge to maximize the absorption contrast. The 2D projection images were collected during rotation of the 152° viewing angle with 1° intervals for each pressure point. 3D reconstruction of 2D projection images was performed using the TXM-Wizard software.[4] The algebraic reconstruction technique (ART) algorithm was applied to each sinogram with 20 iteration cycles. Segmentation and volume measurement was conducted using Avizo (FEI Visualization Sciences Group). The relative volume change as a function of pressure can be precisely measured. By keeping the contrast threshold values consistent for all the pressures points, we determined that the error associated with the relative volume change to be within 1%.

Cluster analysis (MD)

Honeycutt-Anderson (HA) analysis was performed to isolate icosahedral clusters in our simulated system by focusing on arrangements with the 1551 index.[5] This was done to illustrate the connectedness of the atomic arrangements within our model.

Atomic radii and packing fractions

We generated minimized crystal structures of pure face-centered cubic (FCC) Cu and pure hexagonal close-packed (HCP) Zr to obtain the atomic radii of each element, r_{Cu} = 1.278 Åand r_{Zr} = 1.5895 Åfor FF_1. We also generated crystals of $Cu_{50}Zr_{50}$, B2 body-centered cubic with non-identical atoms, and found the Cu-Zr pair separation to be 2.83 Å, a value ∼1.5% lower than r_{Cu} + r_{Zr}, suggesting that such measured atomic radii for this system are fairly robust to structural changes. Assuming the atomic radii for the glass to be similar, we obtained the room-temperature packing fractions of $Cu_{46}Zr_{54}$ using two different force fields: ϕ = 0.717 for FF_1 and 0.728 for FF_2. The values for the $Ni_{80}Al_{20}$ system were obtained in a similar way.

A.2 Supporting discussion

Short range order (SRO)

A Ni-P system was chosen because it lends itself well to electroplating. NiP metallic glasses may have different short range order (SRO) compared with the more common binary glass, CuZr, which has more metallic-like bonding.[6] Although the bonding between Ni and P may not be purely metallic, it should not adversely affect the role of Ni-P metallic glass as a model system nor does it change the findings or the conclusions of this work. Neutron diffraction experiments have also suggested that the pair distribution functions (PDFs) of metal-metalloid systems are qualitatively similar to metal-metal systems such as CuZr, especially after the second nearest neighbors.[7] It is not known whether the brittle-to-ductile transition occurs in only metallic glass systems or in other amorphous systems as well. A similar phenomenon has been seen in amorphous silica nanowires, which at 50-100nm-diameters undergo brittle failure[8] and at down to 20 nm exhibit great deformability[9]. The Cu-Zr which was shown to undergo the size-induced brittle-to-ductile transition (ref. [10] in the manuscript) has more of a metallic-type bonding, but cannot be considered to be purely metallic. Typically, a certain amount of covalent bonding or orientation preference is needed for the formation of an amorphous microstructure. Additionally, the microstructure of our NiP system is completely amorphous, as validated by TEM, and, as Argon et al.'s (ref. [11])

experiments have shown, even unrelated analogous systems such as bubble rafts can lead to rather applicable insights to the underlying deformation in amorphous systems, including metallic glasses.

Electroplating

The rate of metal ion deposition during electroplating was fairly consistent for both the films and the 100-nm template pillars, suggesting that the plating time is independent of template feature size. Even at 100nm-diameters, the electroplating remained reasonably unhindered by the template, which implies that the only relevant driving force for plating rate is the current density. From the SEM images, it can also be seen in Figure 2.3b & c that the electroplated pillars had relatively smooth surfaces, with few hydrogen bubbles, which are a common issue with electroplated samples.[12] Tensile specimens also have characteristic caps, which are a result of plating over the e-beam developed features. These caps are quite isotropic, and somewhat resemble mushroom tops. Isotropy in the overplated caps is an indicator for the presence of an amorphous rather than a crystalline phase, which might show some sort of anisotropy or orientation preference, as we have seen with our previous samples.[1]

Carbon and Oxygen contamination

EDX only detects the surface atoms, and due to the small size of the EP specimen, the spot size of the e-beam actually includes some of the atoms on the template surface as well as those on the specimens. We have re-normalized the chemical compositions based only on the relative Ni and P content to reflect this. The resulting difference in relative P content is less than 1 wt% between the two sample types, which makes them be nominally identical in terms of chemical composition, as planned. As mentioned in the manuscript, the O and C present on the surfaces of the samples should not form continuous layers, and as such do not bear any load. It may affect the straining slightly, but it is highly unlikely to induce plastic flow in an otherwise brittle glass.

Strain from *in-situ* video

Raw data obtained from the displacement signal of the nanoindenter produces results which have high variability in the loading moduli, an unavoidable characteristic detriment of nano-mechanical testing. Many factors can affect the apparent modulus: slight misalignments between the sample and the grip, surface imperfections on the

sample or the grip (bumps), the machine compliance, the imperfect adhesion, etc. to name a few. We have carefully re-examined the raw data and used the frames from the *in-situ* SEM videos rather than the displacement signal from the nanoindenter to measure and recalibrate the strains obtained in the mechanical data. This technique is more reliable for strain determination and has been successfully utilized in many publications from our group.[10, 13, 14] Such a discrepancy between the strain based on video frames and that measured in the nanoindenter is typical and likely stems from the effects of machine and grip compliances in both sample types and additional substrate effects in EP samples.

Strain rate in molecular dynamics

The strain rate of $10^8 s^{-1}$ applied in our simulations is of many orders of magnitude higher than the strain rate applied in our experiments, $10^{-3} s^{-1}$. Due to limitations in computational time and power, the time scale in MD is inevitably shorter than the experimental time scale. This is a common challenge in simulations, but it is not one that prevents useful insights to be made from atomistic modeling. It is unfeasible to operate in the regime of both qualitative and quantitative accuracy when interpreting MD results. For example, in dislocation systems, the strength of simulated samples can be highly dependent on strain rate even when the same mechanism governs the deformation.[15, 16] However, the aforementioned results still produce qualitatively accurate results that reveal significant deformation mechanisms. It is crucial to avoid the regime whereby qualitatively inaccurate results are obtained due to either the activation of unrepresentative processes or the exclusion of vital processes, which is possible in both dislocation systems[17] and amorphous systems[18]. In our simulations we avoided a static loading procedure because thermally activated processes would be excluded and they appear to be important in the physics we are attempting to capture. Of course, the high strain rates applied here will suppress these thermal processes, but since the fundamental mechanisms of relaxation and deformation in our experiment and simulations are the same, just happening at different rates, the results of our model should qualitatively capture the physical processes at hand.

Correlation length

$$\xi \propto |p - p_c|^{-\nu} \tag{A.3}$$

At $p = p_c$, ξ diverges, which signifies that the entire system is fractal with macro-

scopic pores. At $p < p_c$ and $p > p_c$, ξ is finite, and the system is only fractal on length scales shorter than the correlation length. At probabilities greater than the percolation threshold, $p > p_c$, the percolation cluster is defined by,

$$M(r) \propto \begin{cases} r^{D_f}, & r \gg \xi \\ r^{D}, & r \ll \xi \end{cases} \tag{A.4}$$

In Eq. A.4, we modified $M(r) \sim r^{D_f}$ to be represented by a piecewise equation that depends on ξ. To test our hypothesis that there must be a length beyond which the samples no longer exhibit fractal behavior, we modified Eq. A.4 to better represent the experimentally obtained volume, V, which is related to mass through density, and the interatomic spacing, r_i, where i is the peak number or neighbor number. This gives:

$$V(r) \propto {r_i}^{D_f} \tag{A.5}$$

Eq. A.5 then becomes,

$$V(r) \propto \begin{cases} {r_i}^{D_f}, & i \gg \xi \\ {r_i}^{D}, & i \ll \xi \end{cases} \tag{A.6}$$

with both i and ξ described by pair separation distances. Eq. A.6 implies that analyzing the data at peak positions beyond the first neighbor in real space will eventually allow us to probe the long-range dimensionality, 3, rather than the short-range fractal dimension, ~2.5, consistent with our original hypothesis.

References

(1) Burek, M. J.; Greer, J. R. *Nano Letters* **2010**, *10*, 69–76.

(2) Xiao, Q.; Huang, L.; Shi, Y. *Journal of Applied Physics* **2012**, *113*, 083514.

(3) Lutsko, J. F. *J. Appl. Phys. 65*, 2991–2997.

(4) Liu, Y. J.; Meirer, F.; Williams, P. A.; Wang, J. Y.; Andrews, J. C.; Pianetta, P. *Journal of Synchrotron Radiation* **2012**, *19*, 2 896MO Times Cited:21 Cited References Count:35, 281–287.

(5) Honeycutt, J. D.; Andersen, H. C. *Journal of Physical Chemistry* **1987**, *91*, K0654 Times Cited:1168 Cited References Count:42, 4950–4963.

(6) Cheng, Y.; Ding, J.; Ma, E. *Materials Research Letters* **2013**, *1*, 3–12.

(7) Ma, D.; Stoica, A. D.; Wang, X. L. *Nature Materials* **2009**, *8*, 386FC Times Cited:70 Cited References Count:38, 30–34.

(8) Ni, H.; Li, X. D.; Gao, H. S. *Appl. Phys. Lett. 88*.

(9) Tong, L. M.; Lou, J. Y.; Ye, Z. Z.; Svacha, G. T.; Mazur, E. *Nanotechnology*, *16*, 1445–1448.

(10) Jang, D. C.; Greer, J. R. *Nature Materials* **2010**, *9*, 215–219.

(11) Argon, A. S.; Kuo, H. Y. *Materials Science and Engineering* **1979**, *39*, 101–109.

(12) Hoare, J. P. *Journal of the Electrochemical Society* **1986**, *133*, 2491–2494.

(13) Gu, X.; Loynachan, C. N.; Wu, Z. X.; Zhang, Y. W.; Srolovitz, D. J.; Greer, J. R. *Nano Letters* **2012**, *12*, 6385–6392.

(14) Landau, P.; Guo, Q.; Hattar, K.; Greer, J. R. *Advanced Functional Materials* **2013**, *23*, 1281–1288.

(15) Weinberger, C. R.; Jennings, A. T.; Kang, K.; Greer, J. R. *Journal of the Mechanics and Physics of Solids* **2012**, *60*, 858UV Times Cited:21 Cited References Count:70, 84–103.

(16) Fan, Y.; Osetsky, Y. N.; Yip, S.; Yildiz, B. *Physical Review Letters* **2012**, *109*, 014CD Times Cited:7 Cited References Count:27.

(17) Fan, Y.; Osetskiy, Y. N.; Yip, S.; Yildiz, B. *Proceedings of the National Academy of Sciences of the United States of America* **2013**, *110*, 242LJ Times Cited:2 Cited References Count:50, 17756–17761.

(18) Rodney, D.; Tanguy, A.; Vandembroucq, D. *Modelling and Simulation in Materials Science and Engineering* **2011**, *19*, 844RJ Times Cited:62 Cited References Count:287.

INDEX